Pyramid wavefront sensing in the context of extremely large telescopes

Byron Engler, B.E.(Hons. I)

A thesis presented for the degree of
Doctor of Philosophy
in
Electrical and Computer Engineering
at the
University of Canterbury,
Christchurch, New Zealand.

31 July 2021

ABSTRACT

Imaging astronomical objects, such as stars, planets and galaxies, with ground-based telescopes, is challenging due to the blurring effects of Earth's time-varying atmosphere. Beyond a certain diameter, the resolution of a telescope is limited by atmospheric turbulence.

There are three ways in which the limitations of imaging through Earth's atmosphere can be addressed: put the telescope in space, real-time adaptive optics (AO), and computer post-processing. This thesis deals with real-time AO only.

An AO system consists of three major components: The deformable mirror (DM), the wavefront sensor (WFS) and the wavefront controller (WFC). A DM is a mirror where the shape of the mirror surface can be electronically controlled. The DM is placed in the telescope light path. The WFS is used to estimate the wavefront of the incoming light. The WFC takes the wavefront estimate from the WFS and drives the shape of the mirror, such that the wavefront is as close to planar as possible. This thesis focuses on the WFS and wavefront estimation.

The next generation of ground-based telescopes will have mirror diameters on the order of 25 m to 40 m. These so-called extremely large telescope (ELT)s will all make extensive use of AO systems, with the deformable mirror forming a key component in the telescopes' optical design. The preferred WFS for ELTs is the pyramid WFS. The pyramid WFS provides higher sensitivity and dynamic range in closed-loop than the Shack-Hartmann WFS commonly used in current AO systems.

The pyramid WFS consists of a 4-sided glass prism placed at the focal plane of the telescope and relay optics which re-image the pupil through the pyramid onto the WFS detector. The image formed on the detector consists of four pupil images, from which the slope of the wavefront at each position in the pupil can be found. The pyramid WFS can be generalised to an N-sided prism. This thesis explores the 2-sided roofs, 3-sided, pyramid, 6-sided and cone (infinite sides) prism WFSs in end-to-end numerical simulations using Octopus. In a high photon flux scenario, the pyramid WFS achieves the best performance, with the worst sensor within 2.5%. In a low photon flux scenario, with a high readout noise, the 3-sided WFS performs 8.6% better than the pyramid WFS.

For ELTs, and more specifically the European Extremely Large Telescope (EELT),

the support structure, or spider, which supports the secondary mirror, is large enough to obstruct entire rows of WFS subapertures. The spider arms are on the order of 50 cm thick, which is larger than the expected r_0 at the observatory site. The effect of the large spider is to sub-divide the pupil into discontinuous segments, resulting in each segment having a different mean phase (piston). Segment piston modes are poorly sensed by a pyramid WFS, but the DM can easily produce them. Segment piston can also be introduced by the wavefront reconstructor if not properly optimised. In simulation, an 8 m telescope, without a spider, achieves a closed-loop long exposure Strehl of 96% in K-band at high flux. Introducing a thick spider and keeping the AO parameters the same, the Strehl drops to 0.8%. By optimising the illumination threshold for active subaperture selection, the amount of regularisation used in the wavefront estimation and the AO loop gain, the closed-loop long exposure Strehl is significantly improved, at 94.7%.

Using the EELT 6-fold spider geometry, the pupil is divided into six segments. Using the eigenmodes of the segment piston modes, the sensitivity of the pyramid WFS to segment piston modes at different modulation radii is evaluated. The unmodulated pyramid WFS is shown to be the most sensitive to segment piston modes.

This thesis presents a new modulation technique for the pyramid WFS, the flip-flop method, which combines the increased linearity and dynamic range of the modulated pyramid, with the sensitivity to segment piston modes of the unmodulated pyramid. The flip-flop method is able to run in closed-loop and control segment piston errors, even in R-band. The flip-flop method uses a single pyramid WFS, with two modulation states, modulated and unmodulated. The modulated loop runs at 1 kHz and controls the bulk of atmospheric turbulence. The unmodulated loop has a specialised reconstructor which is optimised for controlling the segment piston modes and runs at 100 Hz. For a high flux case, with an r_0 of 15 cm, an improvement of 8.3% and 12.1% is shown for K and R-band respectively over a modulated pyramid.

Deputy Vice-Chancellor's Office
Postgraduate Office

UNIVERSITY OF CANTERBURY
Te Whare Wānanga o Waitaha
CHRISTCHURCH NEW ZEALAND

Co-Authorship Form

This form is to accompany the submission of any thesis that contains research reported in co-authored work that has been published, accepted for publication, or submitted for publication. A copy of this form should be included for each co-authored work that is included in the thesis. Completed forms should be included at the front (after the thesis abstract) of each copy of the thesis submitted for examination and library deposit.

Publication 1: Clare, R.M. and Engler, B. and Weddell, S. and Shatokhina J. and Obereder A. and Le Louarn M. (2017), 'Numerical Evaluation of Pyramid Type Sensors for Extreme Adaptive Optics for the European Extremely Large Telescope', In *Adaptive Optics for Extremely Large Telescopes (AO4ELT5)*.

Parts of Chapter 4 present material from this publication.

Publication 2: Engler, B. and Weddell, S. and Clare, R.M. (2017), 'Wavefront Sensing with Prisms for Astronomical Imaging with Adaptive Optics', In *International Conference on Image and Vision Computing New Zealand (IVCNZ)*.

Parts of Chapter 4 present material from this publication.

Publication 3: Engler, B. and Weddell, S. and Le Louarn M. and Clare, R.M. (2018), 'Effects of the telescope spider on extreme adaptive optics systems with pyramid wavefront sensors', In *Adaptive Optics Systems VI*, International Society for Optics and Photonics, SPIE.

Parts of Chapter 6 present material from this publication.

Publication 4: Engler, B. and Weddell, S. and Clare, R.M. (2018), 'A Digital Prism Wavefront Sensor for Ground-Based Astronomical Image Correction', In *International Conference on Image and Vision Computing New Zealand (IVCNZ)*.

Parts of Chapter 5 present material from this publication.

Publication 5: Engler, B. and Le Louarn M. and Verinaud C. and Weddell, S. and Clare, R.M. (2019), 'Pyramid wavefront sensing in the presence of thick spiders', In *Adaptive Optics for Extremely Large Telescopes 6 (AO4ELT6)*.

Parts of Chapter 6 and Chapter 7 present material from this publication.

Publication 6: Engler, B. Weddell, S. and Clare, R.M. (2019), 'A Digital Prism-based Wavefront Sensor Testbench', In *Adaptive Optics for Extremely Large Telescopes 6 (AO4ELT6).*

Parts of Chapter 5 present material from this publication.

Publication 7: Clare, R.M. and Engler, B. Weddell, S. (2020), 'Wavefront reconstruction with the cone sensor', In *International Conference on Image and Vision Computing New Zealand (IVCNZ).*

Parts of Chapter 4 present material from this publication.

Please detail the nature and extent (%) of contribution by the candidate:

Publication 1: Results, figures, and simulations produced by candidate. Writen by RMC. 55% of the research, and 0% of the writing was contributed by the candidate.

Publication 2: Results, figures, and written content produced by candidate. All authors provided comments and review. 85% of the research, and 95% of the writing was contributed by the candidate.

Publication 3: Results, figures, and written content produced by candidate. All authors provided comments and review. 100% of the research, and 95% of the writing was contributed by the candidate.

Publication 4: Results, figures, and written content produced by candidate. All authors provided comments and review. 100% of the research, and 95% of writing was contributed by candidate.

Publication 5: Results, figures, and written content produced by candidate. All authors provided comments and review. 100% of the research, and 95% of writing was contributed by candidate.

Publication 6: Results, figures, and written content produced by candidate. All authors provided comments and review. 100% of the research, and 95% of writing was contributed by candidate.

Publication 7: All authors provided comments and review. Written by RMC. 15% of the research, and 0% of writing was contributed by candidate.

Certification by co-authors

If there is more than one co-author then a single co-author can sign on behalf of all. The undersigned certifies that:

- The above statement correctly reflects the nature and extent of the PhD candidate's contribution to this co-authored work
- In cases where the candidate was the lead author of the co-authored work, he or she wrote the text.

Name: *Dr Richard M. Clare* Signature: RMC Date: *31 July 2021*

ACKNOWLEDGEMENTS

Firstly, I would like to thank my supervisor Dr Richard Clare and co-supervisor Associate Professor Steve Weddell for their support and guidance over the past four years. Richard also made funding available to attend and present at international conferences in Tenerife, Austin and Quebec.

In 2019, I was fortunate enough to spend three months in the adaptive optics group at the European Southern Observatory (ESO), in Garching, Germany. I would like to thank Richard for making funding available for this trip, and Dr Miska Le Louarn and Dr Christophe Verinaud for their support and supervision whilst at ESO. In 2020, I was awarded an ESO Studentship, which enabled me to return to ESO for an eight month stay. To everyone in the AO group at ESO, thank you for the warm welcome and for the willingness to share your knowledge. Taïssir, Prashant and Nelly, it was great sharing an office with you all. Thanks for all the great discussions, I have learnt so much from you all. To the friends that I have met during my time at ESO, it was great getting to know you all. From trips to the ski fields, swimming in the lakes, to countless games of volleyball, it was a good way to relax after work. Even through COVID-19 lockdowns, we found ways to entertain ourselves (Songclash and Age of Empires).

A big thank you to the technical staff in the Electrical and Computer Engineering department, especially Dave Healy, Nigel Pink, Paul Agger, Randy Hampton and Edsel Villa. They have always gone out of their way to help and support my numerous side projects over the years.

To Ben and Eugene, thanks for being there through it all, and for the many lively debates over lunch.

To my family, I think I have been a student for a lot longer than any of us had imagined. Thank you for love and support through this journey. And finally to Keisy, thank you for sticking with me through all this. The many months spent apart were not easy, but we got there in the end. Love you lots.

PREFACE

This thesis is arranged into eight chapters. Chapters 1-3 are background material and Chapters 4-7 provide the original contributions to the field of this thesis.

Chapter 1 provides an introduction to the problem of astronomical imaging with gound-based telescopes and introduces adaptive optics.

Chapter 2 outlines the mathamatical framework for this thesis.

Chapter 3 provides an introduction to optical systems and an overview of the components of an adaptive optics system.

Chapter 4 describes an N-sided prism wavefront sensor and evaluates how the geometry of the prism affects closed-loop adaptive optics performance, with end-to-end simulations.

Chapter 5 describes a digital Fourier-based wavefront sensor. Continuing from Chapter 4, an experimental configuration in the optics laboratory is developed to digitally create the wavefront sensor prism geometries. The linearity of the 3-sided, pyramid, 6-sided and cone wavefront sensor is measured.

Chapter 6 introduces the problems caused by the telescope spider, in particular segment piston errors.

Chapter 7 outlines the flip-flop modulation method for the pyramid wavefront sensor, combining the increased dynamic range of the modulated pyramid with the increased sensitivity of the unmodulated pyramid, to sense and control segment piston errors.

The thesis is concluded in Chapter 8 with a summary of the work presented and an outline of future areas of research.

PUBLICATIONS

Clare, R.M. and Engler, B. and Weddell, S. and Shatokhina J. and Obereder A. and Le Louarn M. (2017), 'Numerical Evaluation of Pyramid Type Sensors for Extreme Adaptive Optics for the European Extremely Large Telescope', In *Adaptive Optics for Extremely Large Telescopes (AO4ELT5).*

Engler, B. and Weddell, S. and Clare, R.M. (2017), 'Wavefront Sensing with Prisms for Astronomical Imaging with Adaptive Optics', In *International Conference on Image and Vision Computing New Zealand (IVCNZ).*

Engler, B. and Weddell, S. and Le Louarn M. and Clare, R.M. (2018), 'Effects of the telescope spider on extreme adaptive optics systems with pyramid wavefront sensors', In *Adaptive Optics Systems VI*, International Society for Optics and Photonics, SPIE.

Engler, B. and Weddell, S. and Clare, R.M. (2018), 'A Digital Prism Wavefront Sensor for Ground-Based Astronomical Image Correction', In *International Conference on Image and Vision Computing New Zealand (IVCNZ).*

Engler, B. and Le Louarn M. and Verinaud C. and Weddell, S. and Clare, R.M. (2019), 'Pyramid wavefront sensing in the presence of thick spiders', In *Adaptive Optics for Extremely Large Telescopes 6 (AO4ELT6).*

Engler, B. Weddell, S. and Clare, R.M. (2019), 'A Digital Prism-based Wavefront Sensor Testbench', In *Adaptive Optics for Extremely Large Telescopes 6 (AO4ELT6).*

Clare, R.M., Engler and B. Weddell, S. (2020), 'Wavefront reconstruction with the cone sensor', In *International Conference on Image and Vision Computing New Zealand (IVCNZ).*

Kasper, M. and Urra, N.C. and Pathak, P. and Bonse, M.J. and Nousiainen, J. and Engler, B. and Heritier, C.T. and Kammerer, J. and Leveratto, S. and Rajani, C. and Bristow, P. and Louarn, M.L. and Madec, P. and Strobele, S. and Vérinaud, C. and Glauser, A. and Quanz, S.P. and Helin, T. and Keller, C. and Snik, F. and Boccaletti, A. and Chauvin, G. and Mouillet, D. and Kulcsár, C. and Raynaud, H. (2021), 'PCS – A Roadmap for Exoearth Imaging with the ELT', In *The Messenger 182, 2021.*

Clare, R.M. and Engler, B. and Le Louarn M. and Verinaud C. and Weddell, S. (2021), 'A flip-flop modulation method used with a pyramid wavefront sensor to correct piston segmentation on ELTs', *in-preperation.*

CONTENTS

GLOSSARY

0.1 ACRONYMS

AO adaptive optics

DFT discrete Fourier transform

DM deformable mirror

EELT European Extremely Large Telescope

ELT extremely large telescope

FFT fast Fourier transform

FOV field of view

FWHM full width at half maximum

KL Karhunen-Loéve

MAP *maximum a posteriori*

PSD power spectral density

PSF point spread function

SCAO single conjugate adaptive optics

SLM spatial light modulator

SNR signal-to-noise ratio

WFC wavefront controller

WFS wavefront sensor

Chapter 1

INTRODUCTION

1.1 THE GROUND-BASED ASTRONOMICAL IMAGING PROBLEM

Imaging of astronomical objects, such as galaxies, stars and planets, with ground-based telescopes is typically resolution-limited by the blurring effects of Earth's atmosphere. A star can be thought of as a point source, radiating spherical light wavefronts. Due to the large distance between the telescope and the star (>4 lightyears), the spherical wavefront is effectively planar when it reaches Earth's atmosphere. As the planar wavefront passes through Earth's time-varying atmosphere, the wavefront becomes distorted, resulting in randomly distorted images of the astronomical object, which is shown in Figure 1.1.

The spatial resolution of a telescope is inversely proportional to the diameter of the telescope. A larger telescope will provide a higher resolution, however, this does not account for the blurring effects of Earth's atmosphere. Beyond a certain diameter, the resolution of a telescope imaging through Earth's atmosphere will not improve, as the limiting factor is the atmospheric turbulence. Figure 1.2 (a) shows an image of a star that has been blurred by Earth's atmosphere.

The blurring effects of Earth's atmosphere can be reduced by computer post-processing algorithms, such as deconvolution, or in real-time, with an adaptive optics system. Figure 1.2 (b) shows a perfectly corrected image of a star.

1.2 POSSIBLE SOLUTIONS FOR ASTRONOMICAL OBSERVATIONS

1.2.1 A space telescope

One method to overcome the blurring effects of Earth's atmosphere is by placing the telescope outside of Earth's atmosphere. The most famous space telescope is the Hubble Space Telescope, which is in low Earth orbit. Outside of Earth's atmosphere, the resolution of the telescope is only limited by the quality of the optics, the diameter of the mirror and the wavelength of light. Space telescopes are extremely expensive,

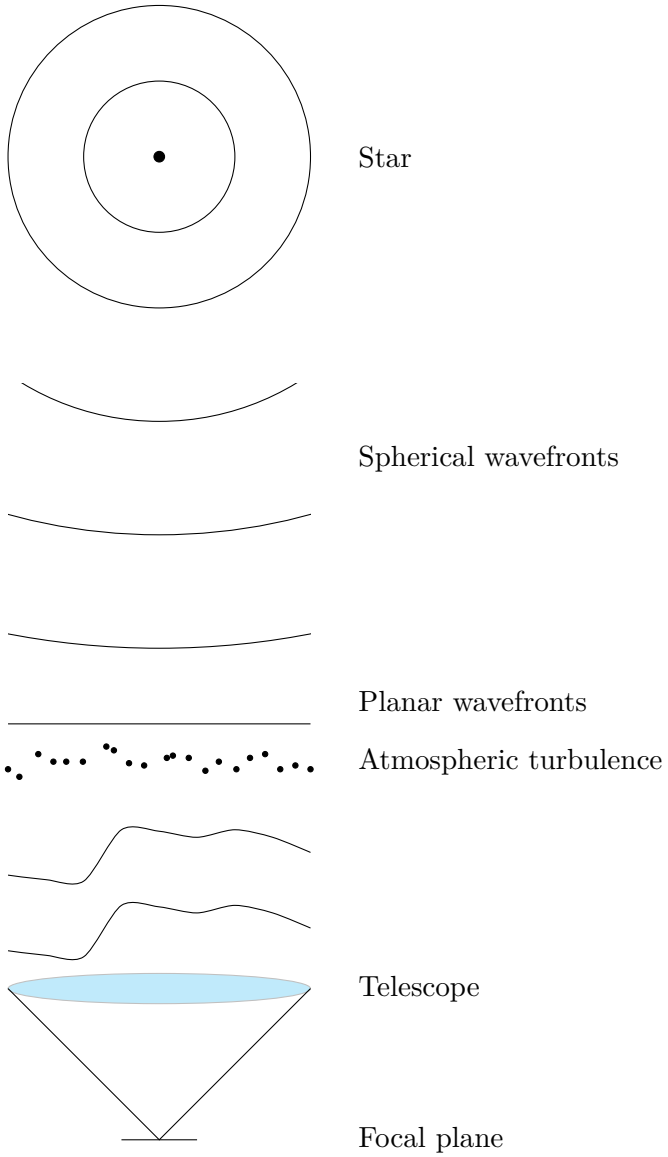

Figure 1.1 Star light propagates through space and the atmosphere to a ground-based telescope.

when compared to any ground-based telescope of equivalent size, and are inaccessible for maintenance or repair.

1.2.2 Lucky imaging

Lucky imaging is an imaging method that uses the statistics of Earth's atmosphere to improve image quality [Law, N. M. et al. 2006]. The time-varying nature of the blurring effects of the atmosphere means that at some point in time there is a chance that the blurring effect is small (lucky) and other times it is large (unlucky). If several thousand short-exposure images are taken, they can be sorted by an image quality metric and the best fraction of images are aligned and averaged together to form the final image, significantly reducing the blurring effects of Earth's atmosphere.

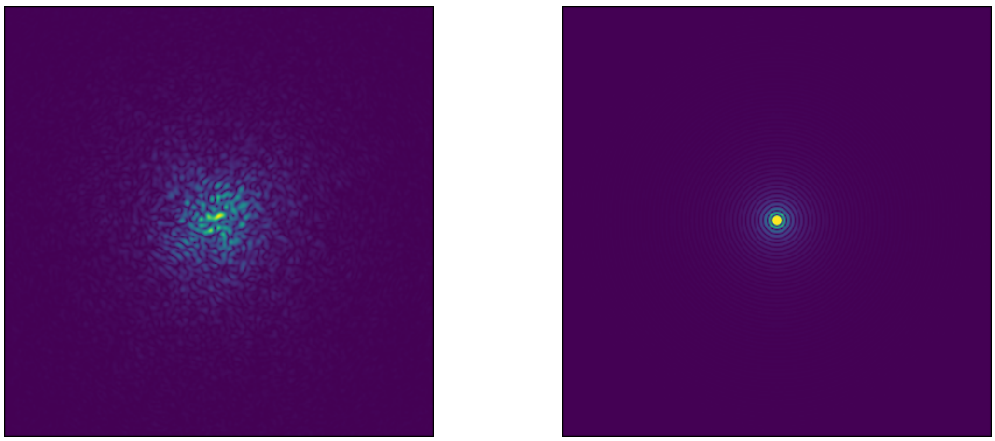

(a) (b)

Figure 1.2 A simulated comparison of a star that has been distorted by Earth's atmosphere (a) and a diffraction-limited star (b), ie no atmosphere.

1.2.3 Post-processing

A telescope can be fitted with a WFS along with the primary imaging sensor. The WFS can be used to estimate the wavefront of light that has been distorted by the atmosphere. If the primary imaging camera and the WFS capture their data simultaneously, the image from the primary camera can be post-processed using the wavefront estimate to improve the resolution of the image. A common technique for this is deconvolution from wavefront sensing [Primot et al. 1990].

1.2.4 Adaptive optics

Lucky imaging and post-processing techniques are limited to imaging only and only make use of a portion of the measured data. AO is a closed-loop optomechanical system that measures and corrects atmospheric turbulence in real-time and is useful for any observation method (imaging or spectroscopy). A simplified diagram of an AO system is shown in Figure 1.3. A WFS is used to determine the shape of the incoming wavefront. The measurements from the WFS are used by the wavefront controller (WFC) to calculate the shape to apply to a deformable mirror (DM). The DM is a mirror with an array of actuators attached to its underside. The actuators have precise position control and take commands from the WFC, which allow for fine control over the mirror's shape [Hickson 2014].

An example of what is possible with a current AO enabled ground-based telescope is shown in Figure 1.4. Using the MUSE instrument at the Very Large Telescope, an image is taken of the globular cluster NGC 6388. The left image shows a wide field of view (FOV) ($60''$ x $60''$) with AO off, the middle image is a zoomed-in portion of the left image ($7''$ x $7''$), and the right image is the same field as the zoomed-in portion,

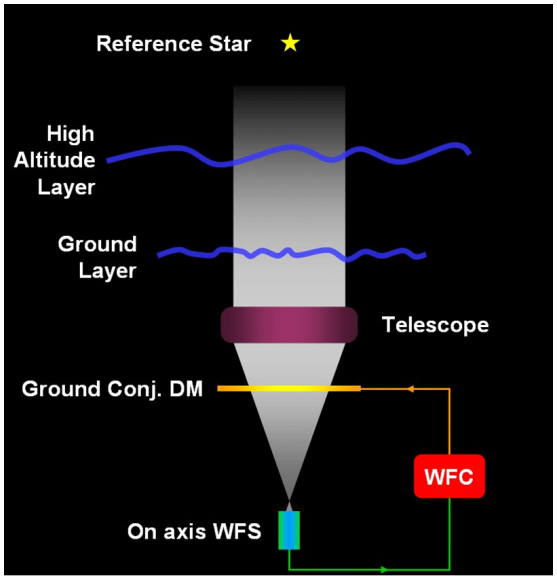

Figure 1.3 A simplified schematic of an AO system. Measurements from a WFS are used by the wavefront controller to calculate commands to send to the deformable mirror [Hubin et al. 2006].

but with AO on. With AO on, the stars are much sharper and many more stars are resolved.

1.3 EXTREMELY LARGE TELESCOPES

The next generation of ground-based telescopes, so-called ELTs, will have diameters on the order of 25 m to 40 m and expect to have first light between 2027 [ESO 2021] and 2030 [GMT 2021]. To fully realise the resolution enabled by the size of these telescopes, they will all employ adaptive optics systems. This thesis focuses on the challenges faced by the adaptive optics systems that will be used by the ELTs, in particular, the European Extremely Large Telescope. The three largest of the Extremely Large Telescopes are shown in Figure 1.5.

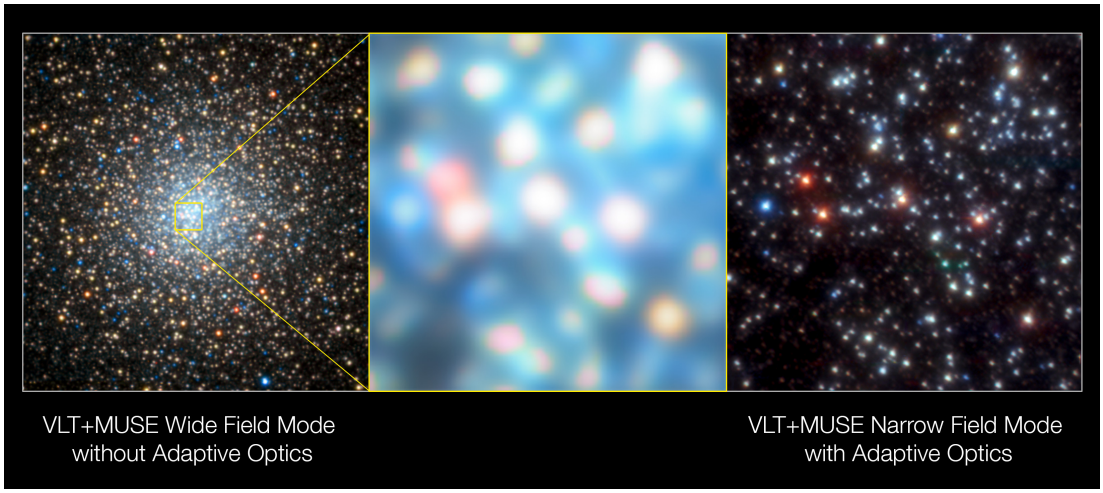

Figure 1.4 Images of the globular cluster NGC 6388 taken with the MUSE instrument at the Very Large Telescope. The left is an image from MUSE in Wide-Field Mode (60″ x 60″), with AO off, the centre image is a zoomed in view of the wide-field image (7″ x 7″). The right image is from MUSE in Narrow-Field Mode with AO turned on (7″ x 7″), showing the same region as the centre image. Image taken from the follwing ESO Press Release: https://www.eso.org/public/news/eso1824/

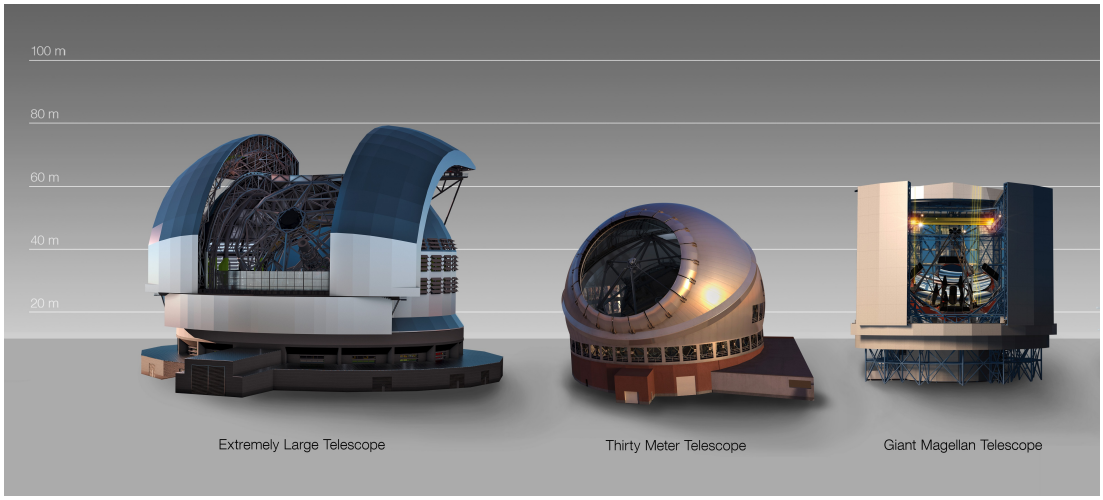

Figure 1.5 3D renderings comparing the size of the European Extremely Large Telescope, Thirty Meter Telescope and the Giant Magellan Telescope. Image taken from the following ESO Press Release: https://www.eso.org/public/news/eso1716/

1.3.1 The EELT

The European Extremely Large Telescope (EELT) is the European Southern Observatory's design of an ELT class telescope. The optical configuration of the telescope is shown in Fig. 1.6, where the primary mirror, M1, is a 39 m segmented mirror [Cayrel 2012]. The Exoplanet Imaging Camera and Spectrograph (EPICS) is a planned instrument for the EELT, which will be used for making direct spectroscopic and photometric observations of extrasolar planets. The instrument will implement a so-called Extreme AO (XAO) system using a pyramid WFS [Kasper et al. 2010]. The EPICS instrument

aims for near-diffraction-limited imaging.

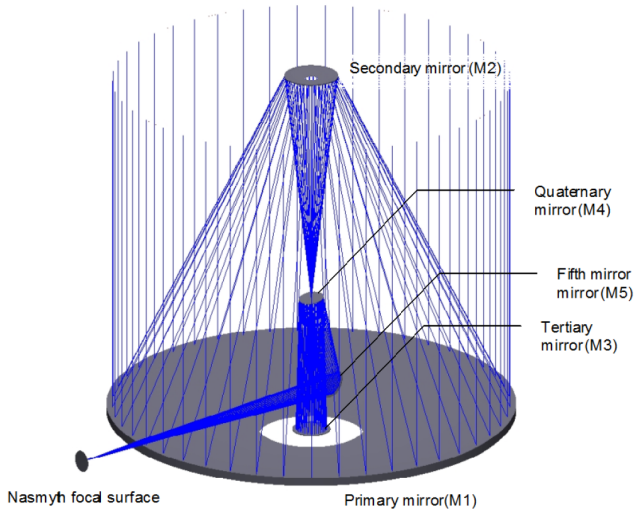

Figure 1.6 The optical configuration of the EELT [Vernet et al. 2012].

1.3.2 The TMT

The Thirty Meter Telescope (TMT) is being designed and built by the TMT International Observatory LLC. The TMT will have a 30 m diameter segmented primary mirror [Boyer and Ellerbroek 2016]. Initial plans were to construct the telescope in Hawaii with a back-up site on a Canary Island, La Palma. The first light AO facility for the TMT is the Narrow Field Infra-Red AO System (NFIRAOS). NFIRAOS is a multi-conjugate AO system which makes use of both natural and laser guide stars and will use a pyramid WFS for high order corrections [Boyer 2018].

1.3.3 The GMT

The Giant Magellan Telescope's primary mirror is made up of seven 8 m mirrors, with an effective diameter of 25 m. The telescope is being constructed at the Las Campanas Observatory in Chile [Bouchez et al. 2018a]. The natural guide star AO system will make use of a pyramid WFS [Bouchez et al. 2018b].

Chapter 2

MATHEMATICAL BACKGROUND

In this chapter, the mathematical notation and functions used in this thesis are outlined. First, the coordinate systems used in this thesis are described, followed by common mathematical concepts, and the definition of special functions. The optical systems described in this thesis can all be expressed in terms of matrices. The matrix notation is defined here. In optics, the complex electro-magnetic fields at the pupil and focal planes are related as a Fourier pair. The Fourier transform is defined and the common computational implementation, the fast Fourier transform (FFT), is introduced.

2.1 COORDINATE SYSTEMS

There are three commonly used coordinate systems: Cartesian, polar and spherical. This thesis makes use of Cartesian and polar coordinates. In this thesis, Cartesian coordinates are used to model optical systems, and a point in the pupil or focal plane is expressed as a vector $\mathbf{x_1} = (x_1, y_1)$, and $\mathbf{u_1} = (u_1, v_1)$ respectively.

The polar coordinate system is used to define Zernike polynomials in Section 3.2.1. A point in polar coordinates, (r, θ), consists of a radius r, and an angle θ. Converting from polar to Cartesian coordinates is defined as

$$x = r\cos(\theta) \tag{2.1}$$

$$y = r\sin(\theta). \tag{2.2}$$

Converting from Cartesian to polar coordinates is defined as follows

$$r = \sqrt{x^2 + y^2} \tag{2.3}$$

$$\theta = \tan^{-1}\left(\frac{y}{x}\right). \tag{2.4}$$

2.2 COMPLEX NUMBERS

In this thesis, the imaginary number defined as $\sqrt{-1}$, is denoted as j. Complex numbers are used when describing electromagnetic waves, containing both magnitude and phase

values. A complex number, z, is given by

$$z = a + jb, \tag{2.5}$$

where a is the real component and b is the imaginary component. The magnitude of z is expressed as

$$|z| = \sqrt{a^2 + b^2}. \tag{2.6}$$

The phase of z is expressed as

$$\phi = \tan^{-1}\Big(\frac{b}{a}\Big). \tag{2.7}$$

The complex conjugate of z is denoted as z^* and is expressed as

$$z^* = a - jb. \tag{2.8}$$

2.3 SPECIAL FUNCTIONS

2.3.1 Pupil function

The pupil function, $P(x, y)$, is used to define a circular telescope pupil with a radius of r

$$P(x,y) = \begin{cases} 0, & \sqrt{x^2+y^2} > r \\ 1, & \sqrt{x^2+y^2} \leq r. \end{cases} \tag{2.9}$$

2.3.2 Rectangular fucntion

The rectangular function, rect(x), is used to model square optical elements such as square telescope pupils, or lenslets [Goodman 2005]. For one dimension, the rectangular function is defined as

$$\text{rect}(x) = \begin{cases} 1, & |x| < \frac{1}{2} \\ 0, & otherwise. \end{cases} \tag{2.10}$$

2.3.3 Sinc function

Taking the Fourier transform of the rectangular function results in the sinc function. The sinc function is defined as

$$\operatorname{sinc}(x) = \begin{cases} \frac{\sin(\pi x)}{\pi x}, & x \neq 0 \\ 1, & x = 0. \end{cases} \tag{2.11}$$

2.4 THE FOURIER TRANSFORM

The Fourier transform was introduced by Joseph Fourier in 1822 [Fourier 1822]. The Fourier transform decomposes a signal into an infinte sum of two basis functions, sin and cos. The Fourier transform converts a signal from one domain (e.g. time) to another (e.g. frequency) and in two dimensions is defined as

$$F(u,v) = \int_{-\infty}^{\infty}\int_{-\infty}^{\infty} f(x,y)e^{-j2\pi(ux+vy)}\,dx\,dy. \tag{2.12}$$

The reverse operation of a Fourier transform is the inverse Fourier transform. If the Fourier transform converts from the time domain to the frequency domain, then the inverse Fourier transform converts from the frequency domain to the time domain, and is expressed in two dimensions as

$$f(x,y) = \int_{-\infty}^{\infty}\int_{-\infty}^{\infty} F(u,v)e^{j2\pi(ux+vy)}\,du\,dv. \tag{2.13}$$

The Fourier transform is denoted by the $\mathcal{F}$ operator.

In terms of optics, the Fourier transform is used to propogate a signal from the pupil plane to the focal plane. The inverse Fourier transfrom is used to propogate a signal from the focal plane to the pupil plane.

Unfortunately, in the real world, signals are often sampled at discrete intervals. For example, a camera used to measure the intensity at the focal plane has a finite number of pixels. Discretising the Fourier transform leads to the discrete Fourier transform (DFT), which is defined as

$$F(u,v) = \frac{1}{XY}\sum_{x=0}^{X-1}\sum_{y=0}^{Y-1} f(x,y)e^{-j2\pi(\frac{ux}{X}+\frac{vy}{Y})}, \tag{2.14}$$

where X and Y are the number of samples in the x and y axes respectively. The inverse DFT is defined as

$$f(x,y) = \sum_{u=0}^{X-1}\sum_{v=0}^{Y-1} F(u,v)e^{j2\pi(\frac{ux}{U}+\frac{vy}{V})}. \tag{2.15}$$

In Equation (2.14) and Equation (2.15), it is assumed that the samples are taken with constant interval size.

2.4.1 The Fast Fourier Transform

Computationally, the most common and fastest method for calculating the DFT is with the FFT algorithm, which was developed by Cooley and Tukey [Cooley and Tukey 1965]. The DFT is computed in $\mathcal{O}(N^2)$ time, while the FFT is computed in $\mathcal{O}(N \log N)$, where N is the number of samples. The FFT is used to compute all the DFTs in this thesis.

2.4.2 Convolution theorem

In the context of this thesis, the convolution theorm is one of the most important Fourier transform relations. The convolution operator, $\odot$, defines the convolution integral of two functions $g(x, y)$ and $h(x, y)$,

$$g(x, y) \odot h(x, y) = \int_{-\infty}^{\infty} \int_{-\infty}^{\infty} g(\xi, \eta) h(x - \xi, y - \eta) d\xi d\eta, \tag{2.16}$$

where ξ and η are dummy variables used in the integral.

The convolution can also be defined in terms of the Fourier transform as

$$\mathcal{F}\{g(x, y) \odot h(x, y)\} = G(u, v)H(u, v). \tag{2.17}$$

The convolution theorm states that the convolution of two signals is equivalent to the multiplication of the respective Fourier transforms of the signals.

2.5 MATRICES AND VECTORS

An M by N matrix, A, is defined as

$$A = \begin{bmatrix} a_{1,1} & a_{1,2} & \cdots & a_{1,N} \\ a_{2,1} & a_{2,2} & \cdots & \\ \vdots & & \ddots & \vdots \\ a_{M,1} & & \cdots & a_{M,N} \end{bmatrix}, \tag{2.18}$$

where $a_{m,n}$ is the element in the m^{th} row and n^{th} column. A is a square matrix if $M = N$.

The transpose of matrix A, denoted as A^T, is found by swapping the row and

column indices,

$$A^T = \begin{bmatrix} a_{1,1} & a_{2,1} & \cdots & a_{M,1} \\ a_{1,2} & a_{2,2} & \cdots & \\ \vdots & & \ddots & \vdots \\ a_{1,N} & & \cdots & a_{M,N} \end{bmatrix}. \tag{2.19}$$

A is $M \times N$, while A^T is $N \times M$.

The identity matrix, I, is a square matrix with ones on the diagonal and zeros everywhere else. The identity matrix is analogous to the number 1 in numerical algebra.

For a square matrix A, the inverse is denoted as A^{-1} and is defined as

$$AA^{-1} = I = A^{-1}A. \tag{2.20}$$

If A^{-1} exists, then A is invertible.

2.5.1 Singular value decomposition

Singular value decomposition is a generalisation of the eigendecomposition for square matrices to any $M \times N$ matrix, where a matrix is factorised into eigenvectors and eigenvalues [Strang 2006]. The singular value decompsition of A is defined as

$$A = USV^T, \tag{2.21}$$

where the columns of V are the eigenvectors of A^TA, the columns of U are the eigenvectors of AA^T, and S is a diagonal matrix made up of the square root of the non-zero eigenvalues corresponding to U and V.

2.5.2 Pseudoinverse

A matrix A is not always invertible. In cases where the inverse does not exist, the Moore-Penrose inverse (or pseudoinverse) can be used, and is denoted as $A^\dagger$ [Strang 2006]. The pseudoinverse can be found by singular value decomposition

$$A^\dagger = VS^{-1}U^T, \tag{2.22}$$

where the diagonal elements of S^{-1} are $[1/s_1, \cdots, 1/s_k]$, where $s_1, ..., s_k$ are non-zero elements of S.

2.5.3 Matrix vectorisation

In this thesis, it is common to vectorise matrices i.e. reducing a 2D matrix to a 1D vector. For a matrix such as A, vectorising it row-by-row results in

$$\mathbf{A} = [a_{1,1}, a_{1,2}, \cdots, a_{1,N}, a_{2,1}, a_{2,2}, \cdots, a_{2,N}, \cdots, a_{M,1}, a_{M,2}, \cdots, a_{M,N}]. \tag{2.23}$$

Chapter 3

BACKGROUND

To understand AO, it is essential to have a general understanding of optics. This chapter provides a review of optics, starting with geometric optics, which considers light propagation in terms of photons, and extends to Fourier optics which describes the propagation of light in terms of waves and the diffraction effects of light. This chapter also introduces atmospheric turbulence and AO systems.

3.1 OPTICS THEORY

3.1.1 Geometric optics

In geometric optics, a light ray is a straight line pointing away from a point source. A wavefront is a surface of constant optical path length from the point source. The wavefront is perpendicular to the light rays.

The refractive index of a medium is defined as the ratio of the speed of light in a vacuum, c, to the speed of light in the medium, v, [Goodman 2005]

$$n = \frac{c}{v}. \tag{3.1}$$

The refractive index defines how light behaves at the interface of two media. At the interface of two media, two optical phenomena are observed: refraction and reflection. In Figure 3.1, the incident ray A, traveling through medium one, reaches an interface with medium two. A fraction of the incident light is reflected as ray B. The angle of incidence of ray A, θ_1, is measured to the norm of the interface. The angle of reflection is equal to the angle of incidence. Ray C is the unreflected light passed from medium one to medium two. The angle of refraction, θ_2, of the transmitted ray is defined by Snell's law [Goodman 2005]

$$\frac{n_2}{n_1} = \frac{sin(\theta_1)}{sin(\theta_2)} = \frac{v_1}{v_2}, \tag{3.2}$$

where v_1 and v_2 are the speed of light in the respective media. In a geometric approximation of light propagation, a photon at some position in a wavefront propagates

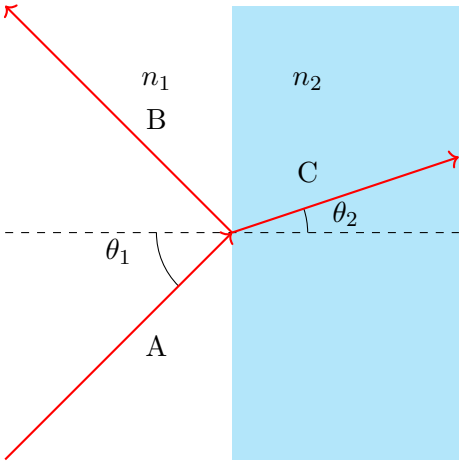

Figure 3.1 The reflection (B) and refraction (C) of an incident light ray (A) at a step change in refractive index between two media.

perpendicularly to the wavefront at that position. The geometric approximation does not include diffractive effects.

3.1.1.1 Optical elements

Optical elements can be divided into three main groups: refractive, reflective and diffractive. Only refractive and reflective elements are considered in this thesis. A refractive lens uses the difference in refractive index of two media (typically air and glass) to converge or diverge a wavefront. Using a curved lens, the focal length, f, of the lens is related to the radii of curvature, r_1 and r_2, of both faces of the lens and the refractive index of the lens material, n:

$$\frac{1}{f} = (n-1)\Big(\frac{1}{r_1} - \frac{1}{r_2}\Big). \tag{3.3}$$

Figure 3.2 shows a diagram of a convex lens, showing the radii of curvature, r_1 and r_2, and the focal length f.

Reflective optics use a mirror to converge or diverge a wavefront. For a concave mirror, the focal length, f, is

$$f = \frac{r}{2}, \tag{3.4}$$

where r is the radius of curvature of the mirror.

For optical systems operating with chromatic light (light consisting of multiple wavelengths), mirrors perform better than lenses, as the refractive index of a material is wavelength dependent. In comparison, the reflection of a mirror is independent of wavelength.

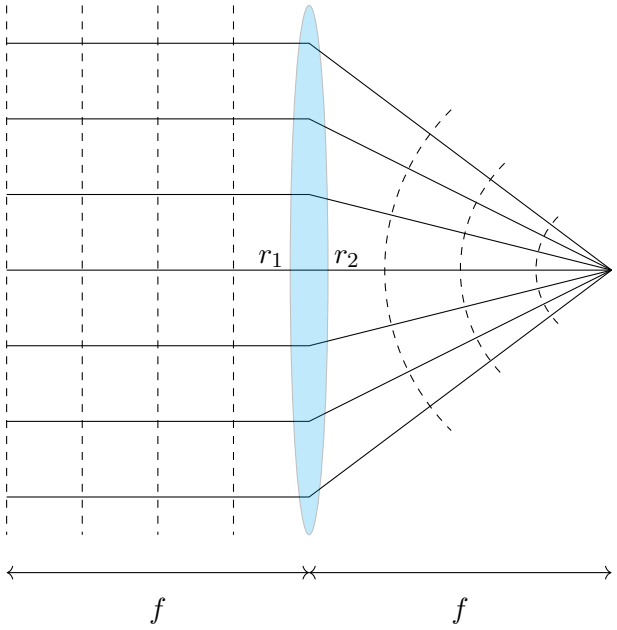

Figure 3.2 A converging lens with focal length f. The radii of curvature of the surfaces of the lens are denoted by r_1 and r_2.

3.1.2 Fourier optics

Geometric optics can describe simple systems without taking the wave-like nature of light into account. To consider systems where effects of diffraction and interference are required, Fourier optics is used. Fourier optics considers light as a wave rather than a particle. Within Fourier optics, two models of diffraction exist. For the near-field, where wavefronts are spherical, Fresnel diffraction is used. By taking a binomial approximation of the Huygens-Fresnel principle [Goodman 2005], Fresnel diffraction is described as

$$U(x,y) = \frac{e^{jkz}}{j\lambda z}\int_{-\infty}^{\infty}\int_{-\infty}^{\infty} U(u,v)e^{\frac{jk}{2z}((x-u)^2+(y-v)^2)}dudv, \tag{3.5}$$

where $U(x,y)$ is the diffracted electromagnetic field, $U(u,v)$ is the input electromagnetic field, z is is the distance between $U(x,y)$ and $U(u,v)$, k is the wave number ($\frac{2\pi}{\lambda}$), and λ is the wavelength of light [Goodman 2005].

Once the wavefront has propagated far enough such that it appears planar (far-field), Fraunhofer diffraction is used. The distance, z, after which the Fraunhofer approximation is used, is

$$z >> \frac{k(u^2+v^2)_{max}}{2}. \tag{3.6}$$

The Fraunhofer diffraction model is defined as [Goodman 2005]

$$U(x,y) = \frac{e^{jkz}}{j\lambda z}e^{\frac{jk}{2z}(x^2+y^2)}\int_{-\infty}^{\infty}\int_{-\infty}^{\infty} U(u,v)e^{-\frac{jk}{2z}(xu+yv)}dudv. \tag{3.7}$$

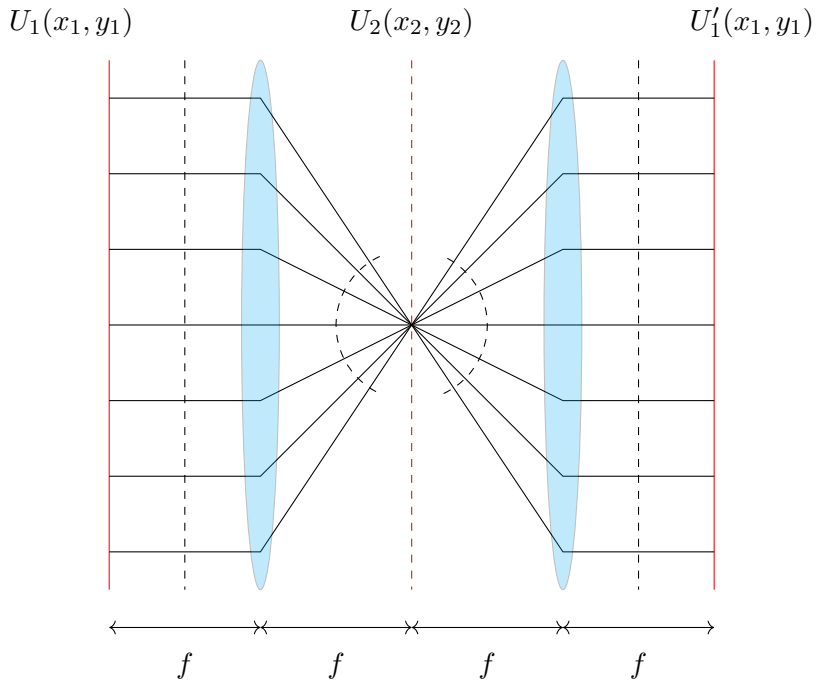

Figure 3.3 Through a 4f optical system, the input electromagnetic field is duplicated at the output.

An important realisation is that apart from the multiplicative factor, $\frac{e^{jkz}}{j\lambda z}e^{\frac{jk}{2z}(x^2+y^2)}$, the Fraunhofer model states the electromagnetic field, $U(x, y)$, propagated a distance z, is simply the Fourier transform of the input electromagnetic field, $U(u, v)$ [Goodman 2005]. An image sensor is not able to measure the complex field, $U(x, y)$, directly, but instead the intensity is measured, $|U(x, y)|^2$.

3.1.2.1 Optical conjugation

A special case of wavefront propagation occurs when the propagation distance, z, is equal to the focal length, f, of a lens being modeled. In the special case of $z = f$ before the lens and $z = f$ after the lens, Equation (3.7) can be rearranged to be [Breckinridge and Voelz 2011]:

$$U_2(x_2, y_2) = \frac{e^{jkf}}{j\lambda f}\int_{-\infty}^{\infty}\int_{-\infty}^{\infty} U_1(x_1, y_1)P(x_1 + x_2, y_1 + y_2)e^{-\frac{jk}{2z}(x_1x_2+y_1y_2)}dx_1dy_1, \quad (3.8)$$

where $P(x, y)$ is the pupil function, (x_1, y_1) are coordinates in the U_1 plane, and (x_2, y_2) are coordinates in the U_2 plane. The pupil function arguments account for vignetting, where there is a loss of light off-axis due to the finite pupil size. $U_2(x_2, y_2)$ is then a scaled Fourier transform of $U_1(x_1, y_1)$.

The special case of Fraunhofer propagation, where $z = f$ before and after the lens, is used to model optical conjugation. Figure 3.3 illustrates an optical system where $U_1(x_1, y_1)$ and $U_1'(x_1, y_1)$ are optically conjugated.

3.1.3 Point spread function

The point spread function (PSF), $G(u, v)$, is the impulse response of an optical system, i.e., the optical system's response to a point source of light. When imaging an object through an optical system, the resulting image, $I(u, v)$, can be described as the convolution of the true object image, $O(u, v)$ with the PSF, $G(u, v)$, of the optical system,

$$I(u, v) = O(u, v) \odot G(u, v). \tag{3.9}$$

Using Fraunhofer diffraction, the diffractive patterns for different pupil geometries can be calculated. In a one dimensional (1D) case, if the pupil is defined as $\text{rect}(x)$, then the resulting PSF is

$$G(u) = \text{sinc}^2(u), \tag{3.10}$$

and is plotted in Figure 3.4. Extending the 1D case to two dimensions, the pupil becomes a square, $P(x, y) = \text{rect}(x)\text{rect}(y)$, and

$$G(u, v) = \text{sinc}^2(u)\text{sinc}^2(v), \tag{3.11}$$

which is shown in Figure 3.5.

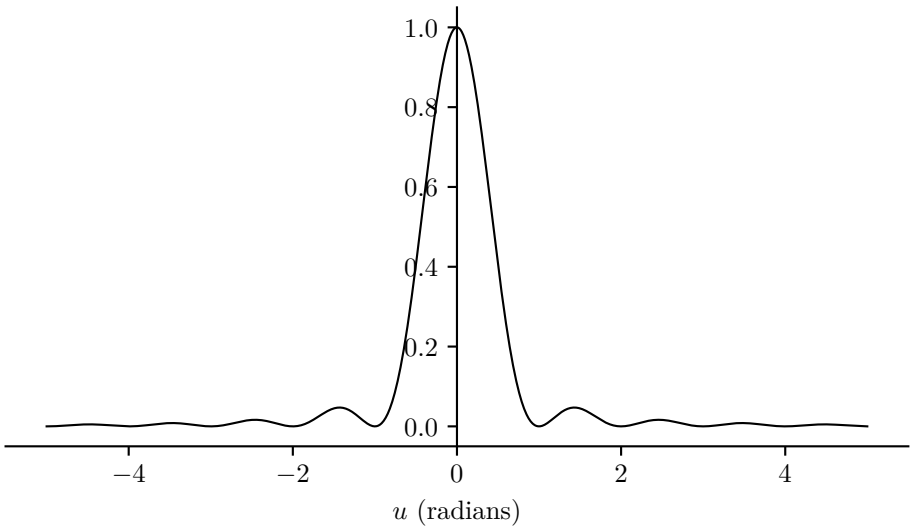

Figure 3.4 The 1D diffraction-limited PSF of a system with a rectangular pupil.

In the case of a circular pupil, $P(x, y)$, the PSF can be expressed with a Bessel function of the first kind, in polar coordinates

$$G(\omega) = \frac{2J_1(\omega)}{\omega}, \tag{3.12}$$

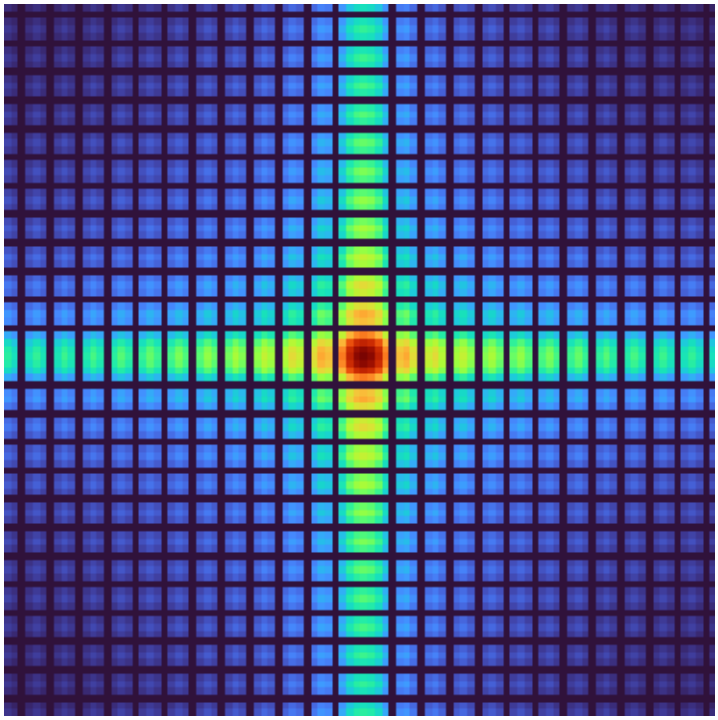

Figure 3.5 The diffraction-limited PSF of a telescope with a square pupil.

where

$$\omega = \frac{2\pi}{\lambda}\frac{r}{z}\sqrt{u^2 + v^2}, \tag{3.13}$$

where r is the radius of the pupil. The PSF for a circular pupil is plotted in Figure 3.6. The PSF of a circular pupil is know as an Airy disk.

3.1.4 Rayleigh diffraction limit

An optical system has a finite minimum detectable angular separation, e.g., the ability to resolve binary stars. The minimum resolvable separation can be described as the angular separation of two Airy disks, where the peak of one disk falls on the first null of the second disk; as shown in Figure 3.7. The Rayleigh resolution limit is

$$\alpha_{min} = 1.22\frac{\lambda}{D}, \tag{3.14}$$

where α_{min} describes the smallest angular separation detectable for a given optical system, λ is the wavelength at which the observation is made at, and D is the diameter of the telescope mirror [Born and Wolf 1999]. For the same wavelength of light, the larger the pupil (mirror) of the telescope, the finer the details that can be resolved, assuming no atmospheric turbulence.

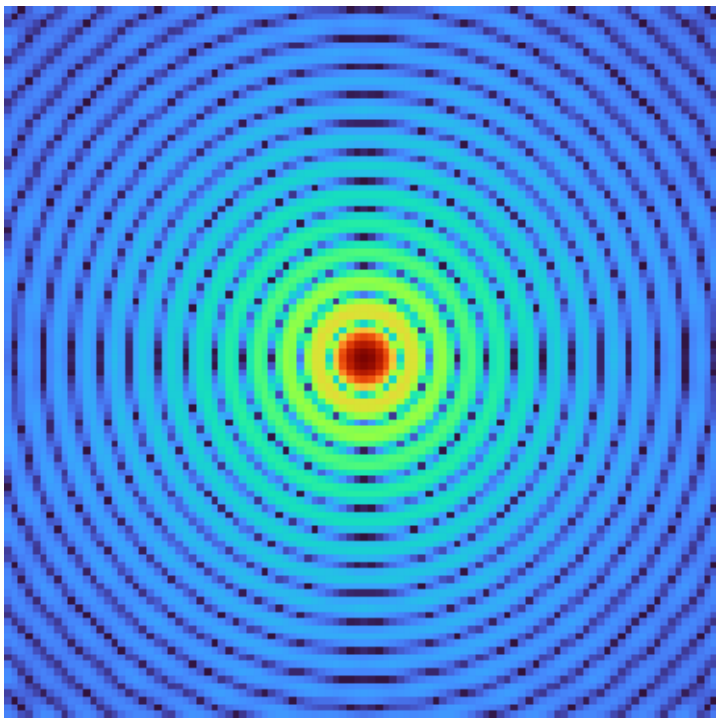

Figure 3.6 The diffraction-limited PSF of a telescope with a circular pupil. The Airy disk pattern is clearly visible.

3.2 ATMOSPHERIC TURBULENCE

The wavefront of incoming starlight becomes distorted as it propagates through Earth's atmosphere. The distortions are due to random time-varying differences in air temperature and humidity, which vary the refractive index of the air [Roddier 1999]. A statistical model for the time-varying turbulence was first proposed by Kolmogorov [Kolmogorov 1941] and has been extended to include the statistics of the change of refractive index. The Kolmogorov power spectrum, $\Phi_n^k(\mathbf{k})$, of the varying refractive index is defined as [Roddier 1999]

$$\Phi_n^k(\mathbf{k}) = 0.033(2\pi)^{\frac{2}{3}} C_n^2(h)|\mathbf{k}|^{\frac{-11}{3}} , \tag{3.15}$$

where $\mathbf{k}$ is the spatial wavenumber vector, $C_n^2(h)$ is the refractive index structure constant at height, h, above ground. Energy is input to the atmosphere by radiation from the Sun at the outer scale, L_0, typically on the order of tens of metres. The energy progresses through the atmospheric system at finer and finer scales until the inner scale, l_0 (typically millimetres), where the energy dissipates as heat. The Kolmogorov power spectrum does not account for finite inner and outer scales and loses accuracy at low spatial frequencies. The Von Karman power spectrum, $\Phi_n^v(\mathbf{k})$, includes the effects of

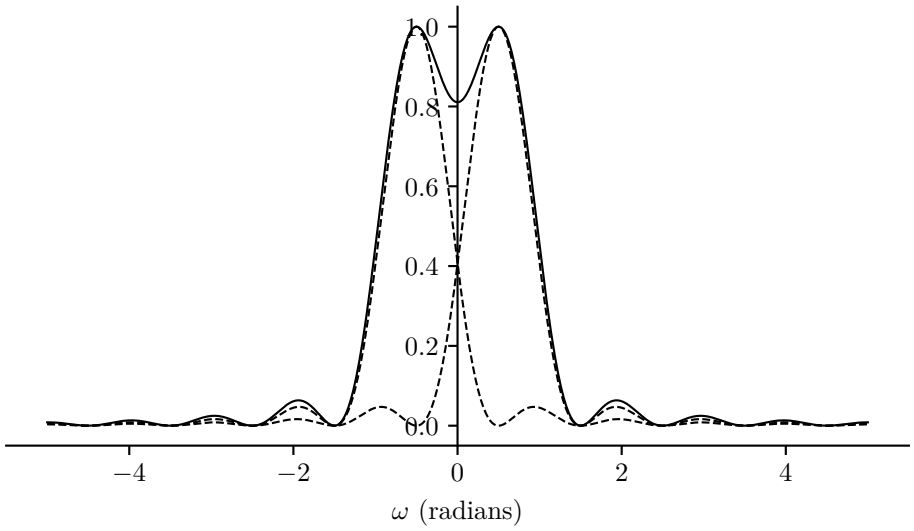

Figure 3.7 Two overlapping Airy disks, where the peak of one disk is over the first null of the second disk.

finite inner and outer scales

$$\Phi_n^v(\mathbf{k}) = 0.033(2\pi)^{\frac{2}{3}} C_n^2(h) \left[|\mathbf{k}|^2 + \left(\frac{1}{L_0} \right)^2 \right]^{\frac{-11}{6}} e^{-(|k|l_0)^2}. \tag{3.16}$$

As seen from the ground, the total turbulence is then the integral of the turbulence at every height, h, above the ground. In practice, the atmospheric turbulence tends to form in distinct layers and can be defined by the C_n^2 of each layer. The strength of the turbulence can be summarised by the Fried parameter, r_0, also known as the coherence length [Fried 1966]. The Fried parameter is defined as the diameter over which the wavefront variance is less than $1\,\text{rad}^2$. The Fried parameter, when observed at wavelength λ, is expressed as

$$r_0(\lambda) = 0.423 \left(\frac{2\pi}{\lambda} \right) \int_0^\infty C_n^2(h)\, dh. \tag{3.17}$$

Another parameter of use to characterise atmospheric turbulence is the coherence time, τ_0, which is the duration over which the atmosphere appears frozen. The coherence time is expressed as

$$\tau_0(\lambda) = (6.88)^{\frac{-3}{5}} \frac{r_0}{\bar{\nu}}, \tag{3.18}$$

where $\bar{\nu}$ is a weighted average of the layers' velocities.

When simulating atmospheric turbulence in the context of AO systems, the atmosphere is modeled as a superposition of independent layers. Each layer is translated at a fixed velocity (wind speed), $\nu(h)$, in a fixed direction, and is known as frozen flow. The concept of frozen flow was introduced by Taylor [Taylor 1938].

The full width at half maximum (FWHM) of the PSF due to atmospheric turbulence is a function of r_0. For a large telescope where $D >> r_0$, the PSF FWHM can be expressed as [Roddier 1999]:

$$\theta = 2.013 \times 10^5 \frac{\lambda}{r_0}, \tag{3.19}$$

where λ is the wavelength of observation. θ defines the smallest resolvable feature, in arcseconds, in a long exposure image and is the common measure for seeing.

3.2.1 Modal decomposition of atmospheric phase

In order for an AO system to compensate for atmospheric turbulence, it is first necessary to estimate the phase of the wavefront. The phase of the wavefront, $\phi(x, y)$, can be represented as a weighted sum of basis functions, $\psi(x, y)$, defined over the telescope pupil, and can be represented by

$$\phi(x, y) = \sum_{i=0}^{\infty} a_i \psi_i(x, y), \tag{3.20}$$

where a_i is the i^{th} coefficient of the basis function and ψ_i is the i^{th} basis function.

3.2.1.1 Zernike basis

Zernike polynomials are commonly used as the basis function in AO systems, as they match classical optical distortions such as defocus, astigmatism and coma [Lane and Tallon 1992, Noll 1976]. Zernike polynomials can be expressed analytically, using the Noll ordering [Noll 1976]:

$$Z_{even,i}(r, \theta) = \sqrt{n+1} R_n^m(r) \sqrt{2} cos(m\theta), m \neq 0 \tag{3.21}$$

$$Z_{odd,i}(r, \theta) = \sqrt{n+1} R_n^m(r) \sqrt{2} sin(m\theta), m \neq 0 \tag{3.22}$$

$$Z_i(r) = R_n^0(r), m = 0, \tag{3.23}$$

where

$$R_n^m(r) = \sum_{s=0}^{(n-m)/2} \frac{(-1)^s (n-s)!}{s![(n+m)/2 - s]![(n-m)/2 - s]!} r^{n-2s}, \tag{3.24}$$

where n is the radial order, m is the azimuthal order. The Noll index, i, is a function of m and n. The first 20 Zernike polynomials, excluding piston, are illustrated in Figure 3.8 using Noll ordering.

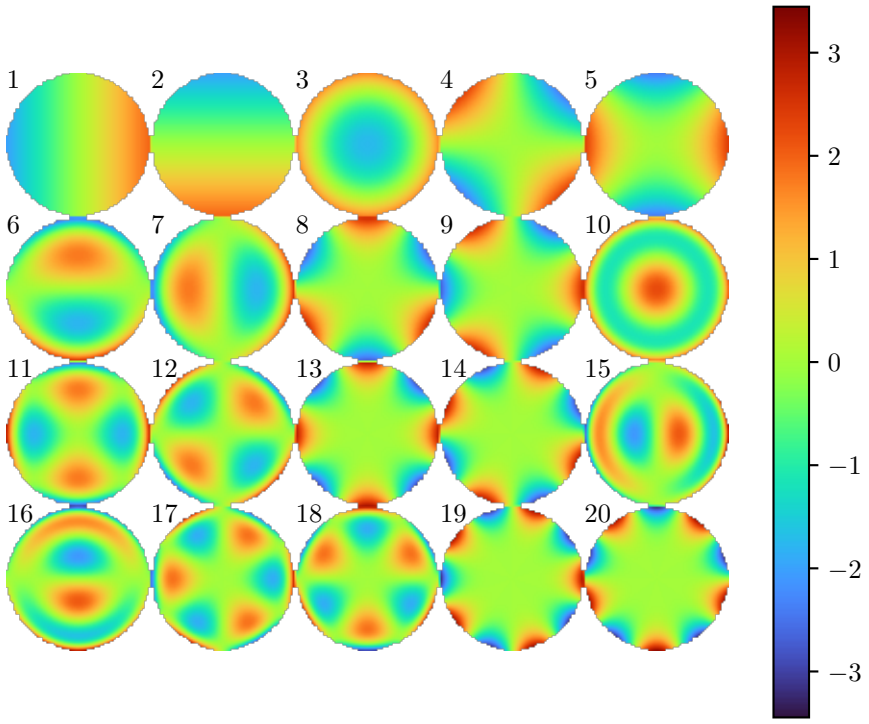

Figure 3.8 The first 20 Zernike polynomials (excluding piston), normalised to a RMS of 1, using the Noll ordering.

3.2.1.2 Karhunen-Loéve basis

The covariance matrix of the Zernike polynomials is not diagonal, meaning that some modes are correlated. For low order AO systems, Zernike polynomials might be adequate, but for high order systems, which use thousands of modes, Zernike polynomials are not optimal. The optimal modal basis is the Karhunen-Loéve (KL) basis [Gendron 1995, Mathar 2010], which takes the atmospheric statistics and the DM geometry into account. The KL basis is orthogonal, and importantly, the modes are statistically independent. A method for calculating the KL modal basis was introduced by Gendron [Gendron 1995]. The technique uses a double diagonalisation. Gendron's method starts with a geometric covariance matrix (the covariance of the DM actuators) and a statistical covariance matrix (covariance of the atmospheric turbulence). First, the geometric covariance matrix is diagonalised, then a second diagonalisation is performed after combining the diagonal geometric covariance matrix with the statistical covariance matrix [Gendron 1995, Lai et al. 2000]. This produces a modal basis which is orthonormal in the DM space and statistically independent with regards to atmospheric turbulence.

3.3 ASTRONOMICAL OBSERVATIONS

3.3.1 Imaging

In astronomy, the focal plane detector used is typically the charge-coupled device (CCD) sensor. The CCD sensor accumulates light over the exposure duration to form an image. The integration time for CCD imaging (typically on the order of minutes) is generally much larger than the coherence time, τ_0 (on the order of milliseconds). As a result, the CCD sensor detects the average position of the star over time. Due to the random variations of the atmosphere, the star becomes blurred, and the telescope's full optical resolution is not realised. If a target is bright enough, and the detector is fast enough, images can be acquired with an exposure time less than τ_0, which produces speckle images. There are imaging techniques such as lucky imaging [Baldwin et al. 2001] where these speckle images are used to create images with a higher resolution than an equivalent long exposure image taken through the same atmosphere.

3.3.1.1 Noise sources in imaging

A real-world imaging system (in this thesis, a telescope with an image detector) is degraded by noise. There are two main source of noise which are considered in this thesis: photon noise (shot noise) and detector readout noise.

For the detection process, light will be considered in its quantized form, where individual photons arrive at the detector. Independent random events, such as photon detection, can be modeled as a Poisson distribution. The probability of receiving n photons at a position (u, v) in the detector plane is expressed as

$$Pr\Big[n(u,v)\Big] = \frac{e^{-l(u,v)} l(u,v)^{n(u,v)}}{n(u,v)!}, \tag{3.25}$$

where $l(u, v)$ is the mean number of photons per pixel at position (u, v) and ! is the factorial operator [Berry and Burnell 2005]. Once the number of photons per image increases to about 20 photons, the Poisson distribution is almost indistinguishable from a Gaussian distribution. For $l > 20$ [Berry and Burnell 2005],

$$Pr\Big[n(u,v)\Big] = \frac{1}{\sqrt{2\pi l(u,v)}} e^{-\frac{(n(u,v)-l(u,v))^2}{2l(u,v)}}. \tag{3.26}$$

The CCD has noise associated with reading out the image, which is known as readout noise. Readout noise is not the only source of noise introduced by a CCD, but is all that will be considered in this thesis. Readout noise can be modeled as a Gaussian distribution. The photon noise and the readout noise are independent.

3.3.1.2 High contrast imaging and coronography

High contrast imaging (HCI) is an imaging technique used to maximise the contrast between the on-axis star and the regions immediately off-axis. HCI is beneficial in the case of imaging exoplanets. An exoplanet is several orders of magnitude dimmer than the star that it orbits. High contrast imaging techniques use a coronagraph, which occults the bright on-axis star, improving the image's contrast, thus allowing dim exoplanets to be detected.

3.3.2 Spectroscopy

Another observation technique is spectroscopy, where the starlight is directed into a spectrograph. A spectrograph is an instrument which decomposes light into a spectrum, where the intensity of the starlight can be measured over a range of wavelengths of the electromagnetic spectrum.

3.3.3 Performance metrics

3.3.3.1 Strehl ratio

A performance metric commonly used in AO is the Strehl ratio. The Strehl ratio, S, is the ratio of the peak intensity of the aberrated to the diffraction-limited PSFs,

$$S = \frac{\left|I(u,v)_{aberrated}\right|_{max}}{\left|I(u,v)_{diffraction-limited}\right|_{max}}, \tag{3.27}$$

where $I(u,v)$ are focal plane images. In the case of a point source (such as a star), the PSF and the focal plane image are equivalent. The Strehl ratio is expressed as a number from zero to one, where one represents no aberration. The Strehl ratio can be approximated from the wavefront statistics [Mahajan 1983]. Mahajan shows that over a wide range, the Strehl ratio can be approximated by

$$\text{Strehl} \approx e^{-(\frac{2\pi\epsilon}{\lambda})^2}, \tag{3.28}$$

where ϵ is the root mean square (RMS) of the wavefront optical path difference.

3.3.3.2 PSF contrast

Another performance metric used in AO is PSF contrast, which is the difference between the on-axis peak and the off-axis minimum. PSF contrast is an important metric for HCI.

3.3.4 Mean squared error

Mean squared error (MSE) is a performance metric used to evaluate the performance of wavefront estimation. In simulations, calculating the MSE is possible as the true wavefront is known. The MSE is then

$$MSE = \frac{1}{N}\sum_{i=0}^{N-1}[\mathbf{w}(i) - \hat{\mathbf{w}}(i)]^2, \tag{3.29}$$

where $\mathbf{w}$ is the true wavefront vector, $\hat{\mathbf{w}}$ is the estimated wavefront vector and N is the length of the wavefront vector. In practice with an AO system, the true wavefront is unknown, and the measured wavefront is the residual wavefront after corrections with the DM have been made. In an AO system, the desired wavefront is a flat (zero) wavefront and the MSE (or variance, σ^2) is then

$$\sigma^2 = \frac{1}{N}\sum_{i=0}^{N-1}[\hat{\mathbf{w}}_m(i)]^2, \tag{3.30}$$

where $\hat{\mathbf{w}}_m$ is the residual wavefront estimate (calculated from the WFS measurements) from the closed-loop AO system.

3.4 AN ADAPTIVE OPTICS SYSTEM

AO is a method for correcting the blurring effects that the atmosphere has on astronomical images [Davies and Kasper 2012]. Figure 1.3 shows a typical single conjugate adaptive optics (SCAO) system where one WFS is used to estimate the wavefront aberration introduced by the atmosphere. AO is an optomechanical system that utilises a DM, which changes shape under computer control. A bright guide or reference star is required to provide a usable signal-to-noise ratio (SNR) in the WFS. The guide star can be a natural star or a 'star' artificially generated with the use of a laser. The light from the guide star propagates through the atmosphere, and through the telescope where it reaches a beam splitter. The beam splitter divides the light based on wavelength, where wavelengths of scientific interest go to the science instruments and the remaining light is sent to the WFS. In the case of a laser guide star, only the wavelength of the laser light is sent to the WFS. The WFC uses measurements from the WFS to calculate the commands to send to the DM. The DM then adjusts its shape according to the commands received from the WFC and corrects the aberrated wavefront. DMs are discussed further in Section 3.6. Typically, closed-loop AO systems can operate up to a few kilohertz [Kasper et al. 2010].

SCAO is useful for observing single on-axis stars or a small FOV. Figure 3.9 shows an SCAO system where an off-axis star is present. Light from the off-axis star propagates through a part of the atmosphere which is different to that of the on-axis guide star.

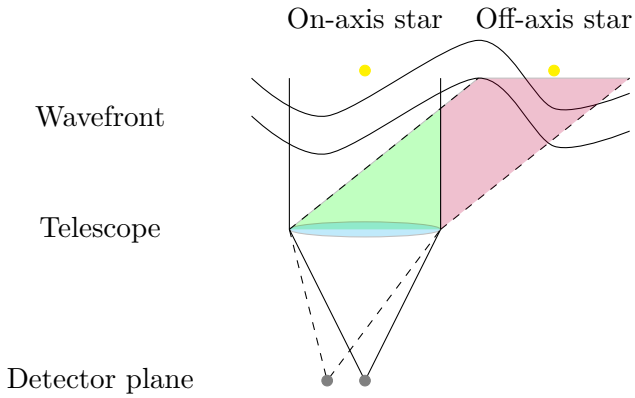

Figure 3.9 A SCAO system with an on-axis star used for wavefront sensing to correct an off-axis star. The area highlighted in green is the atmosphere which is common to both the on-axis guide star and off-axis star, and is seen by the WFS. The area highlighted in red is the atmosphere which is unique to the off-axis star, and is not seen by the WFS.

The WFS is not able to sense the off-axis atmospheric turbulence and therefore the AO system cannot compensate for it. This effect is known as angular anisoplanatism and is covered in more detail in Section 3.7.4.

If a wider FOV is to be corrected, then measurements of the wavefront need to include the entire atmospheric volume that starlight passes through, as well as more DMs conjugated to different layers in the atmosphere. To achieve AO corrections over a wide FOV, several guide sources are used. The guide sources can be natural or laser guide stars or a combination of both, with several WFSs. With several WFSs, tomographic reconstruction of the atmosphere is possible, and prominent turbulence layers can be identified. These individual layers are then used to control individual DMs that are conjugated to different altitudes (layers) in the atmosphere. Such a system is known as Multi Conjugate Adaptive Optics (MCAO) [Roddier 1999] and is shown in Figure 3.10.

3.5 WAVEFRONT SENSING

3.5.1 Shack-Hartmann wavefront sensor

The Shack-Hartmann (SH) WFS is widely used in AO systems today [Hickson 2014], particularly for WFS with laser guide stars. Figure 3.11 shows the operation of the SH WFS. A lenslet array is used to sub-divide the pupil plane, with each lenslet forming a low-resolution image of the object (a spot). If the incoming wavefront is planar, the spot will appear directly beneath each lenslet. If the incoming wavefront is aberrated, then the spot will shift from the centre of the lenslet by an amount proportional to the wavefront slope over that lenslet. By measuring the spot shift, the slope of the wavefront at each lenslet can be calculated [van Dam 2002]. The centroid, $(\hat{u}, \hat{v})$, of each spot within the bounds of the lenslet can be estimated with a centre of gravity

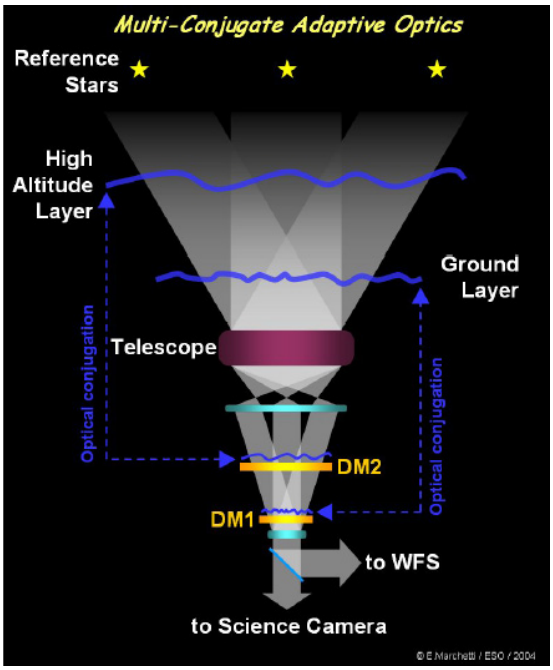

Figure 3.10 A simplified schematic of an MCAO system. Measurements from multiple wavefront sensors are used to control multiple DMs conjugated to different layers in the atmosphere [Hubin et al. 2006].

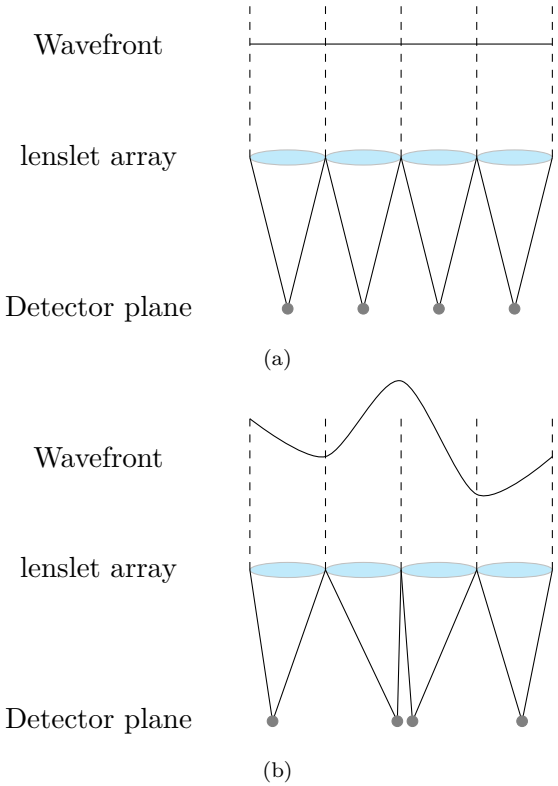

Figure 3.11 The Shack-Hartmann WFS with a planar wavefront (a) and with an aberrated wavefront (b).

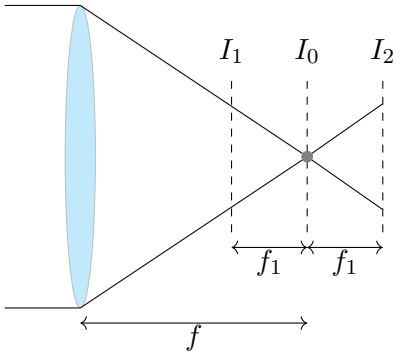

Figure 3.12 The curvature and geometric WFS need an intra (I_1) and extra (I_2) focal plane image, which are f_1 away from the focal point. I_0 is the image at the focal plane.

algorithm

$$\hat{u} = \frac{\sum_u \sum_v uA(u,v)}{\sum_u \sum_v A(u,v)}, \tag{3.31}$$

$$\hat{v} = \frac{\sum_u \sum_v vA(u,v)}{\sum_u \sum_v A(u,v)}, \tag{3.32}$$

where $A(u,v)$ is the image formed by one lenslet.

3.5.2 Geometric and curvature wavefront sensors

The geometric and curvature wavefront sensors use the same optical configuration, but differ in how the measurement data is processed. Two measurements are needed: an intra-focal image and an extra-focal image as illustrated in Figure 3.12. The intra- and extra-focal images, in effect, provide some phase diversity. Phase variations manifest as intensity changes in the measured images. By analysing how the intensity pattern differs between the intra- and extra-focal images, properties of the wavefront can be derived. For the curvature WFS, the curvature of the wavefront can be derived directly and is particularly useful with bimorph DMs [Roddier 1988]. For the geometric WFS, the x and y slopes of the wavefront can be derived [van Dam and Lane 2002].

3.5.3 Pyramid wavefront sensor

The pyramid wavefront sensor was first introduced in 1996 [Ragazzoni 1996]. Since then, the pyramid wavefront sensor has gained popularity with next-generation telescope systems due to its improved performance in closed-loop [Chew et al. 2006, Esposito and Riccardi 2001]. The pyramid WFS works by placing a 4-sided prism at a telescope's focal plane, which has the effect of subdividing the focal plane into four quadrants [Ragazzoni 1996].

Figure 3.13 shows how a pyramid wavefront sensor is placed into an optical system. A relay lens is used at the output of the prism to focus on to a charge-coupled device

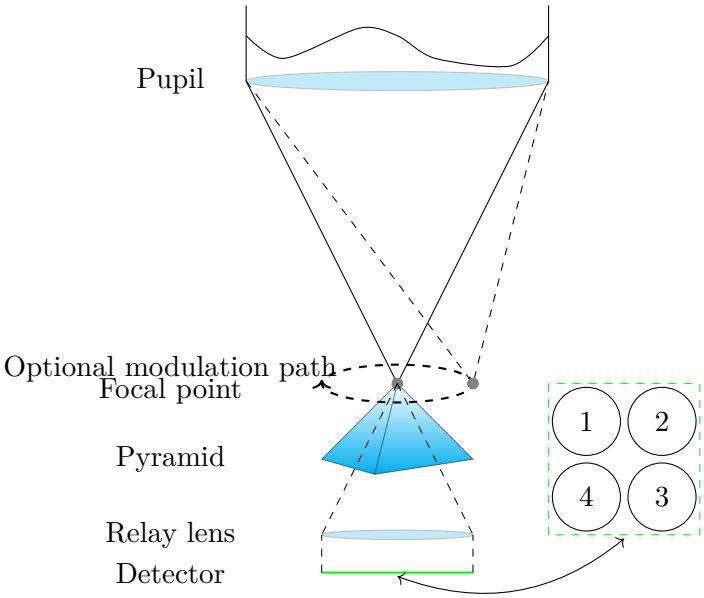

Figure 3.13 Schematic of the pyramid WFS. A 4-sided prism (pyramid) is placed in the focal plane of the telescope. Starlight travels through the atmosphere and becomes distorted. The pupil focuses the light onto the apex of the pyramid. The pyramid subdivides the focal plane into quadrants. The output from the prism is focused onto a detector by the relay lens, forming four images of the pupil. The focal point can be modulated around the apex of the pyramid, as shown by the dotted circle, to improve the dynamic range.

(CCD) sensor. Four images of the pupil are formed on the CCD, at the conjugate pupil plane. The prism can be described as a spatial filter, $H(u, v)$. The conjugate pupil plane, $I(x, y)$, is defined as [Esposito and Riccardi 2001]:

$$I(x,y) = \left| \mathcal{F}^{-1}\left[H(u,v) \times \mathcal{F}\left[P(x,y)\exp[j\phi(x,y)] \right] \right] \right|^2 . \tag{3.33}$$

By making use of the convolution theorem and the linearity of the Fourier transform, the conjugate pupil plane can be written as a convolution [Clare and Lane 2003]

$$I(x,y) = \left| h(x,y) \odot P(x,y)\exp[j\phi(x,y)] \right|^2 , \tag{3.34}$$

where $h(x, y)$ is the inverse Fourier transform of $H(u, v)$. The spatial filter for the pyramid WFS, $H_4(u, v)$, is defined by [Clare et al. 2017]

$$H_4(u,v) = \exp[j2\pi b(|u| + |v|)], \tag{3.35}$$

where b controls the pupil images' separation in the conjugate pupil plane (or the apex angle of the prism). Figure 3.14 shows the prism phase screen for a pyramid WFS.

Using the pyramid spatial filter, $H_4(u, v)$, Figure 3.15 shows the conjugate pupil plane where four pupil images have formed, for a flat wavefront. From these conjugate

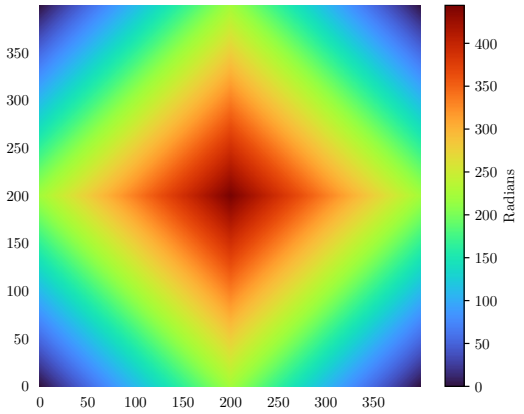

Figure 3.14 The phase of the pyramid WFS spatial filter, $H_4(u, v)$.

pupil images, the wavefront slopes, (S_x, S_y) are calculated as [Verinaud 2004]:

$$S_x = \frac{I_1(x,y) - I_2(x,y) - I_3(x,y) + I_4(x,y)}{\sum_{i=1}^{4} I_i(x,y)} \tag{3.36}$$

$$S_y = \frac{I_1(x,y) + I_2(x,y) - I_3(x,y) - I_4(x,y)}{\sum_{i=1}^{4} I_i(x,y)}. \tag{3.37}$$

The pyramid WFS has a small dynamic range, when compared to a Shack-Hartmann WFS, because the sensor is only in the linear region when the focal spot is near the apex of the pyramid [Clare and Lane 2005]. A method to overcome the limited dynamic range is to modulate the focal point around the tip of the pyramid and the detector image is summed over each modulation point [Clare and Le Louarn 2011]. This modulation trades sensitivity for dynamic range. The spatial filter is shifted by (u', v') giving a new spatial filter $H(u-u', v-v')$. Using the inverse Fourier transform and the Fourier shift theorem, the spatial filter of a modulated prism is written as $h(x,y)\exp[j2\pi x u']\exp[j2\pi y v']$ [Clare et al. 2017]. Different modulation paths can be used (i.e. square, circular). Ragazzoni has shown that the square modulation path is optimal for the pyramid sensor [Ragazzoni 1996]. The images formed in the complex aperture plane from a modulated prism are the continuous summation of the images formed over the modulated path R

$$\begin{aligned} I(x,y) = \oint_R \Big| & h(x,y)\exp[j2\pi x u']\exp[j2\pi y v'] \\ & \odot P(x,y)\exp[\phi(x,y)]\Big|^2 \mathrm{d}u'\mathrm{d}v'. \end{aligned} \tag{3.38}$$

The pyramid WFS exhibits non-linear behaviour, especially in the presence of closed-loop AO residual wavefront error [Deo et al. 2018, Korkiakoski et al. 2008]. The non-linearity manifests as a spatial frequency (modal) dependent loss in sensitivity. A

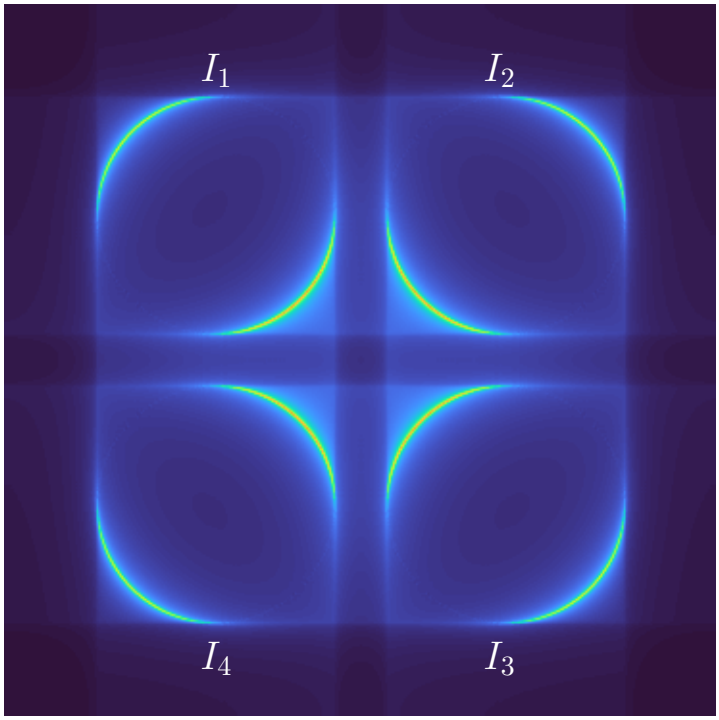

Figure 3.15 The detector plane (or conjugate aperture plane) of a pyramid WFS with spatial filter, $H_4(u, v)$.

pyramid WFS is typically calibrated about a zero-phase point, however in operation, the "zero-point" is the closed-loop residual phase, resulting in a sensitivity loss. An illustration of this loss in sensitivity is shown in Figure 3.16. The so-called optical gains represent this loss in sensitivity. The optical gains can be calibrated as [Chambouleyron et al. 2020]

$$OG = \frac{diag(F_{\text{res}}^T \cdot F_{\text{diff}})}{diag(F_{\text{diff}}^T \cdot F_{\text{diff}})}, \tag{3.39}$$

where F_{res} is the modal interaction matrix in the presence of AO residual, F_{diff} is the diffraction-limited modal interaction matrix and OG are the modal optical gains.

3.6 DEFORMABLE MIRRORS

A DM is a mirror where the shape of the mirror surface is controlled via actuators, in real-time. AO systems make use of DMs as the means of correcting the wavefront of starlight propagating through Earth's atmosphere. Several different technologies enable DMs, such as piezoelectric actuators, micro-electro-mechanical machines (MEMs) actuators and voice-coil actuators. There are four critical parameters which characterise a DM: the number of actuators, the actuator pitch, the actuator stroke and the actuator influence function. The actuator pitch describes the spacing between actuators, and along with the number of actuators, ultimately defines the maximum spatial frequency

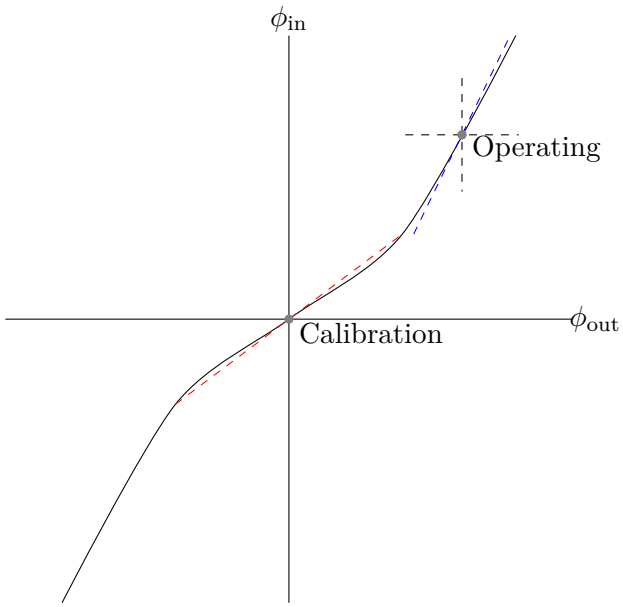

Figure 3.16 A representation of the linear approximation of the pyramid WFS about the diffraction-limited calibration point (red), and the linear approximation of the pyramid WFS opearting with closed-loop AO residuals (blue). The ratio of the gradients of the red and blue lines is the so-called optical gain.

controllable. The actuator stroke is the maximum displacement of an actuator, and the actuator influence function gives the mirror shape when a single actuator is poked.

3.6.1 Piezoelectric mirrors

There are two main kinds of piezoelectric DMs: bimorph mirrors [Horsley et al. 2007] and piezoelectric stack actuated mirrors [Wlodarczyk et al. 2014]. A bimorph DM is formed by bonding two piezoelectric disks together. The middle point of the disks has an electrode attached, the front side has an electrode attached, and the backside has an electrode array for each actuator. A differential voltage is applied between the midpoint and the top and bottom disks, causing the disks to curve. A thin mirror surface is bonded to the top disk. Piezoelectric stacks can be formed and used as single actuators. An array of piezoelectric stacks are attached to a thin mirror membrane; each actuator can push or pull on the membrane to control the shape.

3.6.2 MEMs mirrors

A MEMs DM is one which is manufactured using methods from microelectronic device fabrication. Multi-layer structures can be fabricated on a silicon wafer to form electrostatic actuators [Bifano et al. 2000]. MEMS DMs are an important technology as they utilise standard microelectronic mass production technologies and could therefore be mass-produced, which would significantly reduce the cost compared to DMs of similar

capabilities of other technologies. MEMs-based DMs typically have an actuator stroke in the order of a few to tens of micrometres.

3.6.3 Voice-coil actuators

For large diameter DMs, typically used as the secondary mirror of a telescope, an array of voice-coils actuators are used. Voice-coil actuators have three main components: a permanent magnet, an electromagnet and a capacitive displacement sensor [Arsenault et al. 2006, Martin et al. 2006]. The permanent magnet is bonded to a thin (1 mm to 2 mm) membrane (typically glass), and the electromagnet is bonded to a reference body. A capacitor is formed between the permanent magnet and the electromagnet. By measuring the capacitance, the distance from the reference body to the permanent magnet can be derived to accuracies on the order of nanometres. The voice-coil actuators used in the DMs are operated in closed-loop, where the current through the voice-coils is regulated to maintain a set separation between the permanent magnet and the reference body.

Voice-coil actuated DMs are currently in use at the Large Binocular Telescope [Martin et al. 2006] and the Very Large Telescope [Arsenault et al. 2006]. The main DM of the EELT will also use a voice-coil actuated DM and is specified to have a diameter of 2.4m and 5316 actuators [Vernet et al. 2012].

3.7 WAVEFRONT ESTIMATION AND CONTROL

So far, all the major components of an AO system have been introduced. This section brings all the components together into a closed-loop AO system.

3.7.1 The forward problem

Due to the variations in the refractive index in the atmosphere, as described in Section 3.2, the wavefront becomes distorted by the time it reaches the ground. A telescope with a WFS is used to make measurements from which the wavefront can be estimated. Assuming a linear system, the WFS measurement can be expressed as

$$\mathbf{d} = F\mathbf{w} + n, \tag{3.40}$$

where $\mathbf{d}$ is the measurement from the WFS, F is the interaction matrix, $\mathbf{w}$ is modal coefficients of the wavefront, and n is measurement noise. The interaction matrix provides a mapping between WFS measurements and the DM commands of a known wavefront. The interaction matrix can be found experimentally or via simulations. Using the DM, a set of known wavefronts (the selected basis, modal or zonal) are shown to the WFS, one at a time, and the resulting measurements are stored as rows in the

interaction matrix. In the case of the pyramid and Shack-Hartmann WFSs, where the measurement consists of an x and y-slope, the slopes are vectorised and concatenated together to form a single measurement vector. An interaction matrix consisting of x and y slopes can be expressed as

$$\mathbf{F} = \begin{bmatrix} S_{x_1} & S_{y_1} \\ \vdots & \vdots \\ S_{x_N} & S_{y_N} \end{bmatrix}, \tag{3.41}$$

where S_x and S_y are the slopes in the x and y directions respectively, and N is the number of basis elements in the wavefront discretisation.

3.7.2 The inverse problem

The forward problem has been outlined in Section 3.7.1. The inverse problem is to estimate the modal coefficients of the wavefront, $\mathbf{w}$, from WFS measurements and the associated interaction matrix, which can be expressed as

$$\mathbf{w} = F^{-1}\mathbf{d}. \tag{3.42}$$

However, the interaction matrix is typically non-invertible as it is poorly conditioned. The WFS measurement can instead be rewritten as

$$\mathbf{w} = B\mathbf{d}, \tag{3.43}$$

where B is the Moore-Penrose inverse of F. B is defined as

$$B = (F^T F)^{-1} F^T. \tag{3.44}$$

A better method of finding the command matrix is with a *maximum a posteriori* (MAP) estimator, where the statistics of the atmosphere and statistics of system noise are taken into account [Clare et al. 2011, Clare 2004]. A MAP estimator is given by:

$$B = (F^T N^{-1} F + W^{-1})^{-1} F^T N^{-1}, \tag{3.45}$$

where $N = \langle nn^T \rangle$ is the covariance of the noise, and $W = \langle ww^T \rangle$ is the covariance of the turbulent wavefront [Clare et al. 2011, Clare 2004].

The estimators described here are matrix vector multiplication (MVM) algorithms, which are computationally expensive to run. A 37 m diameter telescope will require between 256-4096 times more computation than that of the current 8 m diameter telescopes [Hubin et al. 2006]. What was manageable for the 8 m case is no longer easily achieved in the ELT cases. There are other methods such as the cumulative reconstructor

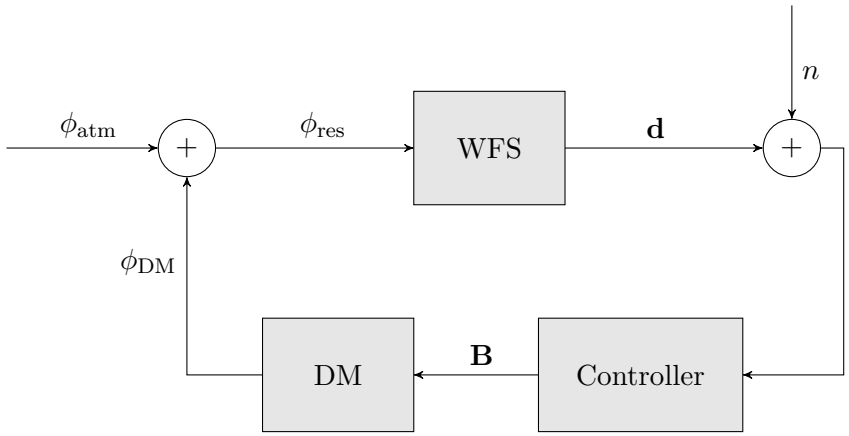

Figure 3.17 A simplified block diagram of an AO control system, where ϕ_{atm} is the phase of the atmospheric turbulence, ϕ_{DM} is the phase after correction from the DM and ϕ_{res} is the residual phase ($\phi_{atm} - \phi_{DM}$).

with domain decomposition (CuReD) algorithm [Rosensteiner 2012], which avoid the use of MVM in the wavefront estimation and provide a computational advantage. The CuReD reconstructor is designed for the Shack-Hartmann WFS and is based on the fact that the Shack-Hartmann WFS provides a discrete estimate of the wavefront slope, therefore, the reconstruction can be made via an integration.

The preprocessed cumulative reconstructor with domain decomposition (PCuReD) reconstructor is an implementation of the CuReD reconstructor for the pyramid WFS. The Shack-Hartmann and pyramid WFS are effectively a Fourier pair; the Shack-Hartmann subdivides the pupil, whilst the pyramid subdivides the focal plane. The preprocessing step of the PCuReD algorithm transforms the pyramid WFS measurements into the Shack-Hartmann form, then the CuReD algorithm is used to reconstruct the wavefront [Shatokhina et al. 2013]. Typical matrix-vector-multiplication reconstructors have a complexity of $O(n_a^2)$, where n_a is the number of DM actuators. The PCuReD reconstructor has a complexity of $O(n_a)$.

3.7.3 Adaptive optics control loop

A typical closed-loop AO system is shown in Figure 3.17. The WFS does not measure the wavefront, but rather the residual wavefront after correction. A simple integrator control loop is adequate for closed-loop wavefront control. The controller takes the form of:

$$C = C_{k-1} + gC_k, \tag{3.46}$$

where C is the command vector going to the DM, k represents the time step, and g is the integrator gain.

More complex controllers can be used to improve performance and are currently under investigation, such as linear-quadratic regulators [Petit et al. 2010] and predictive

control [Le Roux and Carbillet 2006].

3.7.4 Error sources

3.7.4.1 Fitting and temporal error

A real-world AO system is not able to perfectly correct the atmospheric turbulence. In this thesis, two main error sources are considered when evaluating AO performance in a high flux regime: fitting error and temporal error. The variance of the residual turbulence σ^2_{tot} is then

$$\sigma^2_{\text{tot}} = \sigma^2_{\text{fit}} + \sigma^2_{\text{temp}}, \tag{3.47}$$

where σ^2_{fit} is the residual variance due to fitting errors and σ^2_{temp} is the residual variance due to time delays in the AO system.

The fitting error, σ^2_{fit}, is given by [Béchet et al. 2008]

$$\sigma^2_{\text{fit}} = 0.26\left(\frac{d}{r_0}\right)^{5/3}, \tag{3.48}$$

where d is proportional to the actuator pitch of the DM.

The temporal error is given by [Béchet et al. 2008]

$$\sigma^2_{\text{temp}} = 6.88\left(\frac{V\tau}{r_0}\right)^{5/3}, \tag{3.49}$$

where V is the characteristic wind speed and τ is the AO system delay. The fitting error is due to the limited resolution of the DM, and the temporal error is due to time differences between when the wavefront measurement is made to when the correction is applied to the DM. Using Equation (3.47), the theoretical performance of a given SCAO system can be estimated at high flux.

3.7.4.2 Anisoplanatism

In many cases, the science target is not used for wavefront sensing due to the low signal to noise ratio. In this scenario, a nearby bright star can be used for wavefront sensing. An issue with this is that the off-axis starlight propagates through a different section of atmosphere as shown in Figure 3.9, and is known as angular anisoplanatism. The isoplanatic angle, θ_0, is defined as the angle between an off-axis star and an on-axis guide star which produces a mean squared error in phase of 1 rad^2 and is defined as [Fried 1982]

$$\theta_0 = \left[58 \times 10^{-3}\, \lambda^{6/5} \int_0^\infty C_n^2(z) z^{\frac{5}{3}} dz\right]^{-\frac{3}{5}}. \tag{3.50}$$

Chapter 4

AN N-SIDED PRISM WAVEFRONT SENSOR

In Chapter 3, Section 3.5.3 the pyramid WFS was introduced. The pyramid WFS is a special case of a set of Fourier-based wavefront sensors [Fauvarque et al. 2016, 2017], where a 4-sided prism is used to filter the focal plane electromagnetic field. This chapter extends the pyramid WFS to an N-sided prism. Using analytical models, Fauvarque et al. [Fauvarque et al. 2016, 2017] predict, in a high flux regime, that there is no significant gain in performance by changing the prism geometry. In the case of the pyramid WFS, using only geometric considerations, the wavefront slope in two orthogonal directions (x and y) can be derived from the detector image. For the 3-sided, 6-sided and cone WFS, calculating slopes is more difficult.

Changing the prism geometry from 4-sided could reduce manufacturing costs [van Dam et al. 2012], reduce the required detector area, and possibly increase the sensitivity of the WFS. As long as there are three or more sides to the prism, wavefront slopes in two orthogonal directions (x and y) can be derived. In this chapter, the roofs (two orthogonal 2-sided prisms), 3-sided prism, the conventional pyramid prism, and 6-sided prisms are simulated with the European Southern Observatory's (ESO) Octopus [Le Louarn et al. 2004] end-to-end simulation platform.

To investigate the performance of different Fourier-based prism WFSs with different prism geometries, it is first necessary to define how the prism geometry is generated in simulation. There are two parameters which need to be considered: the first is the number of sides on the prism and the second is the apex angle of the pyramid. The apex angle determines the separation of the conjugate pupils in the detector plane [Clare and Lane 2003]. In Chapter 3, the equations which describe the detector plane, $I(x, y)$, are derived, and repeated here for clarity

$$I(x,y) = \left| \mathcal{F}^{-1}\left[H(u,v) \times \mathcal{F}\left[P(x,y) \exp[j\phi(x,y)] \right] \right] \right|^2 . \tag{4.1}$$

The complex field $H(u, v)$, of the Fourier WFS, can be expressed as

$$H(u,v) = e^{j\phi_{prism}(u,v)}, \tag{4.2}$$

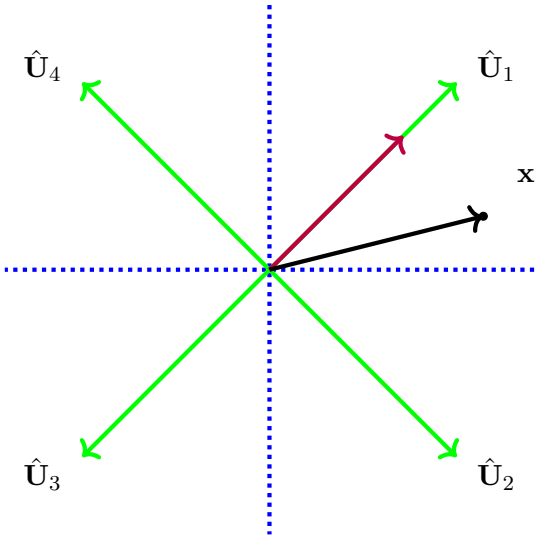

Figure 4.1 The method used for generating an N-sided prism spatial filter. The direction vectors, $\mathbf{U}(u, v)$ (green), point in the direction of the slope of the prism faces and the dotted lines are the prism edges. Point $X(u, v)$ is a pixel in the spatial filter phase and the red vector is the projection of X onto the direction vector. The phase at each pixel on the spatial filter is the magnitude of the dot product of X (black) and the direction vector.

where $\phi_{prism}(u, v)$ is the phase shift introduced by the prism. A method for generating the N-sided WFS spatial filter, $H(u, v)$, as a function of the number of sides of the prism, N, and the separation of the pupil images in the conjugate pupil plane is proposed here. For each face of the prism, a unit direction vector is created, $\mathbf{U_n}$, (Figure 4.1, green vector), pointing in the direction of the slope of the prism face. A vector, $\mathbf{x} = (u, v)$, (Figure 4.1, black vector) is formed, pointing from the origin to a position in the spatial filter $H(u, v)$ (Figure 4.1, red vector). The value for every pixel in the spatial filter is defined as,

$$\phi_{prism} = \frac{b}{\sin(\frac{\pi}{N})} \max(\hat{\mathbf{U}}_1 \cdot \mathbf{x}, \cdots, \hat{\mathbf{U}}_n \cdot \mathbf{x}, \cdots, \hat{\mathbf{U}}_N \cdot \mathbf{x}), \tag{4.3}$$

where b defines the slope of the prism faces.

4.0.1 Roofs WFS

The roofs WFS consists of two orthogonal 2-sided prisms. A 50:50 beamsplitter is used to provide two focal points, and a 2-sided prism is placed at each focal point. The reduced complexity of the 2-sided prism also improves manufacturability. The roofs WFS requires two detectors; however, the area of each detector is reduced when compared to a pyramid WFS. The roofs sensor has been shown theoretically to be more sensitive than a pyramid WFS [Phillion and Baker 2006, Wang et al. 2010].

The phase of the spatial filters, $H_{2x}(u, v)$ and $H_{2y}(u, v)$, and the simulated detector images are shown in Figure 4.2. For the roof WFS, the slope measurements, (S_x, S_y), can be calculated by resolving vectors between aperture images in the conjugate aperture

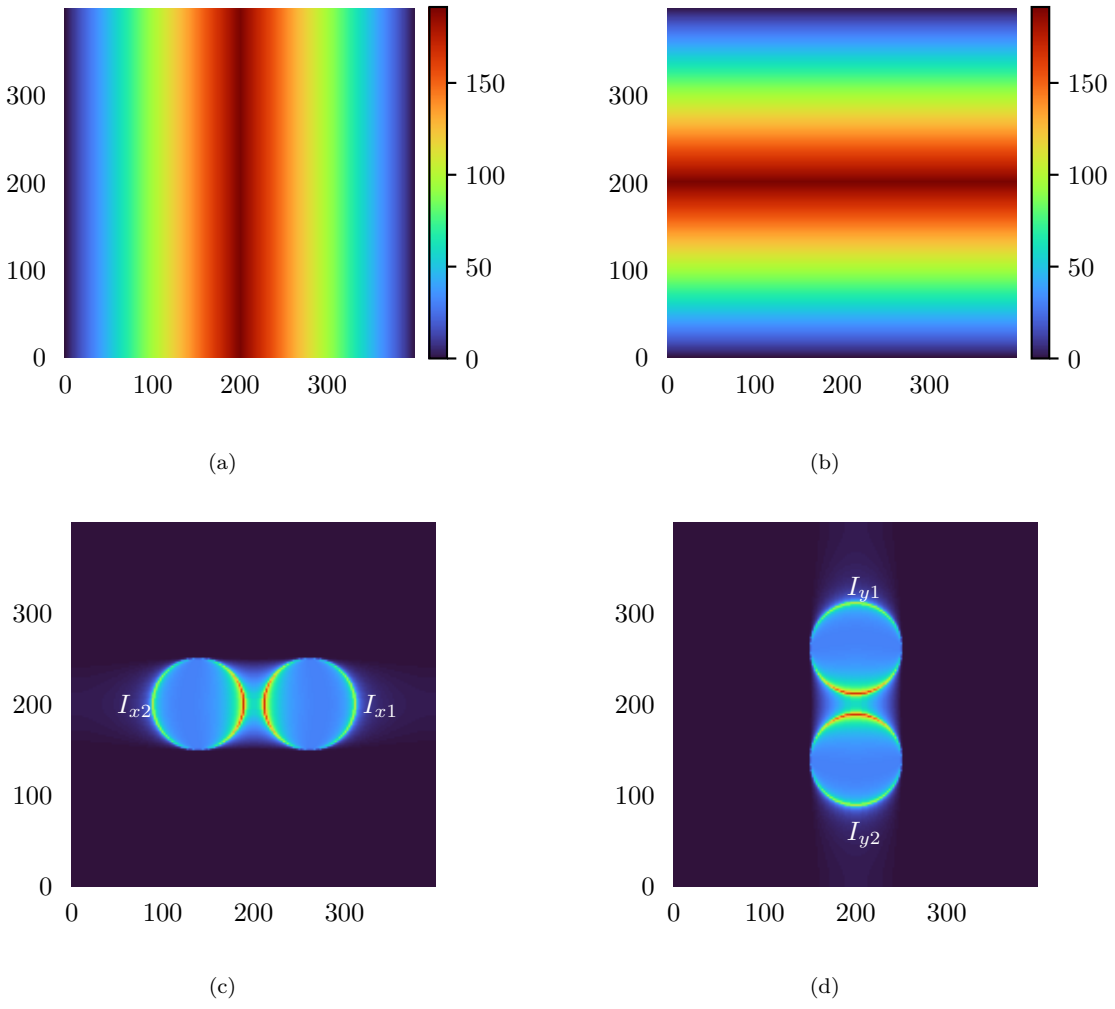

Figure 4.2 The phase, ϕ_{prism}, of the spatial filters $H_{2y}(u, v)$ (a) and $H_{2x}(u, v)$ (b) in radians, for the roofs WFS and the corresponding detector images (c, d).

plane into x and y components. For the roof WFS, the slopes measurements are given by

$$S_x = \frac{I_{x1}(x,y) - I_{x2}(x,y)}{\sum_{i=1}^{2} I_{xi}(x,y)}$$

$$S_y = \frac{I_{y1}(x,y) - I_{y2}(x,y)}{\sum_{i=1}^{2} I_{yi}(x,y)}. \tag{4.4}$$

4.0.2 3-sided WFS

The 3-sided WFS has two potential advantages over the roofs WFS: a beamsplitter is not required, and a single detector can be used. Similarly to the 2-sided prisms of the roofs WFS, the 3-sided prism is simpler to manufacture than the traditional 4-sided prism. The 3-sided WFS subdivides the pupil into three, rather than four for the pyramid and roofs WFS, limiting its ability to estimate the x and y slopes. Using the WFS to estimate slopes differs from the performance metrics used in [Fauvarque et al. 2016], which uses the intensity maps, $I(x,y)$, directly.

The phase of the spatial filter, $H_3(u,v)$, and the simulated detector image are shown in Figure 4.3. From the detector image, the slope measurements for the 3-sided prism are given by [Clare and Lane 2003]

$$S_x = \frac{\frac{\sqrt{3}}{2}\Big(2I_3(x,y) - I_2(x,y) - I_1(x,y)\Big)}{\sum_{i=1}^{3} I_i(x,y)}$$

$$S_y = \frac{\frac{3}{2}\Big(I_1(x,y) - I_2(x,y)\Big)}{\sum_{i=1}^{3} I_i(x,y)}\,. \tag{4.5}$$

4.0.3 6-sided WFS

The EELT will have a 6-arm spider which supports the secondary mirror [Schwartz et al. 2017]. Therefore a 6-sided prism matches the physical geometry of the EELT pupil.

The phase of the spatial filter, $H_6(u,v)$, and the simulated detector image are shown in Figure 4.4. From the detector image, the slope measurements for the 6-sided prism

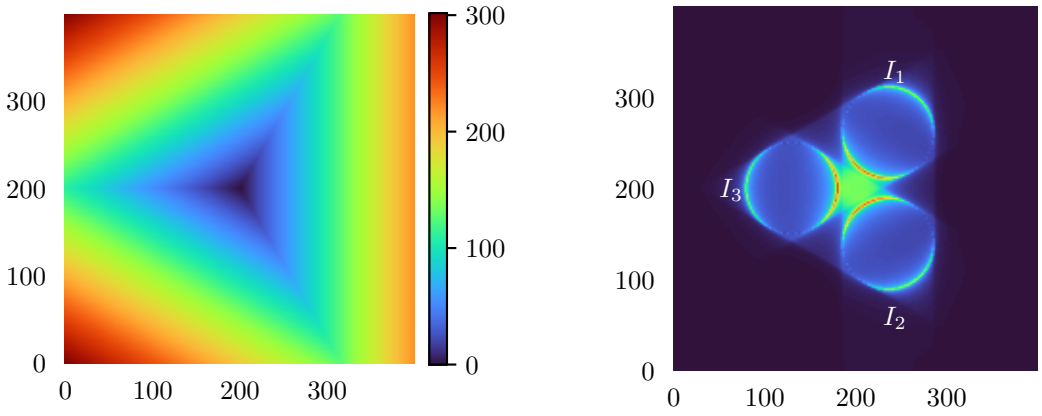

(a) (b)

Figure 4.3 The phase, ϕ_{prism} of the spatial filter, $H_3(u, v)$, for the 3-sided WFS in radians (a) and the corresponding detector image (b).

are given by

$$S_x = \frac{(I_1(x,y) + I_2(x,y) + I_3(x,y)) - (I_4(x,y) + I_5(x,y) + I_6(x,y))}{\sum_{i=1}^{6} I_i(x,y)}$$

$$S_y = \frac{(I_1(x,y) + I_6(x,y)) - (I_4(x,y) + I_3(x,y))}{\sum_{i=1}^{6} I_i(x,y)}. \tag{4.6}$$

4.0.4 Cone WFS

The cone WFS extends the number of sides of the prism to infinity. Previously, it has been shown that an axicon can be used to make wavefront measurements [Fauvarque et al. 2016, 2017, Vohnsen et al. 2011]. An axicon is a cone-shaped lens. The phase of the spatial filter, $H_\infty(u, v)$, and the simulated detector image are show in Figure 4.5.

The cone WFS presents an additional challenge when calculating the x and y slopes as discrete pupil images are no longer formed, but rather a continuous annulus. It is possible to estimate the wavefront by building an interaction matrix of WFS detector images instead of slopes. Ilovitsh et al. have shown that an axicon and an amplitude mask placed in the focal plane produces the Radon transform of the pupil plane at the WFS detector plane [Ilovitsh et al. 2014]. Using the inverse Radon transform, it is possible to estimate the wavefront directly from the cone WFS detector images. The slopes calculation step can skipped, and the entire detector image can be used to directly reconstruct the wavefront. Both the inverse Radon transform and the reconstruction from detector images of the cone WFS have been explored by Clare et al. [Clare et al.

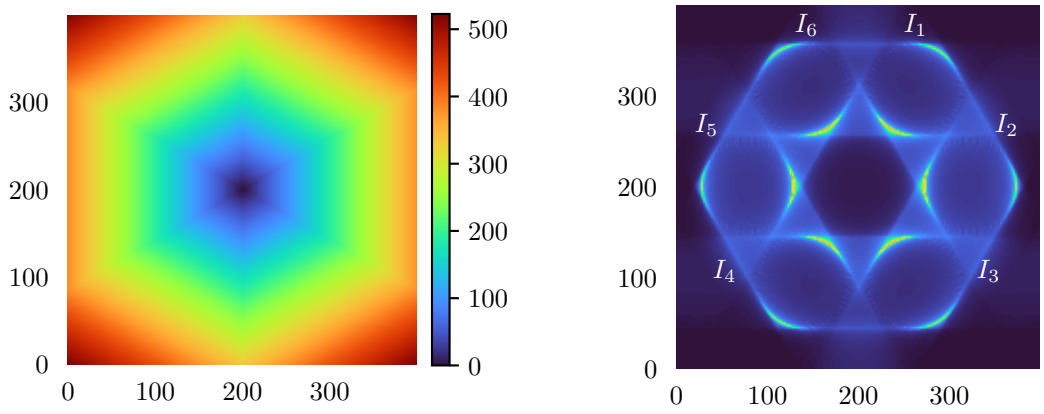

(a) (b)

Figure 4.4 The phase, ϕ_{prism}, of the spatial filter $H_6(u, v)$, for the 6-sided WFS in radians (a) and the corresponding detector image (b).

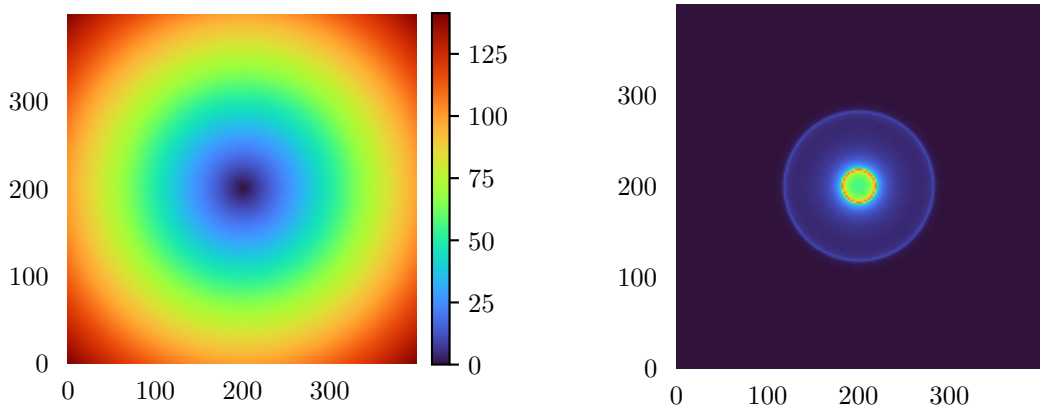

(a) (b)

Figure 4.5 The phase, ϕ_{prism}, of the spatial filter $H_\infty(u, v)$, for the cone WFS in radians (a) and the corresponding detector image (b).

2020].

4.1 END-TO-END SIMULATIONS

For the roofs, 3-sided, pyramid and 6-sided prism WFS, closed-loop end-to-end simulations were performed using the OCTOPUS simulation tool. OCTOPUS generates atmospheric phase screens for different layers of the atmosphere. The Fried coherence length, r_o, and the outer scale, L_0, which define the severity of the turbulence in the atmosphere, are listed in Table 4.1 and Table 4.2. The layer composition is defined from site measurements. These atmospheric phase screens are then shifted to simulate wind flow at each of the layers. After each shift, the WFS images, $I(x, y)$, are calculated, including readout noise and photon noise. The WFS detector images are used to estimate the slopes, (S_x, S_y), of the wavefront using Equation (4.4), Equation (4.5) or Equation (4.6), which are then used to command the DM. Two different wavefront reconstructors are evaluated: the first method is a matrix-vector-multiplication method, using the *maximum a posteriori* (MAP) reconstructor from Chapter 3,

$$B = (F^T N^{-1} F + W^{-1})^{-1} F^T N^{-1}, \tag{4.7}$$

where $N = \langle nn^T \rangle$ is the covariance of the noise, and $W = \langle ww^T \rangle$ is the covariance of the turbulent wavefront, w. The second method is the preprocessed Cumulative Reconstructor with domain decomposition (pCuReD) method. The noise covariance matrix is a diagonal matrix described as

$$N = \begin{bmatrix} \sigma_n^2 & & 0 \\ & \ddots & \\ 0 & & \sigma_n^2 \end{bmatrix}, \tag{4.8}$$

where σ_n^2 is defined as

$$\sigma_n^2 = \frac{\pi^2}{2ln(2)} \frac{1}{N_p} \left(\frac{\theta}{\theta_d} \right)^2, \tag{4.9}$$

where θ is the FWHM of the PSF, N_p is the regularisation photon flux and θ_d is the full width at half maximum (FWHM) of the diffraction-limited PSF [Clare et al. 2011]. By adjusting this regularisation flux, the weighting between the measurement and the wavefront statistics is changed when reconstructing the wavefront.

A closed-loop system is formed where the performance of the WFS can be evaluated. In this thesis, OCTOPUS has been configured to simulate the roofs, 3-sided and 6-sided prism WFSs along with the existing 4-sided pyramid WFS. The closed-loop controller used in OCTOPUS is an integrator controller, which takes the form of

$$B = B_{k-1} + gB_k, \tag{4.10}$$

where B is the command vector going to the DM, k represents the time step, and g is the integrator gain.

4.1.1 Simulation parameters

Two simulation cases are considered: 8 m and 37 m telescope diameters. The 8 m case is a scaled down version of the full 37 m case, and has significantly lower complexity and is used to explore and optimise the WFC performance for each sensor. Once the performance for each sensor is optimised, the 37 m EELT case is used to explore the performance in the expected ELT environment.

Along with exploring how the geometry of the WFS prism affects closed-loop performance, two different wavefront reconstructors, the traditional MAP reconstructor and the pCuReD reconstructor, are evaluated for the roofs and pyramid WFSs. The salient parameters of the simulations are shown in Table 4.1 and Table 4.2 for the 8 m and 37 m cases respectively.

The MAP reconstructor has a complexity of $O(n_a^2)$, where n_a is the number of DM actuators. The second method uses the pCuReD algorithm which has a complexity of $O(n_a)$ [Shatokhina et al. 2013].

Due to the physical size of the ELTs, the support structure (or spider) which holds the secondary mirror in place is also large. In the case of the EELT, the spider has six support arms with a thickness of 0.5 m. These spider arms have the effect of dividing the pupil into six segments (or petals). The width of the spider arms is greater than the typical coherence length of the atmosphere, or Fried parameter r_0, expected at the observatory sites. This introduces complexities in the wavefront estimation, as there is no phase continuity between the six pupil segments. Consequently, the average wavefront over each pupil segment (segment piston) is different.

For each simulation case, two pupil geometries are considered: pupils with and without a spider. For each case considered, the control-loop gain, g, and amount of regularisation used in the reconstructor are optimised for maximum long exposure Strehl after 1000 iterations in closed-loop.

4.1.2 Simulation results

To verify that the simulations are performing correctly in the case of high photon flux, the theoretical errors due to fitting and temporal error are calculated using the parameters from Table 4.1 and Table 4.2. The total wavefront error (fitting error and temporal error), for a high flux case, is calculated using Equation (3.47) and is found to be 116.5 nm RMS. The contribution from fitting error is 96.4 nm RMS and the contribution from temporal error is 20.1 nm. Figure 4.6 and Figure 4.9 show that

Table 4.1 Simulation parameters for the 8 m diameter simulation case.

Parameter	Value
Telescope Diameter (D)	8 m
Fried parameter (r_0)	12.9 cm
Outer Scale (L_0)	25 m
Atmosphere	ESO 9 layer model [Clare et al. 2011]
Central Obscuration Diameter	1.2 m
Frame Rate	3 kHz
Delay	2 Frames
WFS Wavelength (λ_W)	700 nm
WFS Order	40 × 40 Subapertures
Subaperture Width (d)	20 cm
Prism apex angle	26.4°
PSF Wavelength	2.2 µm
Modulation Width	4 λ_W/D
Time Steps	1000
Illumination Threshold	70%
Number of Actuators	1346
Number of Modes	1346
Number of Spider Arms	6
Spider Arm Width	20 cm

the simulation results are within 1% and 2% of the theoretical error, for both the 8 m and 37 m cases respectively.

For all scenarios, the measurement vector, d, consists of the x and y slopes, (S_x, S_y). In the case of the cone WFS, there is no existing method for calculating the slopes, (S_x, S_y), thus the cone is not included in these results.

4.1.2.1 The 8 m case

Simulations of the roofs, 3-sided, pyramid and 6-sided WFS are performed without the telescope spider in this section for the 8 m case. The performance metric used to compare the different WFSs is the long exposure Strehl after 1000 iterations in closed-loop. The results are plotted in Figure 4.6 and show that in a high photon flux scenario, the performance of the WFSs is similar. Under low photon flux, the 6-sided WFS performs poorly, which is due to the fact that the pupil (available photons) is subdivided more.

For the roofs and pyramid WFS, the pCuReD reconstruction technique is evaluated and is compared to the traditional MVM reconstructor. The comparison is plotted in Figure 4.7 and shows that the closed-loop long exposure Strehl from the pCuReD and the MVM reconstructors are within 1% of each other accross a broad range of photon flux. For a very small loss in performance, a significant reduction in computational load

Table 4.2 Simulation parameters for the 37 m Diameter simulation case.

Parameter	Value
Telescope Diameter (D)	37 m
Fried parameter (r_0)	12.9 cm
Outer Scale (L_0)	25 m
Atmosphere	ESO 35 layer model
Central Obscuration Diameter	10.4 m
Frame Rate	3 kHz
Delay	2 Frames
WFS Wavelength (λ_W)	700 nm
WFS Order	148 × 148 Subapertures
Subaperture Width (d)	25 cm
Prism apex angle	26.4°
PSF Wavelength	2.2 µm
Modulation Width	4 λ_W/D
Time Steps	1000
Illumination Threshold	70%
Number of Actuators	5190
Number of Modes	5190
Number of Spider Arms	6
Spider Arm Width	50 cm

is achieved.

Thus far, the simulations above have all neglected the telescope spider. The performance of the roofs, 3-sided, pyramid and 6-sided WFSs are re-evaluated in the presence of the telescope spider. The regularisation and integrator gain are re-optimised in the presence of the spider. The comparison is plotted in Figure 4.8 and shows an overall loss in performance compared to the case of no spider, especially in cases of low photon flux. This loss is attributed to residual segment piston errors and the obstruction of WFS subapertures which is investigated further in Chapter 6. At high flux, the 3-sided WFS performs the worst, while the pyramid WFS performs the best, with a difference in Strehl of 2.5%.

4.1.2.2 The 37 m case

Simulations of the roofs, 3-sided, and pyramid WFSs are performed without the telescope spider in this section for the 37 m case. The performance metric used to compare the different WFSs is the long exposure Strehl, after 1000 iterations in closed-loop. The results are plotted in Figure 4.9 and show that the roofs and pyramid WFS perform similarly and achieve the highest Strehl. The 3-sided WFS achieves a Strehl 4% lower than the roofs and pyramid WFS.

For the roofs and pyramid WFS, the pCuReD reconstructor's performance is

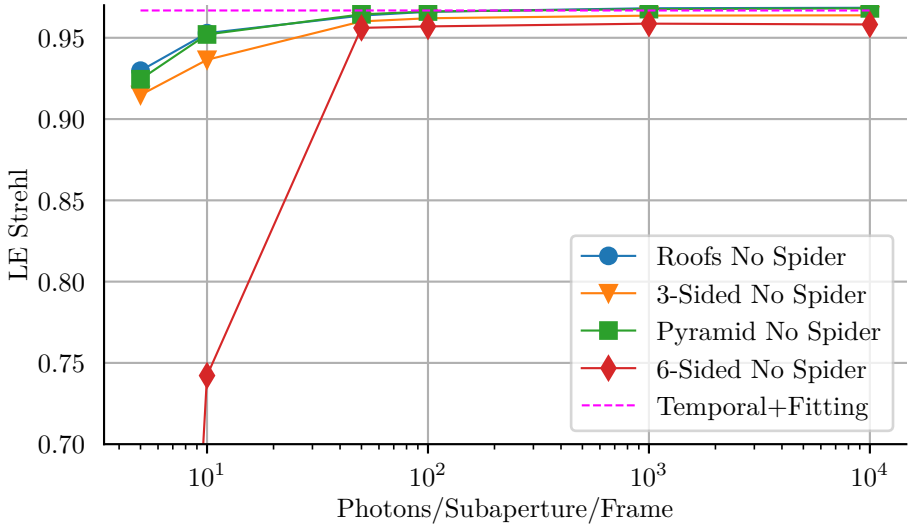

Figure 4.6 The long exposure Strehl in K-band versus the subaperture flux for a read noise of 0 electrons/pixel/read for the 8 m case, without the telescope spider, using the MVM reconstructor. The dashed line is the K-band Strehl corresponding to the sum of the temporal and fitting errors for this frame rate, controller delay and atmospheric conditions.

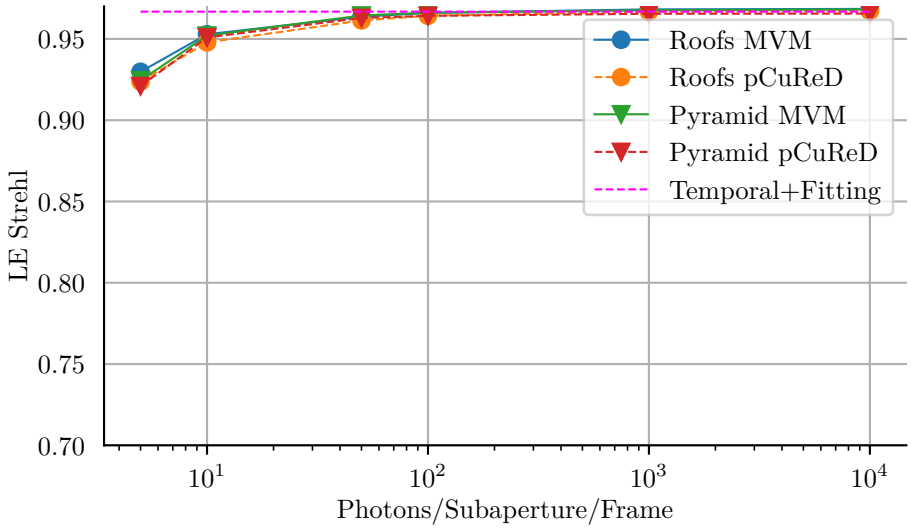

Figure 4.7 The long exposure Strehl in K-band versus the subaperture flux for a read noise of 0 electrons/pixel/read for the 8 m case, without the telescope spider, comparing the MVM reconstructor to the pCuReD reconstructor. The dashed line is the K-band Strehl corresponding to the sum of the temporal and fitting errors for this frame rate, controller delay and atmospheric conditions.

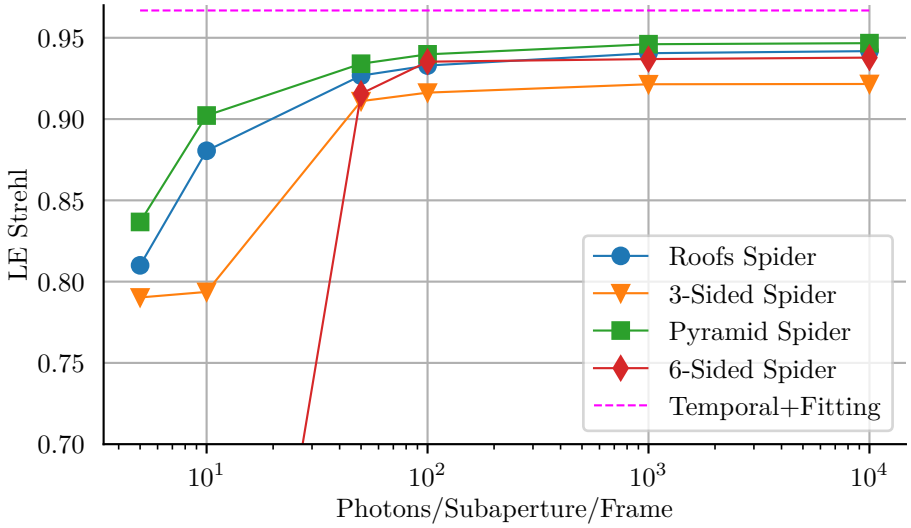

Figure 4.8 The long exposure Strehl in K-band versus the subaperture flux for a read noise of 0 electrons/pixel/read for the 8 m case, with the telescope spider, using the MVM reconstructor. The dashed line is the K-band Strehl corresponding to the sum of the temporal and fitting errors for this frame rate, controller delay and atmospheric conditions.

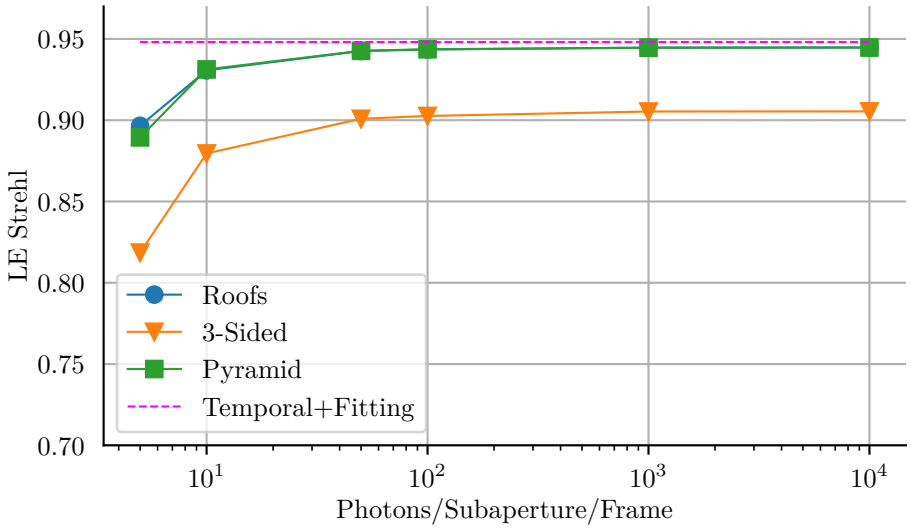

Figure 4.9 The long exposure Strehl in K-band versus the subaperture flux for a read noise of 0 electrons/pixel/read for the 37 m case, without the telescope spider, using the MVM reconstructor. The dashed line is the K-band Strehl corresponding to the sum of the temporal and fitting errors for this frame rate, controller delay and atmospheric conditions.

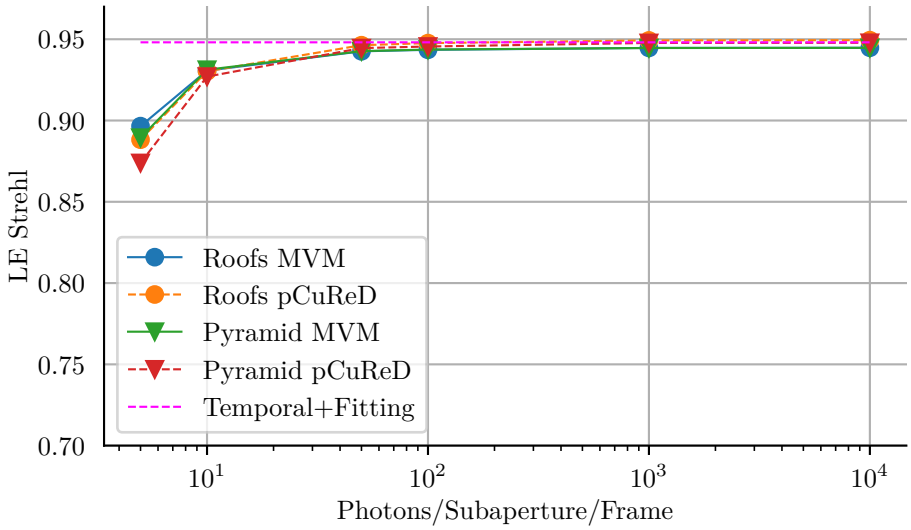

Figure 4.10 The long exposure Strehl in K-band versus the subaperture flux for a read noise of 0 electrons/pixel/read for the 37 m case, without the telescope spider, comparing the MVM reconstructor to the pCuReD reconstructor. The dashed line is the K-band Strehl corresponding to the sum of the temporal and fitting errors for this frame rate, controller delay and atmospheric conditions.

evaluated and compared to the traditional MVM reconstructor. The comparison is plotted in Figure 4.10 and shows that even for the much larger 37 m case, the performance of the MVM and pCuReD algorithms is closely matched.

As the 3-sided WFS only splits the incoming light into three pupil images (instead of four or more), the sensor should perform better in a low light scenario or when detector readout noise is present. Figure 4.11 compares the pyramid WFS to the 3-sided WFS in the presence of readout noise, at different photon fluxes and shows that in a low signal-to-noise ratio (SNR) scenario (low photon flux and high readout noise), the 3-sided WFS has an advantage over the pyramid WFS.

To get a visual sense of the closed-loop performance, a long exposure PSF with and without AO turned on, using a pyramid WFS is shown in Figure 4.12. A more useful way to visualise the PSF is with a radially averaged cross-section, which allows the PSF contrast to be characterised.

The radially averaged cross-section, after 1000 iterations in closed-loop, when using the roofs, 3-sided and pyramid WFSs, using an MVM reconstructor is plotted in Figure 4.13. The contrast relative to the peak intensity is at a maximum at 150 milliarcseconds, where the roofs and pyramid WFS perform similarly, while the 3-sided WFS performance is worse, with less than half a magnitude difference. After 200 milliarcseconds, the PSF tracks the uncorrected PSF and is a result of the limited spatial frequency control space of the DM.

A comparison of the MVM and pCuReD reconstruction methods for the roofs WFS is shown in Figure 4.14, where the radially averaged cross-section after 1000 iterations

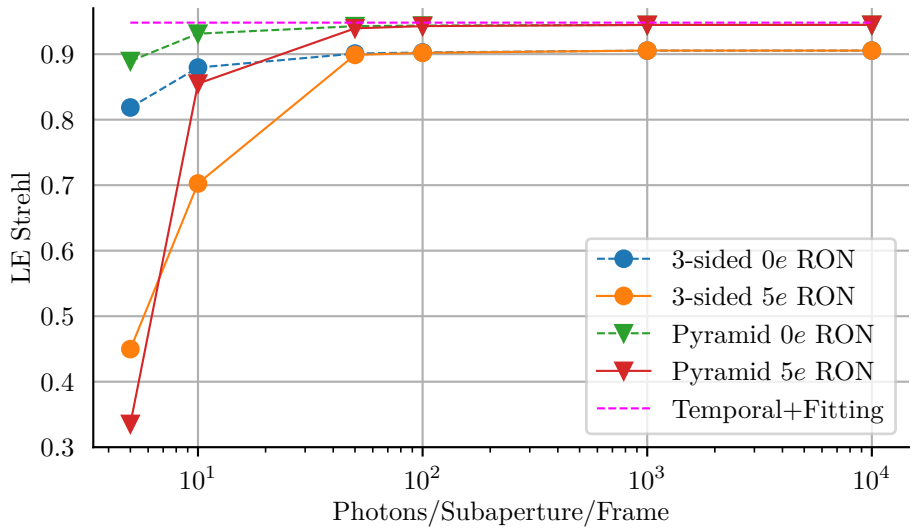

Figure 4.11 The long exposure Strehl in K-band versus the subaperture flux for a read noise of 0 and 5 electrons/pixel/read for the 37 m simulation case, without the spider, using the MVM reconstructor. The dashed line is the K-band Strehl corresponding to the sum of the temporal and fitting errors for this frame rate, controller delay and atmospheric conditions.

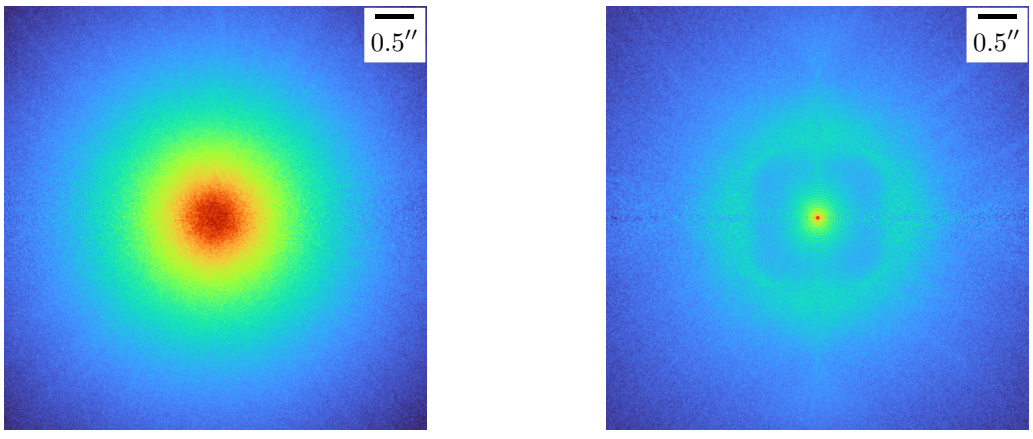

(a) (b)

Figure 4.12 The PSF of an on-axis star for the EELT, simulated with the highest photon flux and zero readout noise. A star blurred by atmospheric distortion (a) is shown for reference. The AO system is operating in closed-loop with a pyramid WFS using an MVM based reconstructor (b).

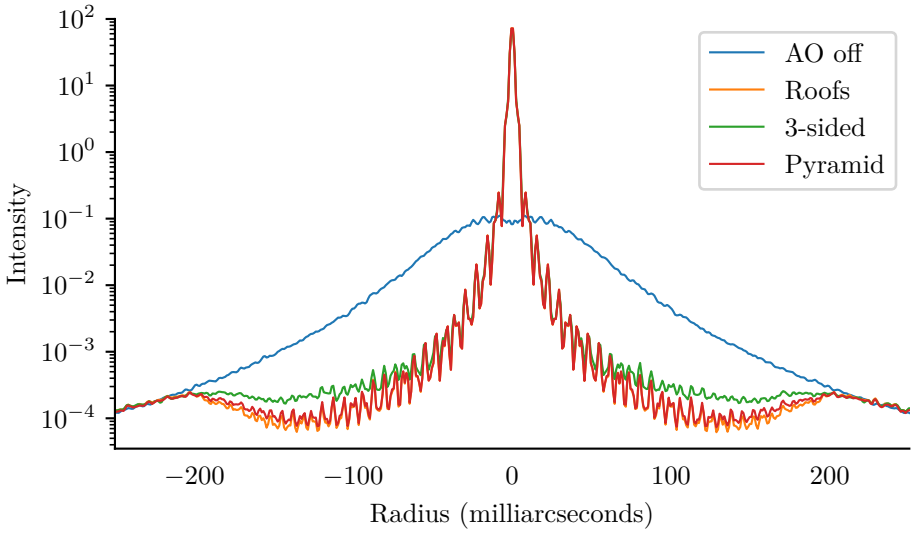

Figure 4.13 The radially averaged cross sections of the PSF images for the 37 m EELT, simulated with the highest photon flux and zero readout noise, using the roofs, 3-sided and pyramid WFS.

in closed-loop is plotted for both reconstruction techniques. The same comparison is done again, but this time for the pyramid WFS and is shown in Figure 4.15. With respect to PSF contrast, the pCuReD and MVM reconstructor have similar performance. The pCuReD reconstructor provides a slight advantage at high angular separation (200 milliarcseconds).

4.2 CONCLUSION

Evaluating the N-sided prism WFS with and without the telescope spider shows that all the sensors perform similarly, with the 3-sided prism WFS performing the worst at high photon flux. With the telescope spider in place, all of the WFSs evaluated see a decrease in closed-loop Strehl compared to the optimum case without the spider, with the roof and 4-sided WFS achieving the highest Strehl ratio. The 6-sided prism WFS performs better than the 3-sided prism WFS, but worse than the roof and 4-sided prism WFSs.

The roofs WFS and pyramid WFS perform almost identically to each other in both the 8 m and 37 m cases in terms of Strehl and PSF profile. In a low SNR scenario, the 3-sided prism WFS achieves a better Strehl than the pyramid WFS. The 3-sided prism WFS is also considerably easier to manufacture than the pyramid WFS and requires fewer optical components than the roofs WFS. It also requires fewer pixels on the CCD, meaning a smaller CCD can be used. The 3-sided WFS could be useful for AO systems where fainter stars are used to guide the AO system. As Fauvarque et al. [Fauvarque et al. 2016, 2017] predicted, in a high flux regime, there is no significant gain in performance by changing the prism geometry, and these end-to-end simulations

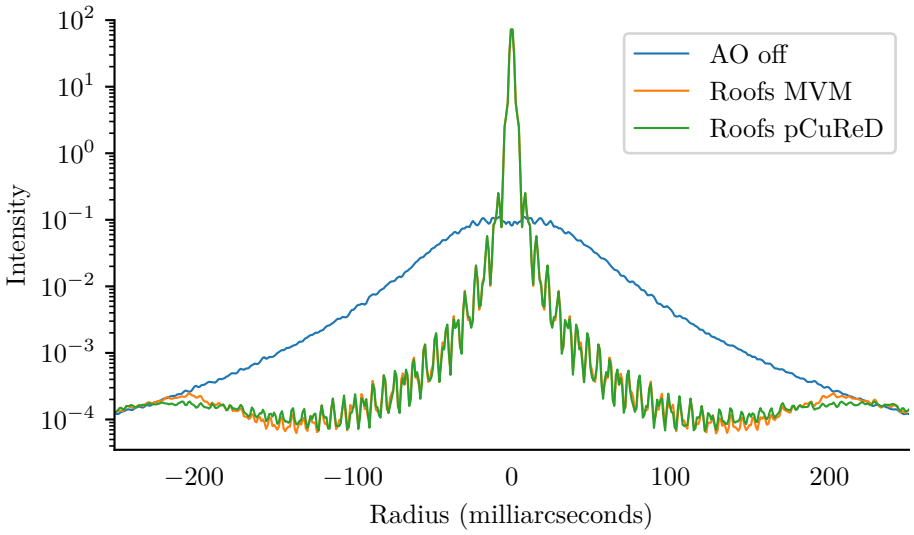

Figure 4.14 The radially averaged cross sections of the PSF images for the 37 m EELT, simulated with the highest photon flux and zero readout noise. The plot compares the pCuReD reconstructor to the traditional MVM reconstructor, using a roofs WFS.

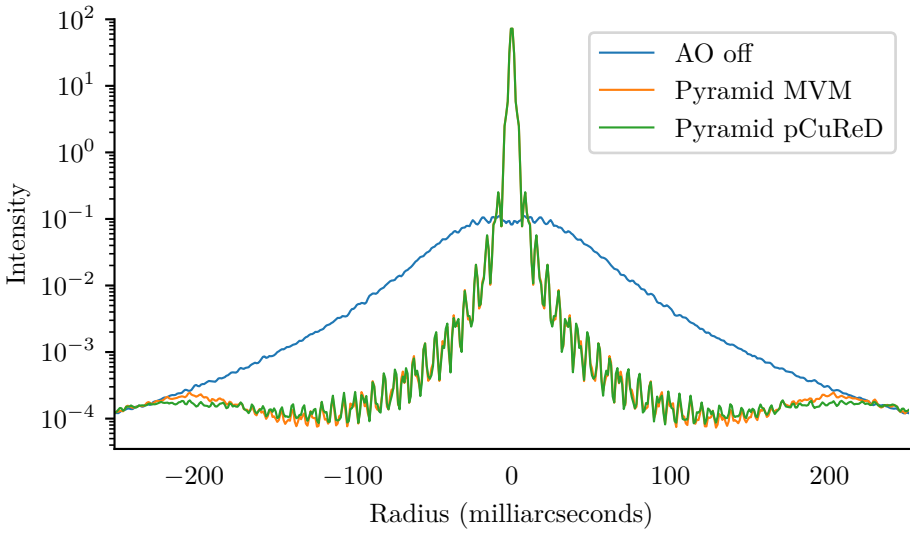

Figure 4.15 The radially averaged cross sections of the PSF images for the 37 m EELT, simulated with the highest photon flux and zero readout noise. The plot compares the pCuReD reconstructor to the traditional MVM reconstructor, using a pyramid WFS.

match that prediction. The pCuReD reconstructor's performance is shown to match that of traditional MVM reconstructors for the roofs WFS and pyramid WFS, whilst significantly reducing computational load.

Chapter 5

DIGITAL FOURIER BASED WAVEFRONT SENSOR

In Chapter 4, the N-sided prism WFS was introduced, and the performance was evaluated in simulation. This chapter takes the N-sided prism WFS from simulations and into the laboratory. Ideally, a physical prism would be manufactured for each type of WFS. However, this is expensive and time-consuming, especially if the aim is to investigate changes to the prism geometry. To overcome the complexities of manufacturing glass prisms, the digital pyramid WFS is used.

In simulation, the prism is represented as a map of optical phase delay, ϕ_{prism}. A spatial light modulator (SLM), which is similar to a liquid crystal display, allows a programmable phase delay at each pixel. This allows for a wide range of prism geometries to be generated, and the prism geometries can be changed on-the-fly. This was first used by Akondi [Akondi et al. 2014] to create a digital pyramid wavefront sensor.

In this thesis, the digital Fourier-based WFS is evaluated, with 3-sided, 4-sided, 6-sided and cone geometries. The phase delay required to produce a useful prism is much larger than the maximum programmable phase delay on each pixel. To overcome the phase limitation, the prism phase map must be wrapped at 2π. The phase wrapping introduces diffraction artefacts, which if not accounted for, can interfere with the pupil images created by the prism WFS. In the configuration used in this chapter, polarising filters are used to minimise the first-order diffraction effects.

Different geometry prisms are interesting, as reducing the number of sides eases manufacturability of the glass prism and for the 3-sided prism, the light is spread over less area, resulting in a higher signal-to-noise (SNR) ratio. There is also evidence to suggest that it could be advantageous to match the prism geometry to the pupil geometry (spider) [Engler et al. 2018]. More information about the incoming wavefront can be measured by increasing the number of prism sides but at a reduced SNR. Using a digital prism WFS, these trade-offs can be evaluated in a real system.

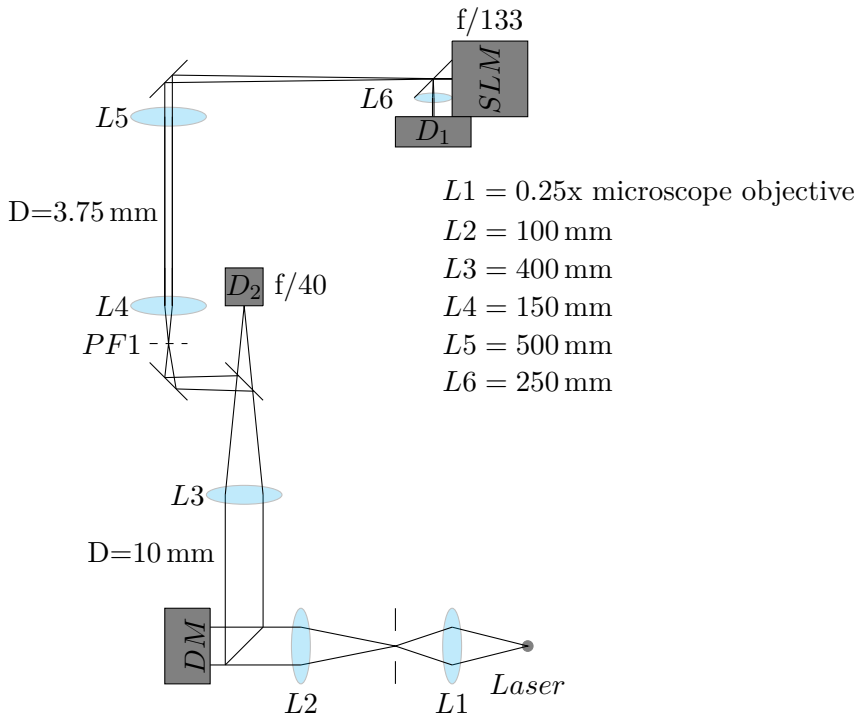

Figure 5.1 The schematic of the optical configuration on the optics bench. The diagonal elements are either beamsplitters or mirrors. All lens elements are Thorlabs 25 mm planoconvex lenses.

5.1 LABORATORY CONFIGURATION

A schematic of the configuration is shown in Figure 5.1 and a photo of the configuration on the optics bench is shown in Figure 5.2. The laboratory configuration consists of a spatial light modulator, a deformable mirror, a 633 nm semiconductor laser, two FLIR grasshopper cameras, and 25 mm planoconvex lenses, mirrors and 50:50 beamsplitters. The pupil of the DM is the pupil mask for the entire configuration. Care is taken to ensure that all pupil planes are optically conjugated to the DM.

5.1.1 Spatial light modulator

The SLM used in this chapter is the Holoeye PLUTO 2 VIS 016, which has a pixel resolution of 1920x1080 with a pixel pitch of 8 µm. The Holoeye PLUTO 2 is a phase-only reflective liquid crystal on silicon SLM offering a maximum of 6π phase shift per pixel. The SLM is configured such that the maximum phase shift per pixel is 2π, and all of the prism phase screens used are modulo 2π. Spatial light modulators are polarisation sensitive. The polarisation filter, PF1, is tuned for the best WFS image quality (high contrast in the pupil images and reduced 0^{th} order reflections). Due to the discretised nature of the SLM, the reflection off of the SLM contains several refractive orders. The 0^{th} order contains light that purely reflects off the SLM surface as well as light which is of the incorrect polarisation. The first order reflection is the desired reflection. Higher

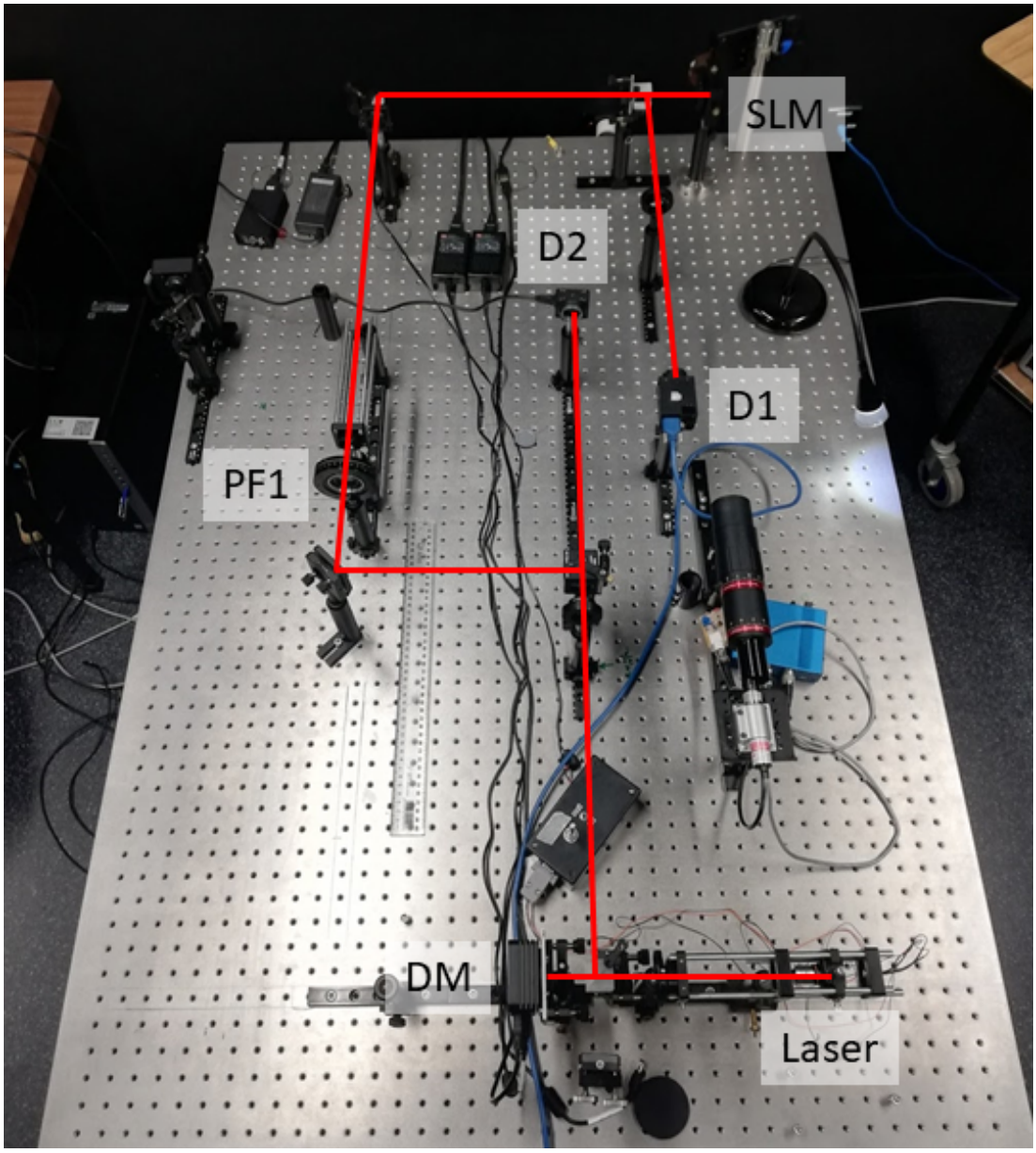

Figure 5.2 The optical configuration on the optics bench, showing the position of the key optical components and the light path through the system.

Table 5.1 Thorlabs DMP40 DM Zernike modes.

Mode number	type
0	astigmatism, 45°
1	defocus
2	astigmatism, 0°
3	Y-trefoil
4	X-coma
5	Y-coma
6	X-trefoil
7	Y-tetrafoil
8	2nd order Y-astigmatism
9	3rd order spherical
10	2nd order X-astigmatism, 45°
11	X-tetrafoil, 45°

order reflections are present, however the detector is not large enough to capture all of them. Tuning PF1, reduces the brightness of the 0^{th} order and increases the contrast of the pupil images.

5.1.2 Deformable mirror

In the optical configuration used in these experiments, a DM is used to introduce wavefront aberrations. The DM used is a Thorlabs DMP40, which uses piezoelectric bimorph technology. The DM has 40 actuators and a 3-actuator tip/tilt system and a 10 mm pupil diameter. The DM has a built-in Zernike modal basis, with a normalized amplitude for each mode. Appendix A shows how a KL modal basis was formed for this DM. The Thorlabs DMP40 Zernike modal basis is outlined in Table 5.1.

5.1.3 Detectors

The experimental configuraion makes use of two FLIR Grasshopper3 cameras, with a resolution of 1920x1200 and a pixel size of 5.86 µm. One camera, D_1, is used as the WFS detector, and the other is used as the focal plane camera, D_2.

5.1.4 Fourier mask

Using the same technique developed in Chapter 4, the prism phase screens for the 3-sided, pyramid, 6-sided and cone WFS are generated to match the dimensions of the SLM and are shown in Figure 5.3. An important step, which is not needed in simulation, is to apply a 2π phase wrap to the prism phase screens. As mentioned, the 2π phase wrapping is required due to the limited phase shift that the SLM can introduce.

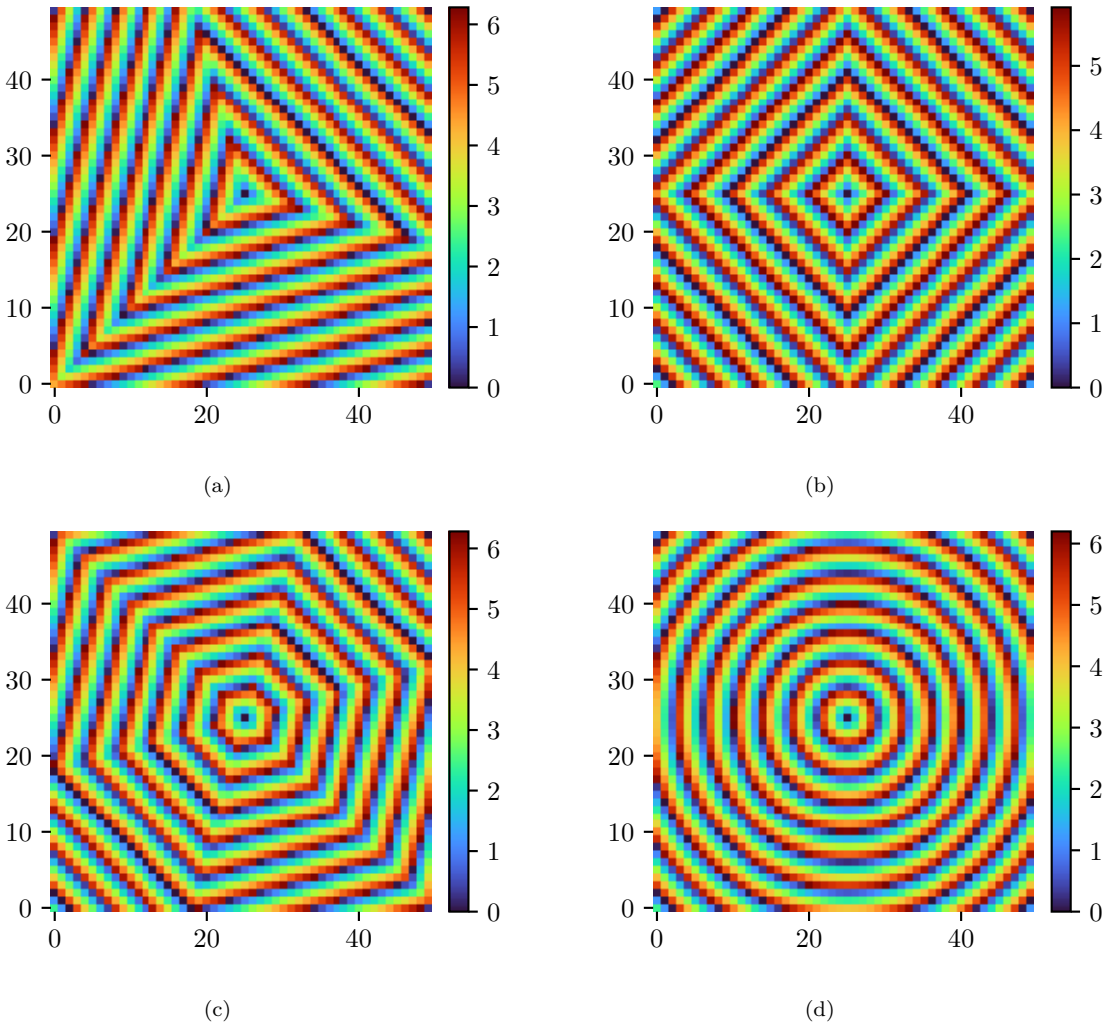

Figure 5.3 A zoomed in view of the phase wrapped prism phase screens, in radians, that are applied to the spatial light modulator for the 3-sided (a), pyramid (b), 6-sided (c) and cone (d) WFS. The original phase screen is 1080x1080 pixels.

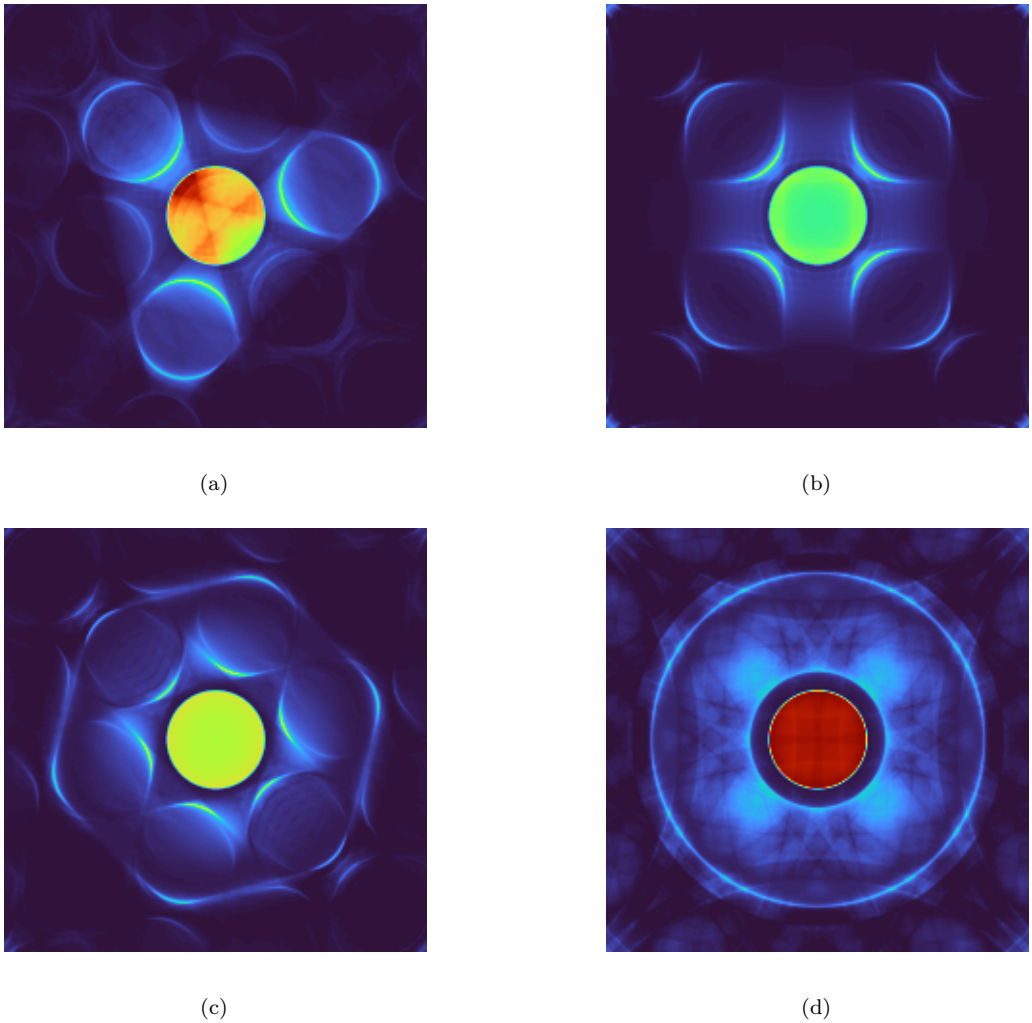

(a) (b)

(c) (d)

Figure 5.4 The simulated detector images for the 3-sided (a), pyramid (b), 6-sided (c) and cone (d) WFS for a flat wavefront. Note the central pupil image which is due to the phase wrapping required by the SLM.

5.2 SIMULATION RESULTS

To better understand any experimental results, it is important to test the system in simulation first. To that end, the unmodulated digital Fourier WFS is simulated for the cases of the 3-sided, pyramid, 6-sided and cone prisms. The simulated WFS detector images for the 3-sided, pyramid, 6-sided and cone WFSs are shown in Figure 5.4.

From Chapter 3, a simple least squares reconstructor, $\mathbf{B}$, can be formed from an interaction matrix, F. To form an interaction matrix, each of the Thorlabs DMP40 Zernike modes are applied (with a small amplitude so as not to saturate the WFS) individually, and the WFS detector image, I, is recorded. The interaction matrix F is

defined as

$$F = \begin{bmatrix} \mathbf{I_1} \\ \vdots \\ \mathbf{I_N} \end{bmatrix}, \tag{5.1}$$

where $\mathbf{I_N}$ a vector containing the N^{th} detector image corresponding to the N^{th} mode in the modal basis. The reconstructor is defined as

$$B = (F^T F)^\dagger F^T. \tag{5.2}$$

The estimated modal weights, $\mathbf{w}$, for the measured wavefront are then

$$\mathbf{w} = \mathbf{B}\mathbf{I}_{\mathbf{meas}}, \tag{5.3}$$

where $\mathbf{I_{meas}}$ is the vectorised image from the WFS detector.

The linearity of 3-sided, pyramid, 6-sided and cone WFSs is evaluated for each of the 12 DM Zernike modes by varying the amplitude of each mode presented to the WFS and calculating the reconstructed amplitude with Equation (5.3). The resulting linearity plots are shown in Figure 5.5 and Figure 5.6. The simulated linearity and detector images of the WFSs form a good baseline of what to expect from the experimental configuration on the optics bench.

5.3 EXPERIMENTAL RESULTS

Using the unmodulated digital Fourier-based WFS, the linearity of each of the Thorlabs DMP40 Zernike modes is measured. An unmodulated WFS is used to limit the number of variables in the experimental system, such as modulation speed and modulation radius. It also removes the need for a tip/tilt modulation mirror, greatly reducing the complexity of the optical configuration and the WFS detector image acquisition.

An example of the WFS detector images is shown in Figure 5.7 for each of the prism geometries, with no wavefront aberration introduced by the DM. The captured image is cropped to the region of interest (a region which contains all of the pupil images) and is vectorised and added as a row in the interaction matrix.

A comparison between the simulated WFS detector image and the measured WFS detector image for the 3-sided, pyramid and cone, with a defocus abberation applied, is shown in Figure 5.8. For each WFS, the measured images match the simulated cases reasonably. There is some residual tilt in the measured images and the measured images have had the central core removed by the polarising filter.

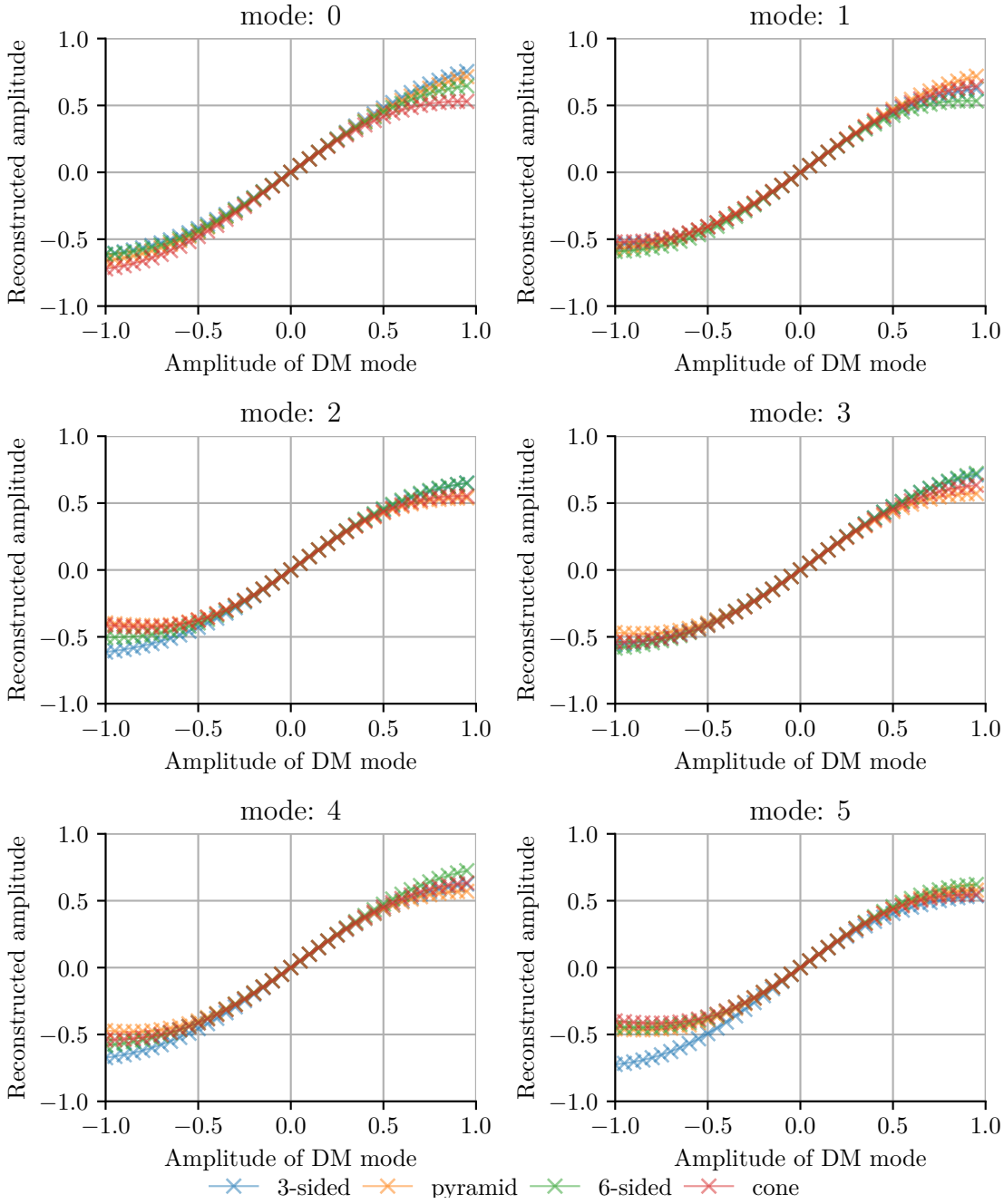

Figure 5.5 The simulated linear range for the 3-sided, pyramid, 6-sided and cone digital Fourier WFS for the first six DM Zernike modes, using the ordering of Table 5.1.

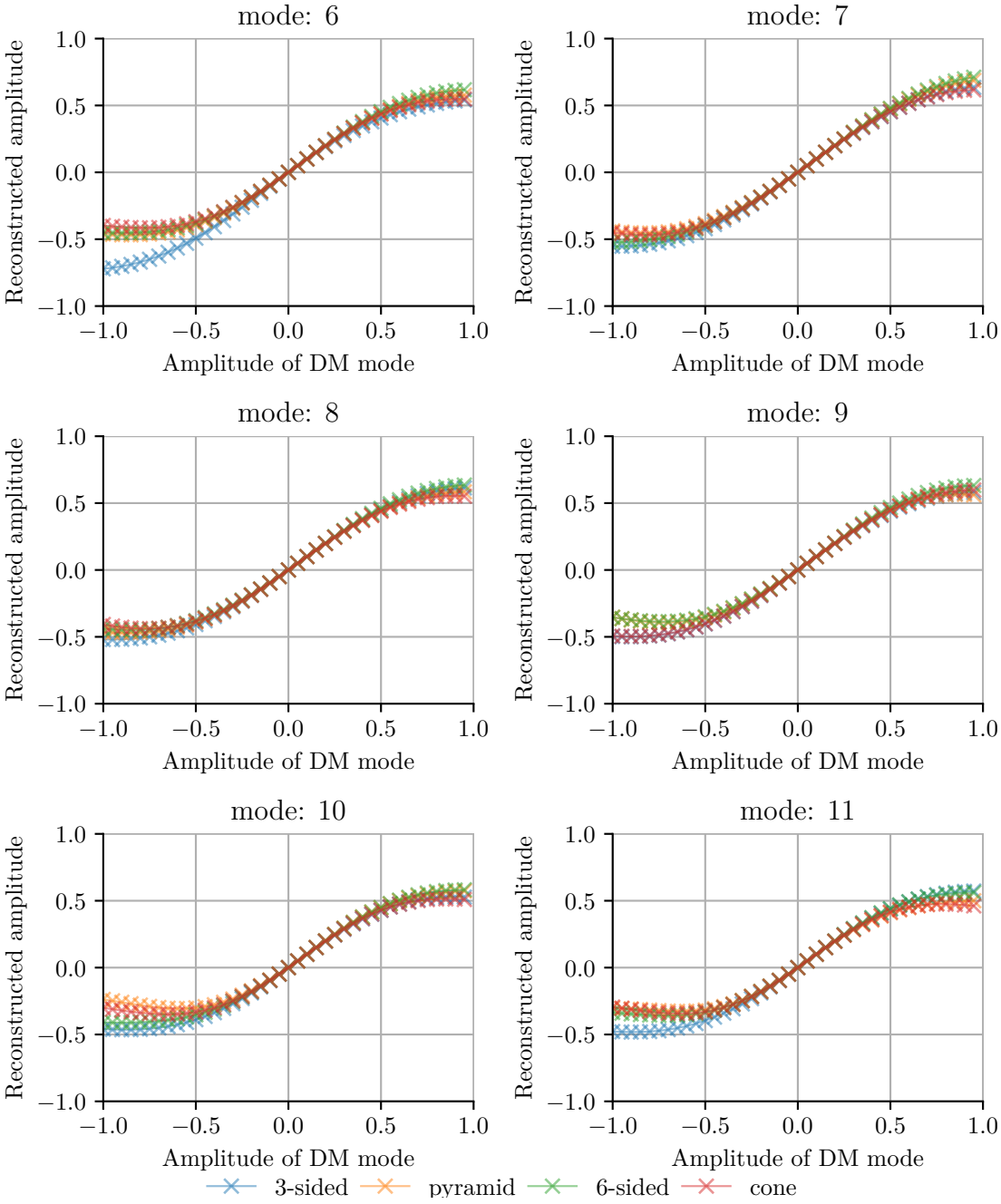

Figure 5.6 The simulated linear range for the 3-sided, pyramid, 6-sided and cone digital Fourier WFS for the last six DM Zernike modes, using the ordering of Table 5.1.

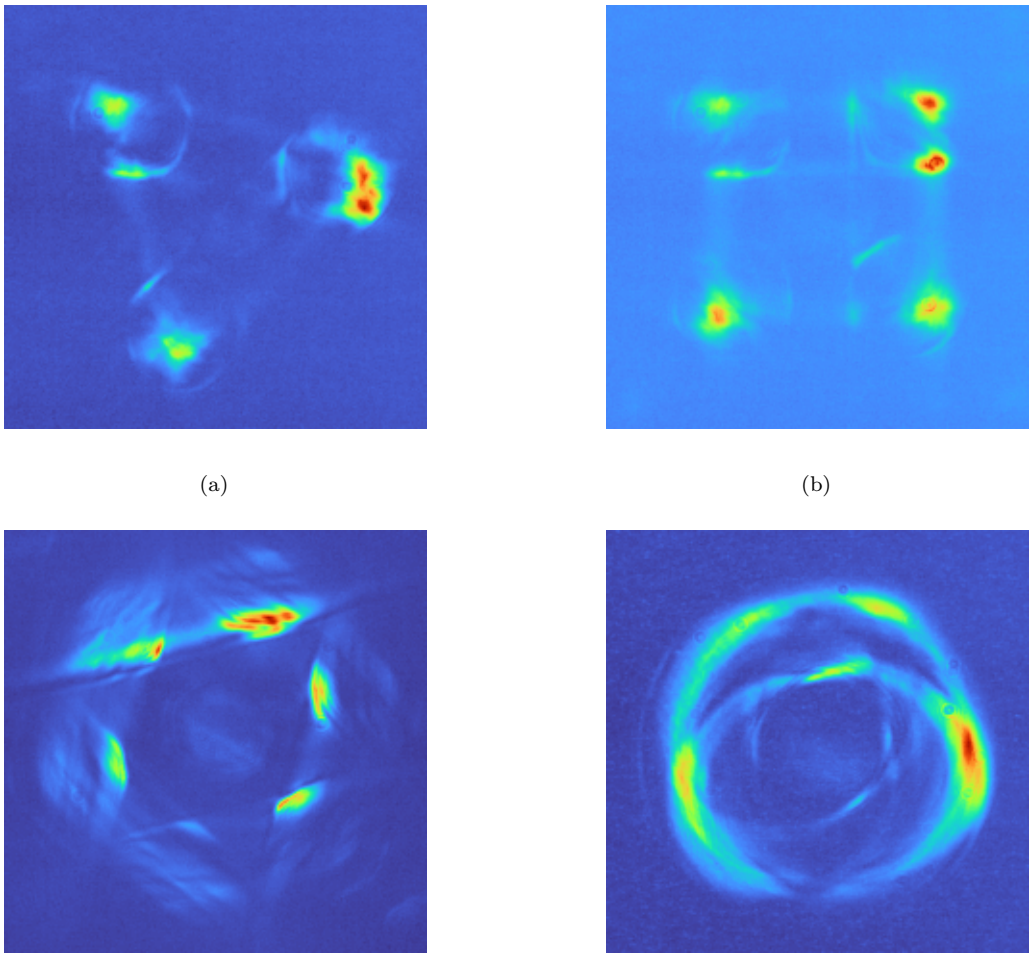

(a) (b)

(c) (d)

Figure 5.7 The detector images for a flat wavefront for the 3-sided (a), pyramid (b), 6-sided (c) and cone (d) WFS.

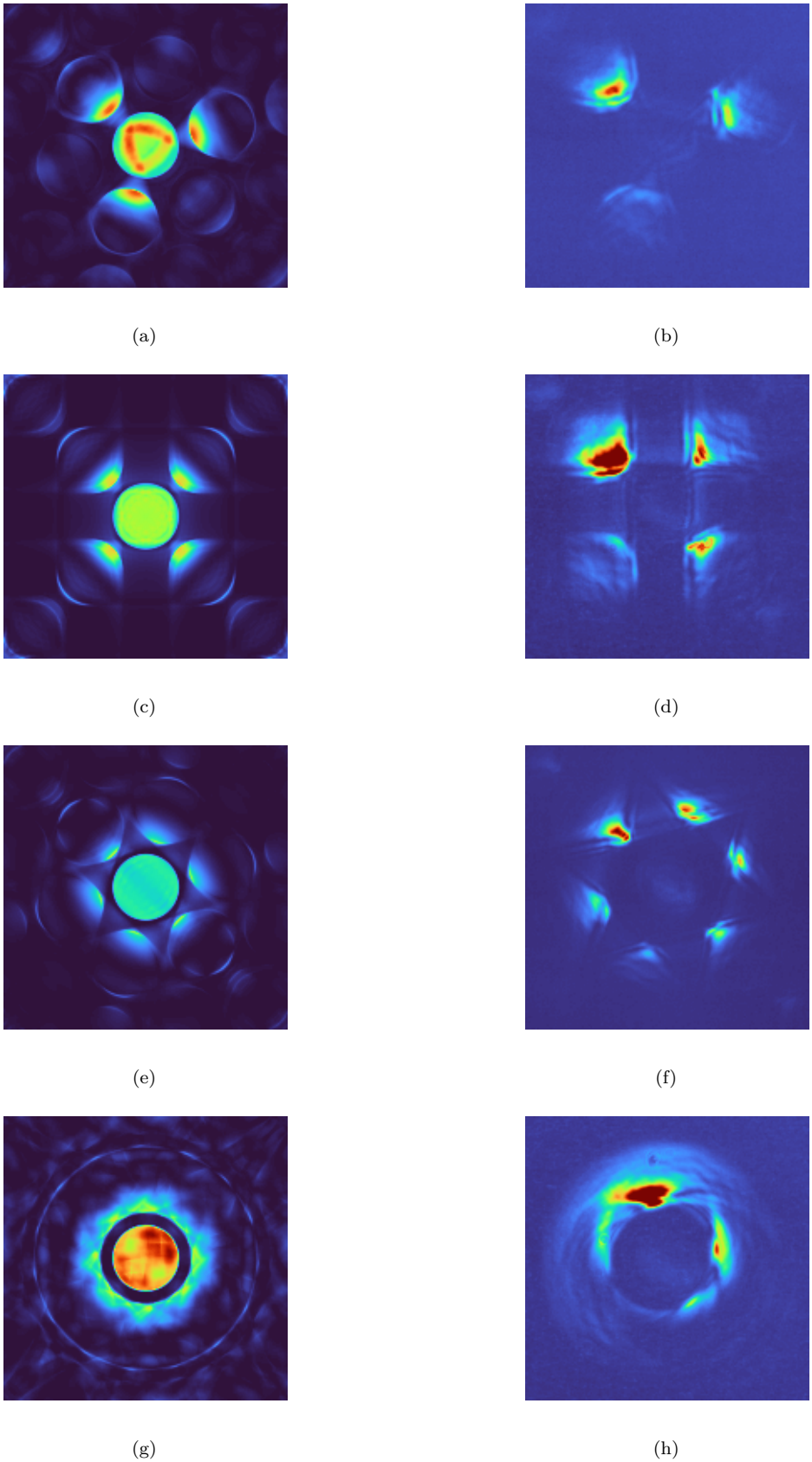

(a) (b)

(c) (d)

(e) (f)

(g) (h)

Figure 5.8 A comparison of a simulated WFS detector image (left column) and a measured WFS detector image (right column) for the digital prism WFS with a defocus abberation applied. The 3-sided prism WFS (a-b), the pyramid WFS (c-d), the 6-sided WFS (e-f) and the cone WFS (g-h)

5.3.1 Wavefront sensor linearity

The linearity of each of the prism geometries is measured for each of the Thorlabs DMP40 Zernike modes. The resulting linearity curves are shown in Figures 5.9 and 5.10, where a small linear region for each mode is observed. From the linearity results, the sensors saturate when a mode amplitude of greater than 0.2 is applied, the higher order modes show a very clear linear range and have a larger amplitude than the lower order modes. This is likely due to the optical gain effect [Deo et al. 2018, Korkiakoski et al. 2008] and a result of the vibrations causing a random modulation of the focal spot.

5.3.2 Limitations of the laboratory

The DM used had limitations in the control of the mirror shape where certain modes contained large tip/tilt components which saturated the unmodulated digital pyramid WFS and required the focal spot to be re-centred on the SLM for every amplitude of the mode. This impacted the dynamic range measurements, and the issue was not overcome, even with the KL modal basis.

It was found that the optics bench is not suitably isolated from the environment, where large vibrations were present on the optics bench, from build infrastructure to heavy construction from the neighbouring buildings. The vibrations resulted in random modulations of the digital Fourier WFS and significantly reduced the quality of the wavefront measurements. Using the focal plane camera, a time series of the PSF was recorded at approximately 1200 frames per second. The centroid of the PSF was calculated for each image from the time series using the centroid equations from Chapter 3 (Section 3.5.1). The power spectrum of the PSF centroid in the x and y directions is shown in Figure 5.11, which shows strong peaks around 30 Hz and 100 Hz. There is also a band of high-frequency vibration spread around 450 Hz. The power spectral density (PSD) is calculated as

$$PSD_x = |\mathcal{F}(\mathbf{x})|^2, \tag{5.4}$$

where $\mathbf{x}$ is a vector containing the time-series of the centroid in the x-axis.

The focal plane camera is at a significantly lower focal ratio than the SLM used for the WFS, meaning the effects of the vibrations are significantly smaller at the focal plane camera than at the SLM.

5.4 CONCLUSIONS

This chapter has presented a digital Fourier-based WFS with a laboratory implementation of the 3-sided, pyramid, 6-sided and cone WFSs. This is the first time digital 3-sided and cone WFSs have been demonstrated. The linearity of the digital 3-sided,

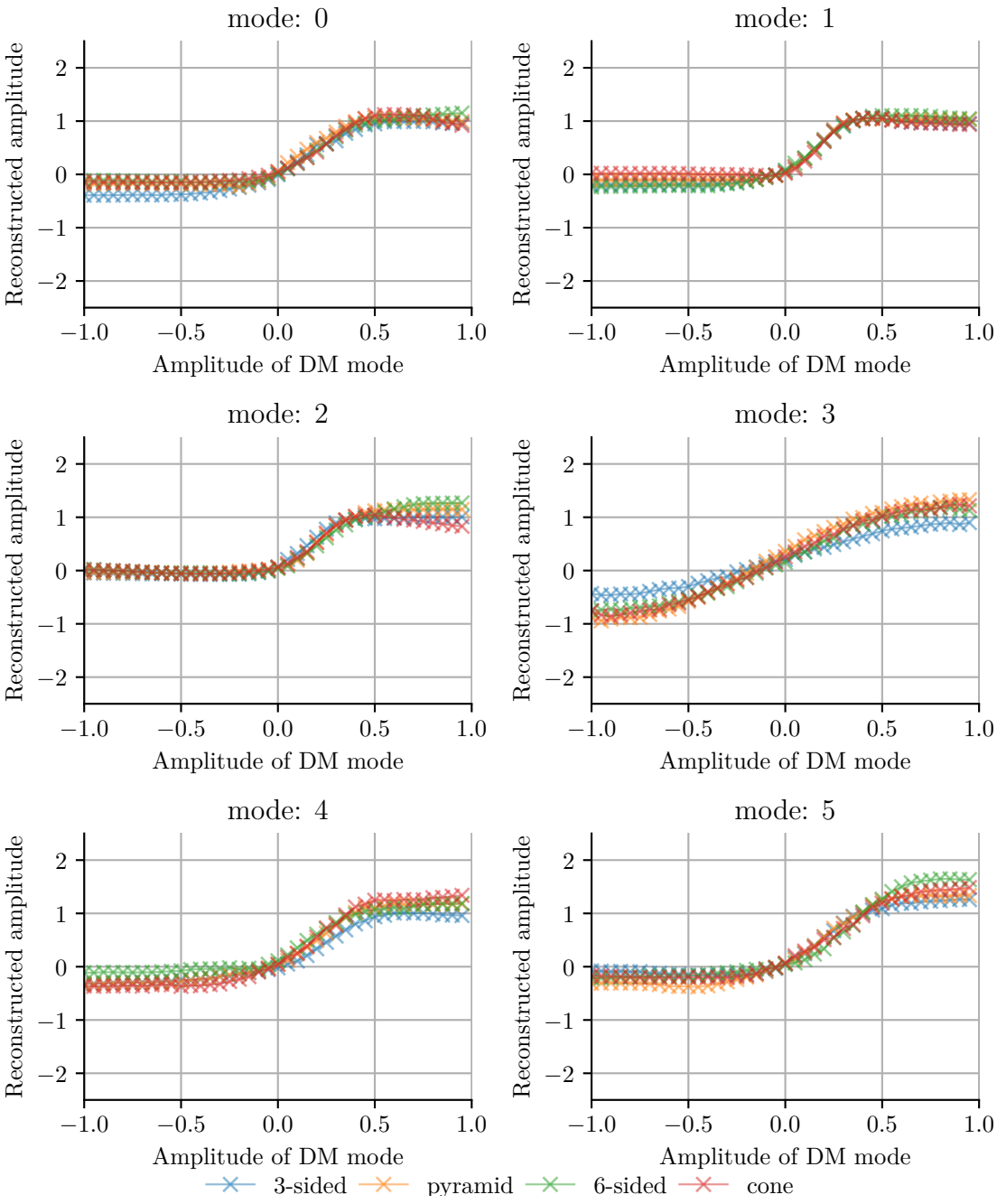

Figure 5.9 The measured linear range for the 3-sided, pyramid, 6-sided and cone digital Fourier WFS for the first six DM Zernike modes, using the ordering of Table 5.1.

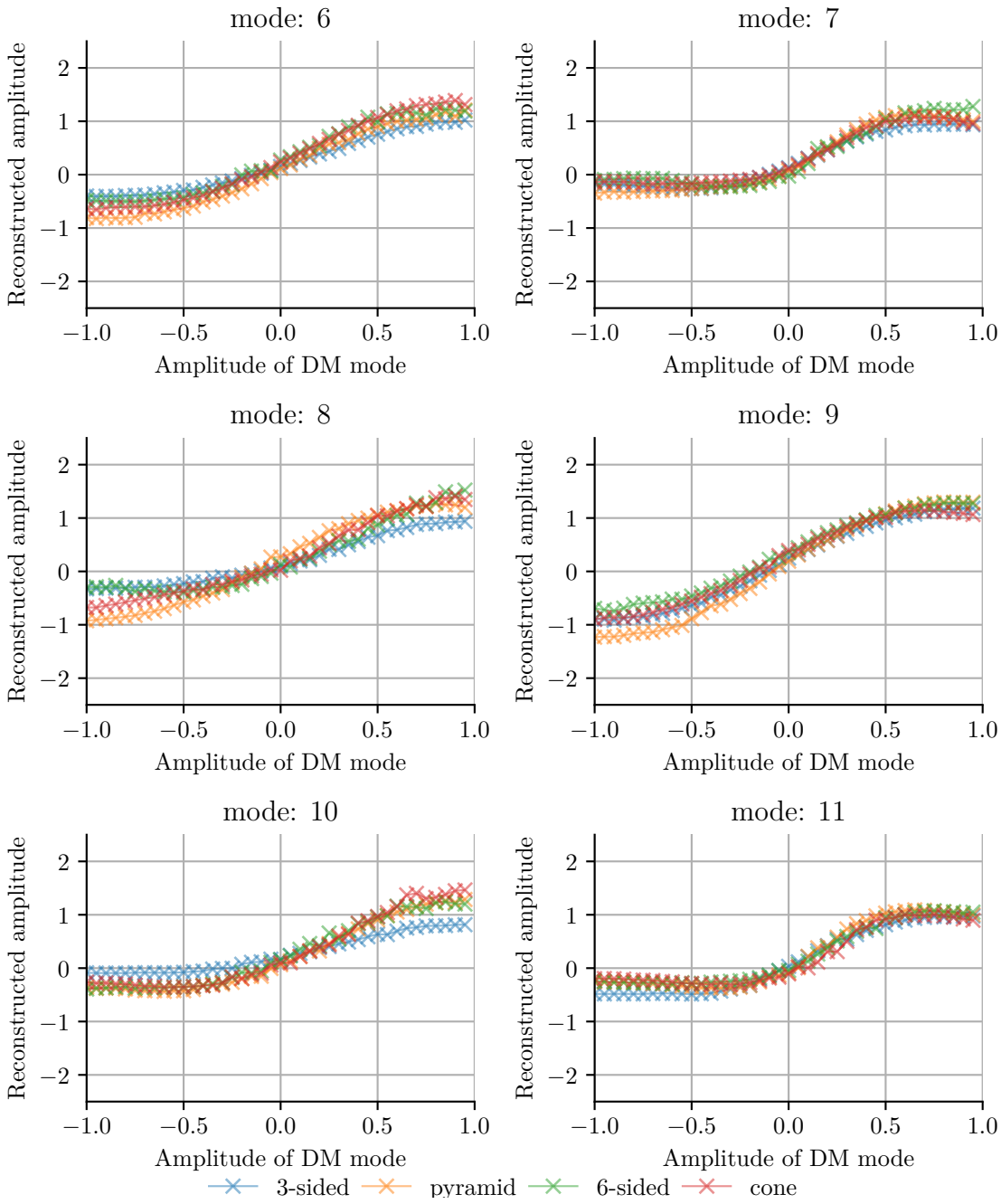

Figure 5.10 The measured linear range for the 3-sided, pyramid, 6-sided and cone digital Fourier WFS for the last six DM Zernike modes, using the ordering of Table 5.1.

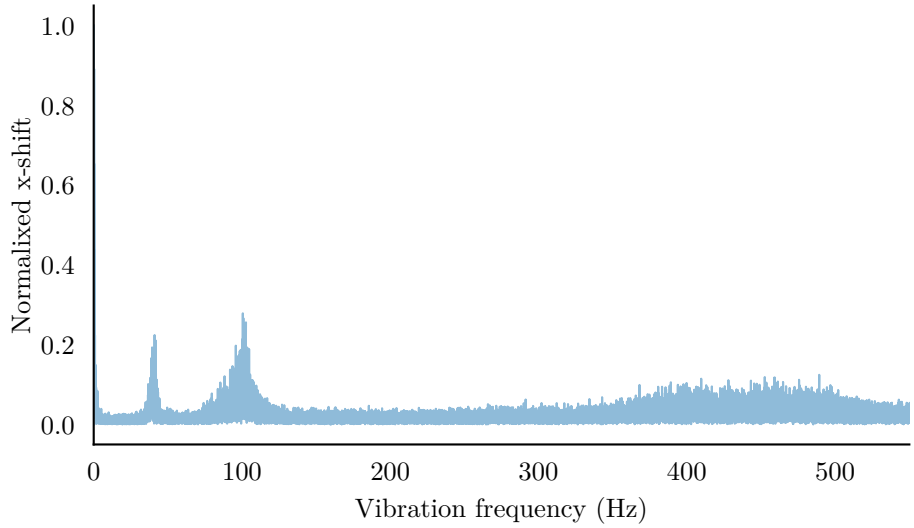

(a) X-axis vibration spectrum

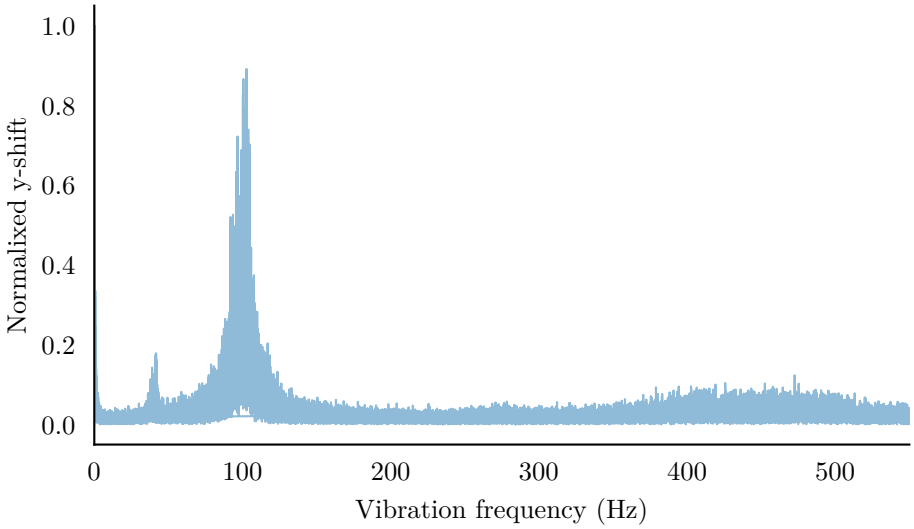

(b) Y-axis vibration spectrum

Figure 5.11 The power spectrum of vibrations on the optics bench in the x (a) and y (b) axis.

pyramid, 6-sided and cone WFSs has been measured in an open-loop configuration and showed little difference between the different geometry prisms, which matches predictions made by Fauvarque et al. [Fauvarque et al. 2016, 2017].

Due to the vibration environment in the optics laboratory and the limitations of the DM, the quality of the results was limited. However, the system shows that the concept of a digital Fourier-based WFS is useful for prototyping prism-based WFS geometries.

The digital pyramid WFS presented here opens the possibility to explore Fourier-based WFSs beyond simple prisms, where the Fourier filter is optimised for a particular application.

Chapter 6

THE PROBLEM OF SEGMENT PISTON DUE TO LARGE SPIDERS

Due to the ELTs' physical size, the support structure (or spider) which holds the secondary mirror in place is also large. In the case of the EELT, the spider has six support beams with a thickness of 0.5 m [Schwartz et al. 2017]. These spider arms have the effect of dividing the pupil into six segments (or petals), which is shown in Figure 6.1. The width of the spider arms is greater than the typical coherence length of the atmosphere, or Fried parameter r_0, expected at the observatory sites. This introduces complexities in the wavefront estimation, as there is no phase continuity between the six pupil segments. Consequently, the average wavefront over each pupil segment (segment piston) is different, and for a modulated pyramid WFS the sensitivity to these segment piston modes is poor.

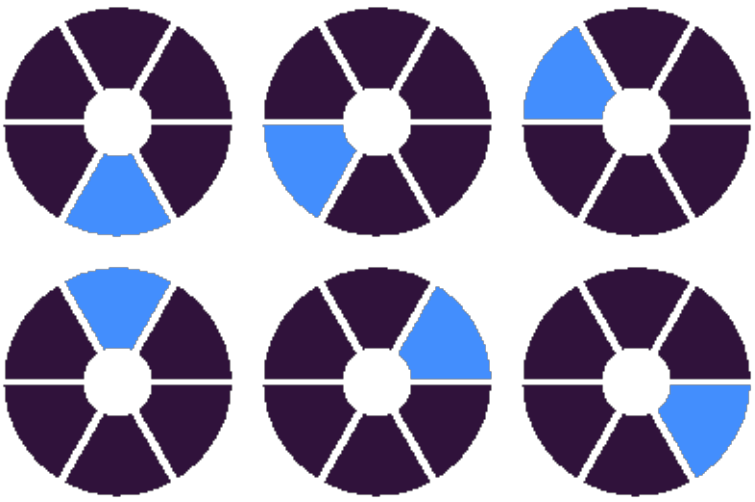

Figure 6.1 The six segment piston modes of the EELT.

The main contributing factors to the segment piston problem are: the so-called low wind effect, segment piston due to atmospheric turbulence, and segment piston due to modal aliasing of the modal basis functions used for wavefront control.

The low wind effect is a phenomenon where the low-velocity wind blowing over the telescope structure is cooled to sub-ambient temperatures, resulting in optical path differences across the pupil of the telescope [Holzlöhner et al. 2020].

This chapter outlines the effects of large telescope spiders on the wavefront measurement and reconstruction, as well as the detrimental effects of segment piston errors.

6.1 TEMPORAL ANALYSIS OF SEGMENT PISTON MODES

Atmospheric segment piston modes are those which naturally occur in the atmosphere. Using the Octopus simulation tool [Le Louarn et al. 2004], a closed-loop AO system is simulated, with no special considerations for segment piston control. Using a pyramid WFS to sense the atmospheric distortion, and a DM to correct for it, the residual segment piston errors are measured at each iteration by projecting each segment piston mode onto the residual phase screen,

$$O_{sp} = \phi_{\text{res}} \cdot \phi_{\text{sp}}, \tag{6.1}$$

where ϕ_{sp} is the mask for a single pupil segment, and

$$\phi_{\text{res}} = \phi_{\text{atm}} - \phi_{\text{DM}}. \tag{6.2}$$

In closed-loop, the average residual phase over each segment should be zero. The PSD of the change in segment piston error over time is given by

$$O_{\text{PSD}} = \frac{1}{F_s N} |\mathcal{F}(\mathbf{O}_{\text{sp}})|^2, \tag{6.3}$$

where F_s is the sample rate (the rate at which the WFS captures images), N is the number of samples, and $\mathbf{O}$ is a vector containing the sampled segment piston error for a single segment.

The cumulative PSD, O_{cumsum}, is the cumulative sum of the PSD over the Nyquist frequency range and is expressed as

$$O_{\text{cumsum}}[i] = \sum_{j=0}^{i} O_{\text{PSD}}[j]. \tag{6.4}$$

Figure 6.2 shows the segment piston errors evolving over time, if not corrected, and the corresponding cumulative PSD, which shows that 95% of the temporal evolution of the segment piston modes occurs at a rate of less than 100 Hz. The temporal evolution of the segment piston modes is relatively slow compared to that of other atmospheric modes suchs as tip, tilt and defocus.

Along with the segment piston errors due to atmospheric turbulence described

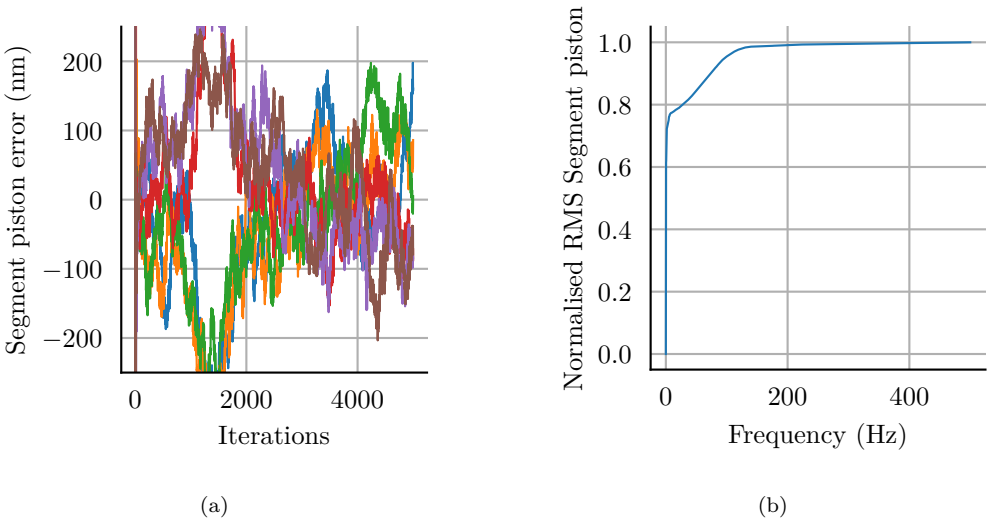

Figure 6.2 The residual segment piston error with an atmosphere with r_0 of 15 cm, using a modulated pyramid wavefront sensor and making no special effort to correct the segment piston errors (a). The different colours represent the six different segments. The corresponding normalised cumulative power spectral density (b).

previously, the WFS and wavefront estimation form a significant contribution to the segment piston error. Between the pyramid WFS and the wavefront estimation, it is possible for the segment piston modes to become aliased into higher-order modes in the control basis. This aliasing results in a situation where the wavefront controller inadvertently introduces segment piston errors.

If care is not taken to compensate for segment piston errors, a decrease in Strehl of over 50% is possible in some scenarios. Figure 6.3 shows the simulated residual optical path difference, using the Octopus simulation tool, over the 37 m EELT pupil in K-band without segment piston mode corrections. The resulting closed-loop Strehl is approximately 42%, compared to 96% without the spider and associated segment piston errors.

6.2 PREVIOUSE ATTEMPTS TO SOLVE THE SEGMENT PISTON PROBLEM

Previous work on the topic of segment piston control has led to several approaches to solving the problem. Schwartz et al. [Schwartz et al. 2017] have shown a phase closure algorithm to ensure a continuous phase across pupil segments. Their algorithm uses the amplitude of actuators along adjacent pupil segment edges to estimate the correction phase required to ensure continuous phase across pupil segments. They also suggest that the pupil segment piston modes can be filtered from the modal basis. However, the AO system would then be unable to correct the atmospheric segment piston modes. Finally, they show that by slaving adjacent actuators across pupil segments, the DM behaves as if the surface were continuous, therefore eliminating segment piston errors.

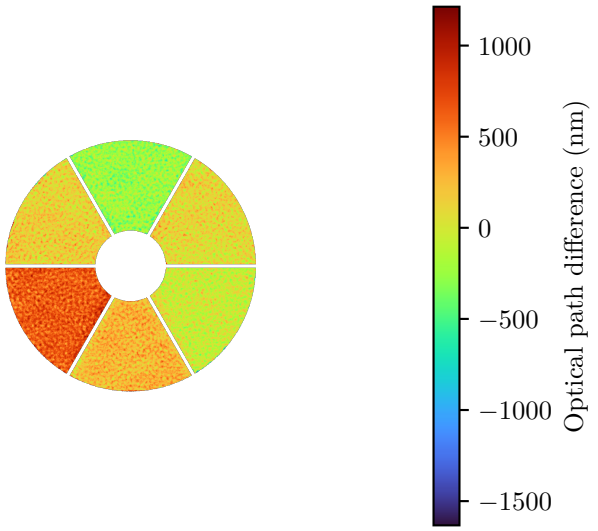

Figure 6.3 The residual optical path difference with an atmosphere with r_0 of 15 cm, using a modulated pyramid wavefront sensor and making no special effort to correct the segment piston errors.

Hutterer et al. [Hutterer et al. 2018] proposed a method using a pyramid WFS with a split controller approach, where two reconstructors are used. In their split approach, one reconstructor uses a segment piston-free modal basis and corrects for the main part of the atmospheric turbulence. A second reconstructor is used only to reconstruct the segment piston modes. The resulting command for the DM is the combination of both reconstructors. They show this method working with a modulated pyramid WFS operating in K-band only.

6.3 SIMULATION PROCEDURE

Numerically evaluating a full 37 m telescope is computationally demanding, especially when searching the parameter space for optimal settings. For this reason, a scaled down test case is used in this chapter, with an 8 m diameter pupil. The spider arm width is selected such that it equals the width of the WFS subapertures. This equates to a spider arm width of 20 cm. Having the spider obstruct entire subapertures creates the segment discontinuities which are of interest in this thesis. Importantly, the spider arm width is also larger than the typical r_0 at the observatory site. The salient parameters for the simulations are presented in Table 6.1.

In the wavefront reconstruction, subapertures are only used if the amount of light received is above the chosen illumination threshold. Consequently, depending on the angle of the spider arms relative to the detector, there are a different number of active subapertures and also a different number of non-contiguous islands. For example, as shown in Figure 6.4, if the spider is rotated slightly (for example, 5°), such that the arm is no longer paraxial, the active subaperture detection algorithm detects the obstruction

Table 6.1 Simulation parameters used in this chapter.

Parameter	Value
Telescope Diameter (D)	8 m
Fried parameter (r_0)	12.9 cm
Outer Scale (L_0)	25 m
Atmosphere	ESO 9 layer model [Clare et al. 2011]
Central Obscuration Diameter	1.2 m
Frame Rate (F_s)	3 kHz
Delay	2 Frames
WFS Wavelength (λ_W)	700 nm
WFS Order	40 × 40 Subapertures
Subaperture Width (d)	20 cm
Prism apex angle	26.4°
PSF Wavelength	2.2 µm
Modulation Width	4 λ_W/D
Time Steps	1000
Number of Spider Arms	6
Spider Arm Width	20 cm
Read noise	0 electrons/pixel/frame
Number of Modes	1346
Number of Actuators	1346

and deactivates the obstructed subapertures. The variation in active subaperture selection with the spider orientation presents a problem when comparing results from the spider at different orientations, whereby the number of active subapertures can vary with the angle of the spider and has an effect on the closed-loop Strehl.

6.4 OPTIMISATION OF THE PYRAMID WFS WITH A SPIDER

Using the simulation parameters from Chapter 4, for the case of an 8 m telescope with no spider, the closed-loop Strehl in K-band is 96%, and there is no segment piston errors, as shown in Figure 6.5(a) Using the optimised parameters for an 8 m telescope without a spider, but now including the spider, results in a closed-loop Strehl of 0.8% due to the effects of segment piston errors, as seen in Figure 6.5(b). By lowering the illumination threshold for active subaperture detection from 75% to 50%, increasing the regularisation, and reducing the number of modes corrected from 1346 to 1000, the closed-loop Strehl is improved from 0.8% to 94.7%. The DM can reproduce modes (segment piston) that the WFS senses poorly. By decreasing the number of modes corrected, and increasing the regularisation, this effect is minimised. For the parameters in Table 6.1, the case optimised with the spider is 2% worse than the optimised case without the spider as seen in Figure 6.5(c). Differential segment piston is still present in the optimised case with the spider. The horizontal striations are due to the lateral

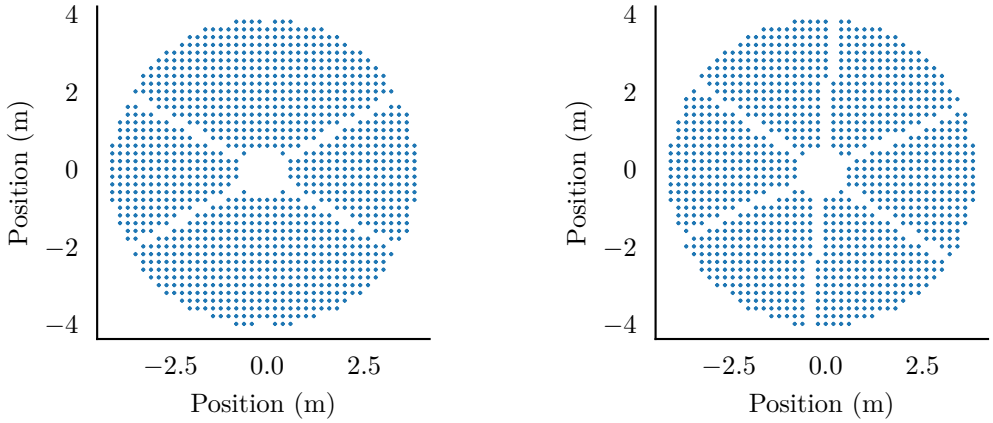

Figure 6.4 When a spider arm is paraxial with the WFS subapertures and with a 50% illumination detection threshold, the subapertures obscured by the paraxial arm are still included (a). When the spider arms are not paraxial and with a 50% illumination detection threshold, the obstructed subapertures are excluded from the reconstruction (b).

movement of the atmospheric phase screens to model wind.

6.4.1 Effect of Illumination Threshold on Closed-loop Strehl

In Section 6.4, the Strehl with a spider is improved by reducing the illumination threshold for active subaperture detection. To identify the optimum threshold for active subaperture detection, the illumination threshold is swept from 20 to 100% in steps of 10% with one of the spider arms paraxial to the WFS detector. For each illumination threshold evaluated, the loop gain, g of Equation (3.46), the number of modes corrected, and the regularisation amount, N_p of Equation (4.9), are optimised for the highest closed-loop Strehl.

Figure 6.6 (a) shows the closed-loop Strehl as a function of the illumination threshold. At illumination thresholds above 50%, subapertures partially obstructed by the paraxial spider arms are ignored in the wavefront estimation, reducing the number of active subapertures used in the wavefront estimation. At illumination thresholds at and below 50%, the subapertures partially obstructed by the paraxial spider arms are included in the wavefront estimation. Consequently the number of non-contiguous islands increases from four to six. This shows that a better wavefront estimate can be achieved when the subapertures partially obstructed by the spider are included in the wavefront estimation. As seen in Figure 6.6 (b), the number of active subapertures increases, as the illumination threshold decreases. However, the large change in Strehl in going from a threshold of 60% to 50%, shows that the improvement is not due to a small change in the number of active subapertures, but rather due to the number of islands reducing from six to four. Care needs to be taken when selecting active subapertures around the telescope

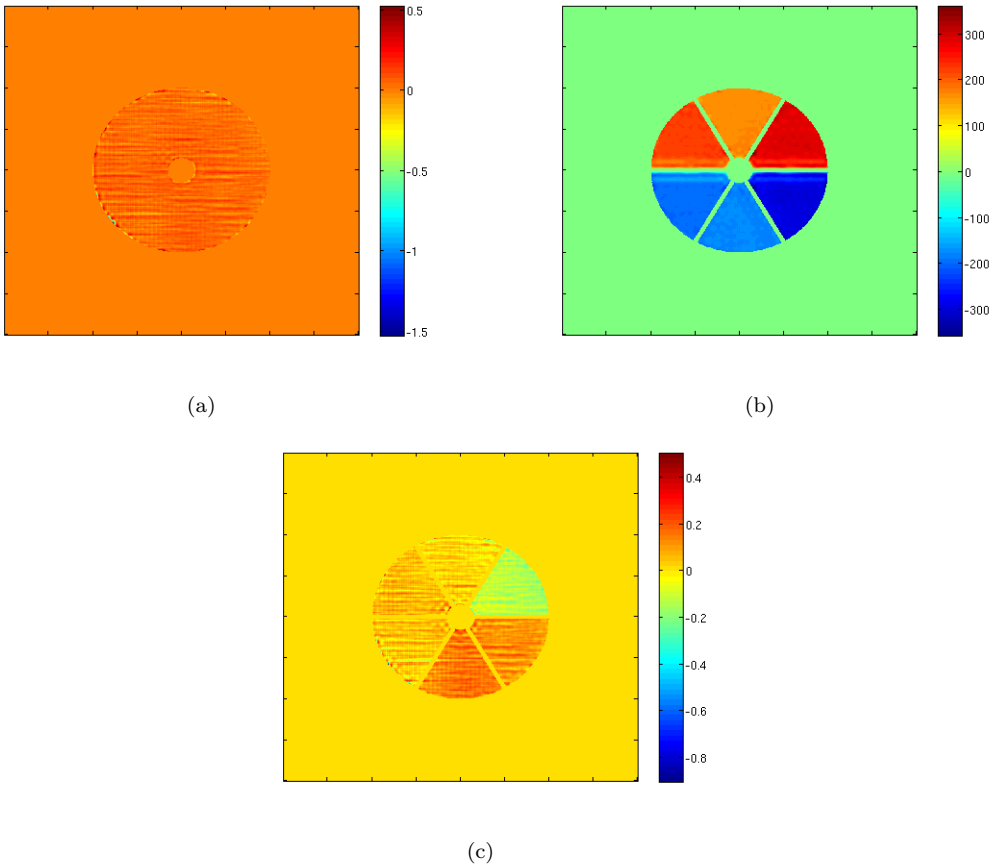

(a) (b)

(c)

Figure 6.5 For the 8 m case, the average residual phase error, in radians, over 500 timesteps, for, optimised without the spider (a), optimised without the spider, now with the spider present (b), and optimised with the spider present (c).

spider arms, as the number of islands of subapertures can change from four (when a spider arm is paraxial to the WFS detector) to six, consequently increasing the segment piston error.

6.4.2 Position of spider arms relative to the pyramid edges

Without a spider, the orientation of the pyramid (prism) to the pupil has no impact. However, when the spider is included, the orientation of the spider arms relative to the edges of the pyramid can have an effect. To test this, an 8 m case where a 20 cm thick 1-arm spider is rotated relative to a fixed prism is simulated.

The spider is rotated in five degree steps. For each rotation angle, the loop gain and regularisation are tuned for maximum closed-loop Strehl. Figure 6.7 shows a 15% variation in closed-loop Strehl between an optimal alignment (0 and 90 degrees) when compared to the worst-case (45 degrees). Physically, an alignment of 0 and 90 degrees corresponds to the spider aligned with the edge of the pyramid, while 45 degrees corresponds to the spider arm in the middle of a pyramid face. The pyramid is an

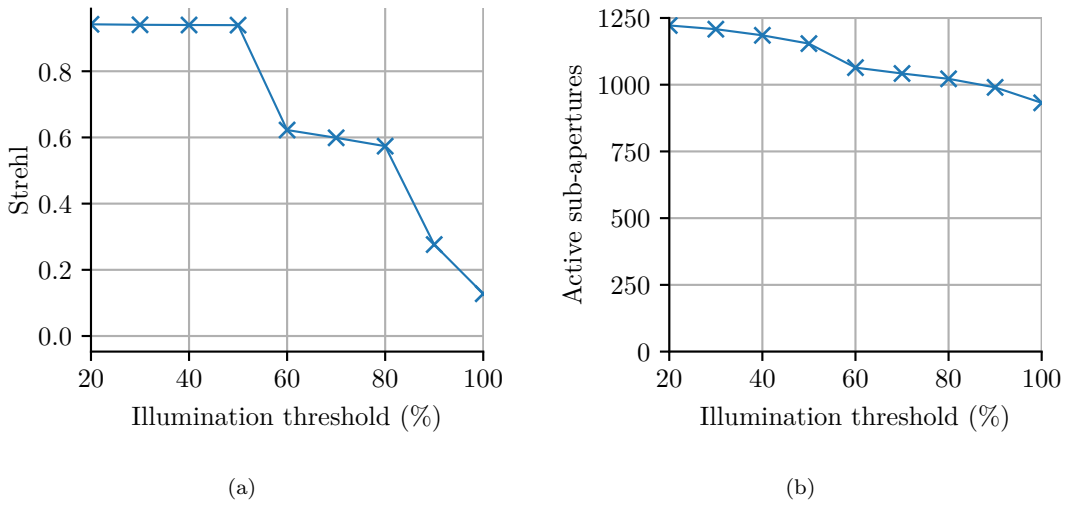

Figure 6.6 The long exposure Strehl in K-band versus the illumination threshold used for detecting active subapertures (a). The number of modes, gain and regularisation are optimised for each point. The number of active subapertures vs the illumination threshold used for detecting active subapertures (b).

extension of the Foucault knife edge test [Wilson 1975], and is most sensitive along the pyramid edges. Having the spider aligned with the pyramid edges is thus most sensitive to segment piston modes. Figure 6.7 also shows the number of active subapertures. While the number of active subapertures decreases by 2%, at 45 degrees relative to zero degrees, this does not account for the associated change in closed-loop Strehl. The variation in Strehl has a sinusoidal variation, whilst the number of subapertures has a more step-like response, suggesting that the Strehl variation is not related to the number of active subapertures but rather the alignment of the spider with the WFS prism.

For wavefront sensors that do not receive a derotated beam (as the Earth rotates the telescope tracks the stars, and for certain types of telescope mounts this causes the imaging field to rotate), the AO system's closed-loop performance will depend on the orientation of the telescope. For instruments that account for field rotation, it will be essential to determine the optimal alignment of the pyramid and spider to obtain the AO system's highest performance.

6.5 SENSITIVITY OF THE PYRAMID WFS TO SEGMENT PISTON

The previous sections have dealt with optimising the wavefront estimation in the presence of the telescope spider. This section investigates the sensitivity of the pyramid WFS to segment piston modes and introduces a sensitivity metric for segment piston modes. The metric used to evaluate the sensitivity of the pyramid WFS to segment piston errors is the eigenvalues of segment piston eigenmodes.

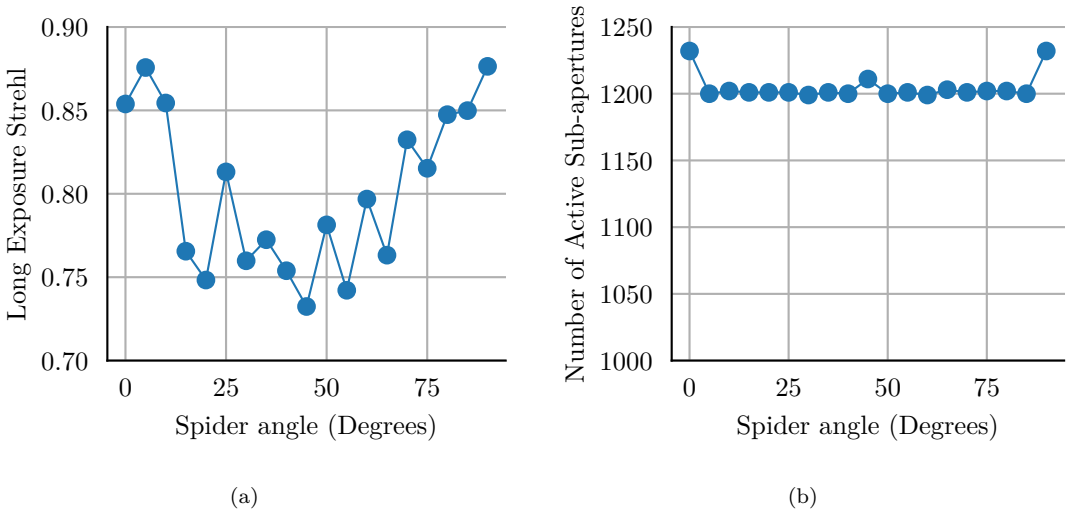

Figure 6.7 A simplified test case with an 8 m diameter mirror and a 1-arm spider. The spider is rotated relative to the pyramid, and at each rotation step a full closed-loop simulation is performed. The closed-loop K-band Strehl versus the spider angle (a). The number of active subapertures used in wavefront estimation (b).

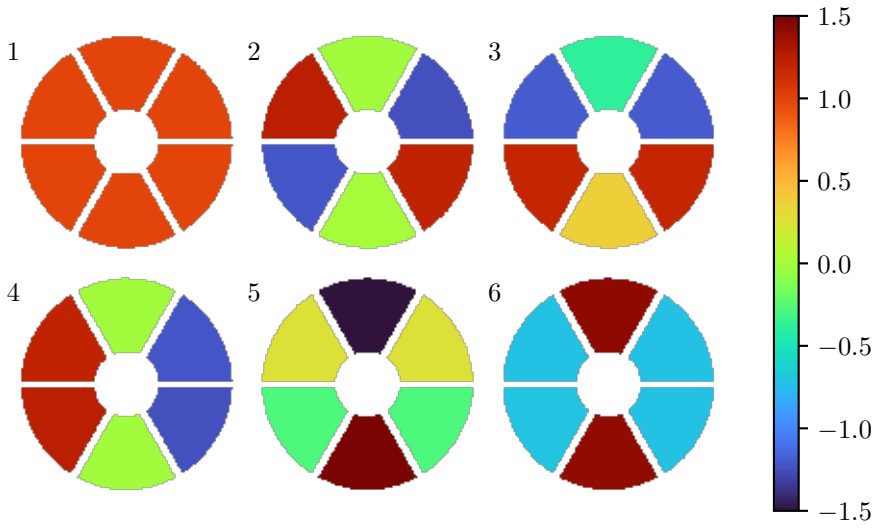

Figure 6.8 The segment piston eigenmodes, including piston, for an unmodulated pyramid WFS. The modes are ordered from least sensitive to most sensitive (top left to bottom right). The amplitude of each mode has been normalised such that the RMS over the pupil is one.

The segment piston eigenmodes, shown in Figure 6.8, are found via a singular value decomposition of an interaction matrix formed by poking the six individual segment piston modes. First, the system response to the segment piston modes is recorded in an interaction matrix, F_{sp}, for a diffraction-limited system. The interaction matrix is generated by applying each segment piston mode to the DM, as shown in Figure 6.1. The resulting wavefront is then propagated to the pyramid WFS, and the wavefront measurement is recorded. Each measurement is a row in the interaction matrix. Then,

using singular value decomposition (SVD), the segment piston interaction matrix, F_{sp}, is decomposed into singular values (or eigenmodes), which are a linear combination of individual segment piston modes,

$$\mathrm{F}_{\mathrm{sp}} = USV, \tag{6.5}$$

where U and V are unitary matrices and S is a diagonal matrix of singular values (eigenvalues). V contains the eigenvectors of F_{sp}, and S contains the corresponding eigenvalues. From this factorisation, the segment piston eigenmode basis is constructed as

$$Z_{\mathrm{eigen}}(i) = \sum_{m=1}^{M} V_{i,m} Z_{\mathrm{sp}}(m), \tag{6.6}$$

where Z_{sp} is the modes-to-command matrix for the segment piston modes as shown in Figure 6.1, Z_{eigen} is the modes-to-command matrix (DM commands for each mode) for the segment piston eigenmodes, i is the eigenmode index, and M is the number of segment piston modes. The resulting segment piston eigenmodes, Z_{eigen}, are shown in Figure 6.8 (unmodulated case) and the corresponding segment piston eigenvalues are shown in Figure 6.9. The higher the eigenvalue, the more sensitive the WFS is to the corresponding eigenmode.

Using the segment piston eigenvalues as a performance metric, the segment piston eigenvalues of a pyramid WFS are calculated for different modulation radii. The results are plotted in Figure 6.9 and show that reducing the modulation radius increases the sensitivity of the pyramid WFS to the segment piston modes. The unmodulated pyramid WFS is the most sensitive to the segment piston modes.

6.6 CONCLUSION

This chapter has shown that the effects of segment piston errors that manifest as a result of the telescope spider can be minimised by optimising the control-loop integrator gain, the amount of regularisation used in the reconstructor and the number of modes reconstructed. The optimised case still has segment piston errors present but significantly reduced.

A new sensitivity metric has been introduced for segment piston errors. By decomposing an interaction matrix formed from segment piston pokes into eigenmodes and eigenvalues, the amplitude of the eigenvalue indicates the sensitivity of the corresponding eigenmode (the larger the eigenvalue, the more sensitive). The modulation radius of the pyramid WFS has a significant effect on the sensitivity of segment piston modes, with the unmodulated pyramid WFS showing the highest sensitivity for all of the segment piston eigenmodes.

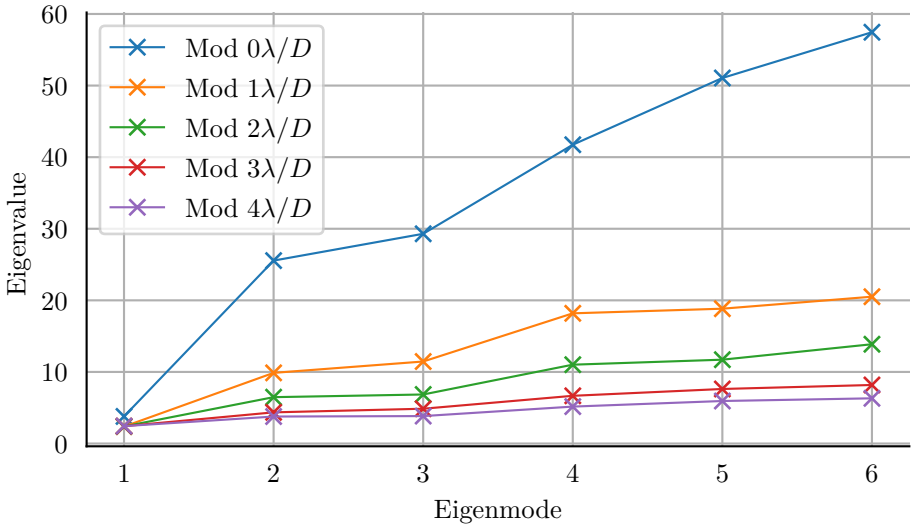

Figure 6.9 The eigenvalues of the six eigenmodes of the segment piston interaction matrix, F_{sp}, for a pyramid WFS in K-band for different levels of modulation radius.

The alignment of the spider with the pyramid edges has a notable impact on closed-loop Strehl. There is a variation in closed-loop Strehl of approximately 15% when a single spider arm is optimally aligned with the pyramid (0 and 90 degrees) compared to the worst-case alignment of 45 degrees. Physically, the optimal alignment corresponds to the spider arm aligning with the pyramid edge.

Optimising the illumination threshold for active subaperture selection is critical for AO systems with thick spiders. From Figure 6.6, the range for best performance is a threshold of 20-50%, which has the effect of including as many subapertures as possible (even poorly illuminated ones) in the wavefront estimation. Optimising the illumination threshold avoids creating extra islands of active subapertures caused by the paraxial spider arm.

The temporal evolution of the segment piston errors is shown to be relatively slow, with greater than 95% of the evolution occuring at a rate of less than 100 Hz. The lower temporal evolution rate of the segment piston errors means a much slower, more sensitive WFS could be used to estimate and correct the segment piston errors.

Chapter 7

SEGMENT PISTON CONTROL WITH A PYRAMID WAVEFRONT SENSOR

A critical component of any AO system is the WFS. The measurements from the WFS are used to estimate the phase of the incoming wavefront. The pyramid WFS is covered in detail in Chapter 3 and Chapter 4. The pyramid WFS has a small dynamic range, when compared to a Shack-Hartmann WFS, because the sensor is only in the linear region when the focal spot is near the apex of the pyramid [Clare and Lane 2005]. A method to overcome the limited dynamic range is to modulate the focal point around the tip of the pyramid and the detector image is summed over each modulation point [Clare and Le Louarn 2011]. This modulation trades sensitivity for dynamic range. For this chapter, the measurement vector, s, of a pyramid WFS is expressed as

$$s = P(\phi) - P(\phi_{\text{flat}}), \tag{7.1}$$

where P is the pyramid operator, ϕ is the phase of the atmospheric wavefront and ϕ_{flat} is a flat (zero) wavefront.

In Chapter 6, an unmodulated pyramid WFS is shown to have an improved sensitivity to segment piston modes compared to a normal modulated pyramid WFS. A modulated pyramid WFS has a larger dynamic range compared to an unmodulated pyramid WFS. This chapter presents a flip-flop modulation scheme, utilising the increased dynamic range of the modulated pyramid WFS and the improved sensitivity to segment piston modes of the unmodulated pyramid WFS. The flip-flop modulation scheme alternates between the modulated and unmodulated states. In this chapter, the flip-flop modulation scheme is first evaluated in pseudo closed-loop end-to-end simulations and then in fully closed-loop end-to-end simulations.

7.1 PSEUDO CLOSED-LOOP FLIP-FLOP MODULATION

All the simulations are performed using the European Southern Observatory's Octopus simulation tool [Le Louarn et al. 2004]. Initially, a pseudo closed-loop scenario of the flip-flop modulation scheme is evaluated, where the modulated pyramid controller

runs in closed-loop. The residual wavefront error is then passed onto an unmodulated pyramid WFS and segment piston reconstructor. The output from the unmodulated pyramid reconstructor is not fed back into the modulated pyramid control loop. The pseudo closed-loop flip-flop method allows the idea to be rapidly evaluated without significantly modifying the Octopus simulation tool. A block diagram of this process is shown in Figure 7.1.

7.1.1 Simulation Procedure

The important simulation parameters for the pseudo closed-loop flip-flop scheme are listed in Table 7.1. The simulations are performed under high flux conditions and an instantaneous change in modulation used. As a proof of concept, the flip-flop modulation technique is implemented in Octopus as two separate simulation runs. First, a closed-loop simulation is performed with a modulated pyramid wavefront sensor and a full modal interaction matrix. At each time-step, the atmospheric phase screen, ϕ_{atm}, and the phase of the DM in the pupil plane, $\phi_{\text{dm\_mod}}$ are saved. The residual phase screen from the modulated pyramid simulation, $\phi_{\text{res\_mod}}$, is calculated by

$$\phi_{\text{res\_mod}} = \phi_{atm} - \phi_{\text{dm\_mod}}. \tag{7.2}$$

Secondly, a closed-loop simulation is performed with an unmodulated pyramid wavefront sensor, using the same atmosphere as the modulated simulation, and an interaction matrix made up of only the six segment piston modes. At each iteration, the phase of the DM in the pupil plane from the modulated simulation is loaded (the unmodulated prism effectively sees the residual wavefront from the modulated simulation). Using the six segment piston mode interaction matrix, the DM phase in the pupil plane is calculated and summed with the modulated pyramid's DM phase screen,

$$\phi_{\text{res\_unmod}} = \phi_{\text{res\_mod}} + \phi_{\text{dm\_unmod}}. \tag{7.3}$$

The resulting residual wavefront has a significantly reduced segment piston error. It should be noted that this is a pseudo closed-loop scenario as the final corrected wavefront is never presented to the modulated pyramid simulation.

7.1.2 Simulation results

The pseudo closed-loop flip-flop pyramid wavefront sensor approach is tested with different levels of atmospheric turbulence (r_0 of 10 cm, 15 cm and 20 cm) representing poor, average and good seeing conditions respectively. The residual phase resulting from the modulated pyramid wavefront sensor path, $\phi_{\text{res\_mod}}$, is analysed by projecting each segment onto the residual phase, $\phi_{\text{res\_mod}}$, effectively taking the mean value over

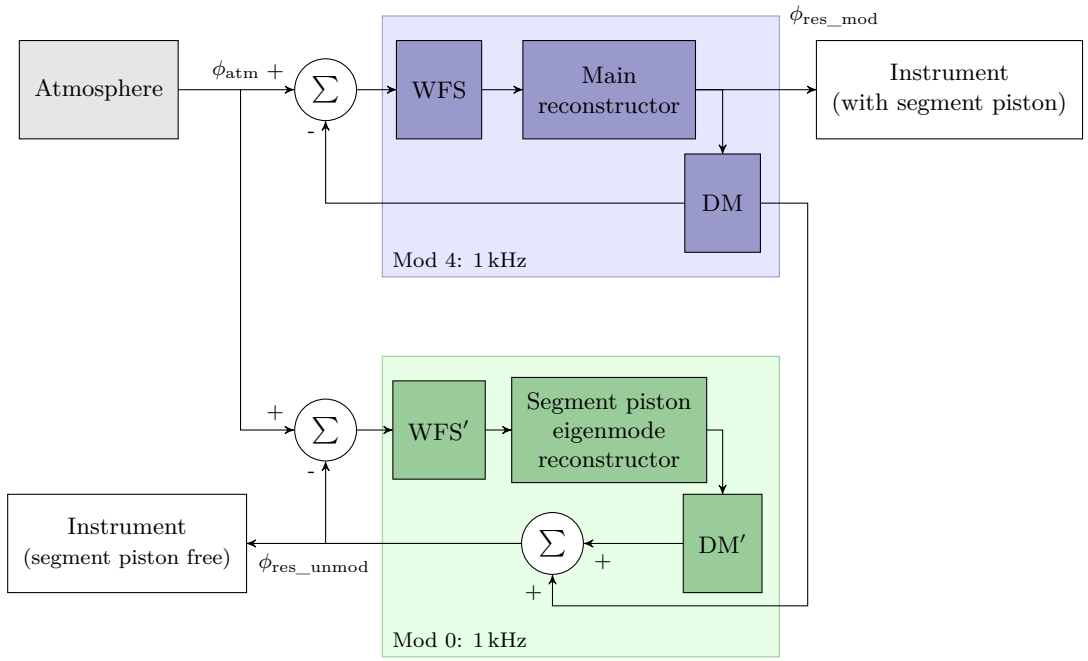

Figure 7.1 A block diagram of how the pseudo closed-loop flip-flop modulated/unmodulated approach is implemented in simulation. This approach is broken into two separate simulation runs: a modulated pyramid and an unmodulated pyramid. First, an atmospheric wavefront is sensed with a modulated pyramid WFS with a full interaction matrix, and at each time-step the DM commands are saved. During the second run (unmodulated), the same atmospheric wavefront is used but this time an unmodulated pyramid WFS with an interaction matrix of just the six segment piston modes is used. At each time step, the DM command generated by the unmodulated pyramid WFS and the corresponding DM command from the modulated WFS are summed and used to correct the wavefront.

each segment,

$$\text{sp}_n = P_{\text{sp}n} \cdot \phi_{\text{res\_mod}}, \tag{7.4}$$

where sp_n is the residual piston in segment n and $P_{\text{sp}n}$ is the pupil mask for segment n. Then the unmodulated path is run and the resulting residual phase screens are again analysed and the segment piston measured. The segment piston error over a single segment is plotted over time in Figure 7.2, showing the amount of segment piston error before and after using an unmodulated pyramid wavefront sensor to correct the segment piston. The flip-flop method significantly reduces segment piston, even in challenging seeing conditions.

As a measure of PSF quality, the Strehl ratio is computed using the residual phase screens before and after the unmodulated prism is used for segment piston correction. The temporal evolution of the closed-loop short exposure Strehl is shown in Figure 7.3. The long exposure Strehl is summarised in Table 7.2. Even under poor atmospheric conditions, the flip-flop modulated/unmodulated segment piston control method improves the closed-loop Strehl by 3.4% (from 63.9% to 67.3%) and under the best atmospheric conditions tested, a 4.4% improvement in the closed-loop Strehl (from

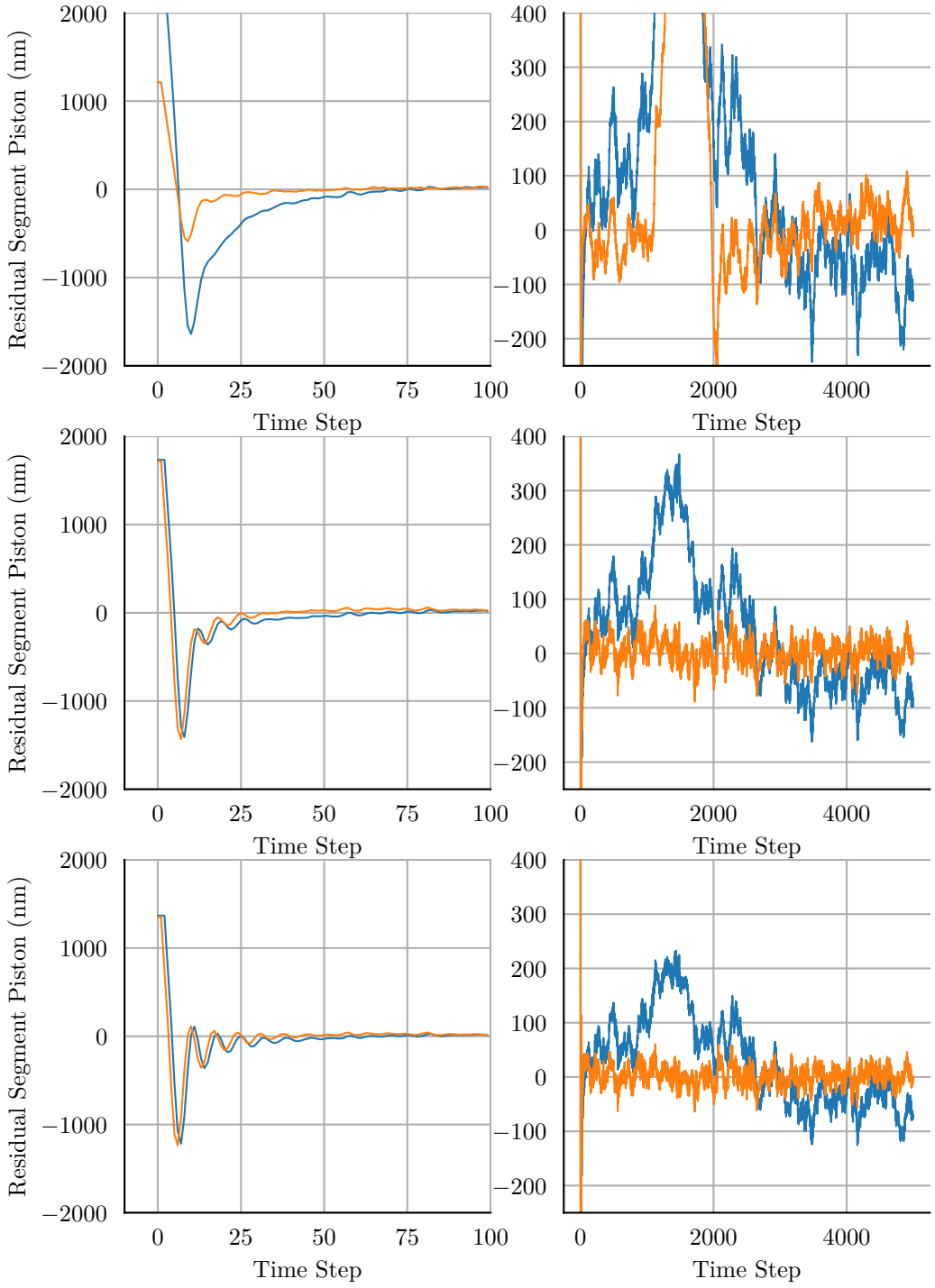

Figure 7.2 Temporal evolution of the residual segment piston, without (blue) and with (orange) the pseudo closed-loop flip-flop modulated/unmodulated method for segment piston control, where the atmosphere has an r_0 of 10cm (top), 15cm (middle) and 20cm (bottom). The left column shows the first 100 iterations as the loop closes and the full duration of the simulation is shown in the right column.

Table 7.1 Pseudo closed-loop simulation parameters used in this chapter.

Parameter	Value
Telescope Diameter (D)	37 m
Fried parameter (r_0)	10 cm, 15 cm, 20 cm
Outer Scale (L_0)	25 m
Atmosphere	ESO 35 layer model
Frame Rate (F_s)	1 kHz
Delay	2 Frames
WFS Wavelength (λ_W)	2200 nm
WFS Order	116 × 116 Subapertures
PSF Wavelength	2200 nm
Modulation Width	$4\lambda_W/D$, $0\lambda_W/D$
Time Steps	5000
Number of Spider Arms	6
Spider Arm Width	50 cm
Flux	10000 photons/subaperture/frame
Number of Actuators	5190
Number of Modes	5190

Table 7.2 Comparison of the long exposure Strehl for the pseudo closed-loop flip-flop modulation scheme under different atmospheric conditions.

Seeing	Strehl with normal modulation	Strehl with flip-flop modulation
poor	63.9%	67.3%
median	80.0%	88.0%
good	88.0%	92.4%

88.0% to 92.4%) is shown.

7.2 FULLY CLOSED-LOOP FLIP-FLOP MODULATION METHOD

In this section, the fully closed-loop flip-flop modulation scheme is presented. Figure 7.4 shows a block diagram of the flip-flop modulation scheme, where two separate reconstructors are used. One reconstructor corrects the bulk of the atmospheric turbulence, using a Karhunen-Loève (KL) basis. The other reconstructor corrects for segment piston modes only and consists of the segment piston eigenmodes (excluding pure piston). The segment piston reconstructor takes measurements from an unmodulated pyramid while the atmospheric reconstructor takes measurements from a modulated pyramid. By using a single pyramid and switching between a modulated and unmodulated state, both reconstructors use the same optical hardware. A similar control structure could be implemented with separate modulated and unmodulated pyramids, removing the

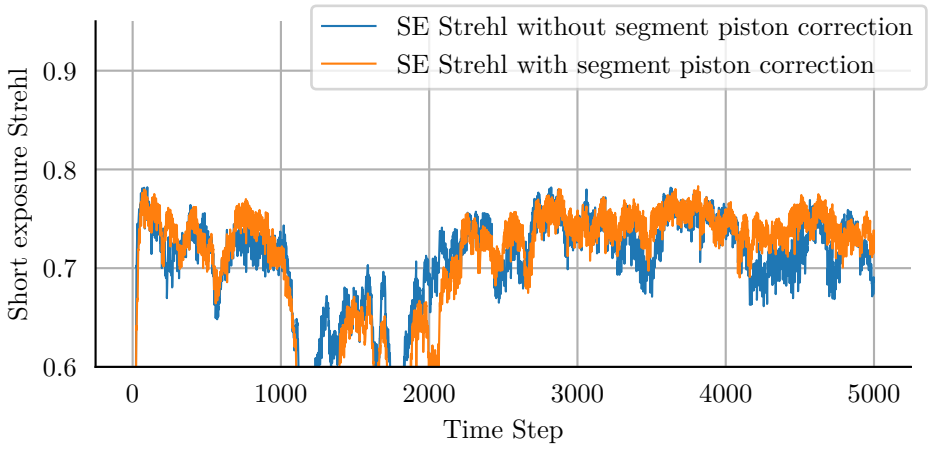

(a)

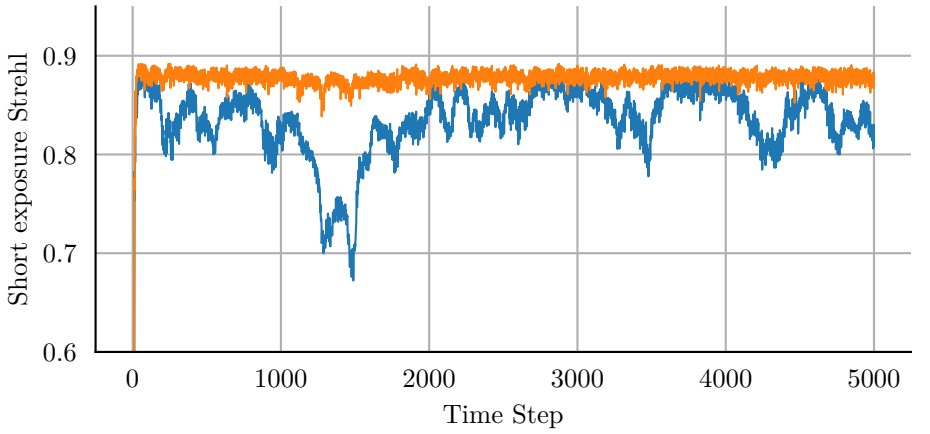

(b)

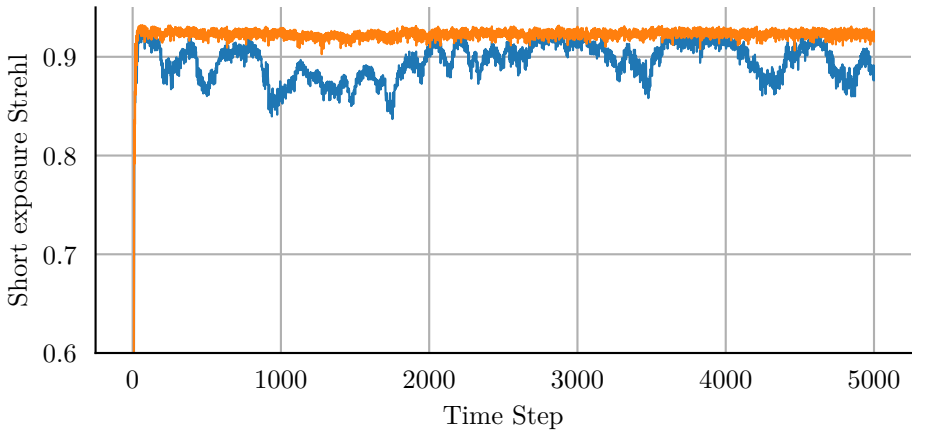

(c)

Figure 7.3 The short exposure, closed-loop K-band Strehl for a pyramid WFS with a modulation of $\frac{4\lambda}{D}$ (blue), and for the pseudo closed-loop flip-flop modulated/unmodulated method (orange). The performance is evaluated for an r_0 of 10 cm (a), 15 cm (b) and 20 cm (c).

need to stop the modulation, but would require splitting the light.

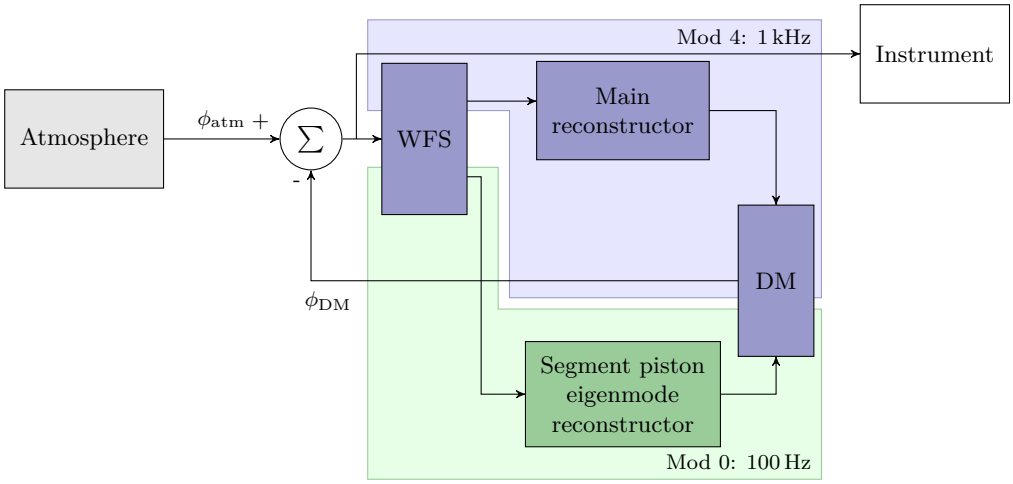

Figure 7.4 The flip-flop modulation pyramid WFS. Two AO control loops operate with a single pyramid. The modulation and associated control loop is switched on and off, allowing the increased dynamic range of a modulated pyramid (blue) for correcting the majority of the atmospheric turbulence and the improved sensitivity of an unmodulated pyramid WFS (green) to control the segment piston modes.

Using the following steps, is is possible to control segment piston errors with a pyramid WFS:

1. Find a modal basis for correcting the segment piston modes.
2. Find a modal basis for correcting the atmospheric turbulence, which is also orthogonal to the segment piston modes.
3. Find the optical gains of the segment piston modal basis, for an unmodulated pyramid.
4. Find the optical gains of the atmospheric modal basis, for a modulated pyramid.
5. Build reconstructors for both modulated and unmodulated loops, with optical gain compensation.
6. Run the AO system and correct segment piston errors.

7.2.1 Finding a modal basis for the unmodulated pyramid

The choice of modal basis is a critical step in controlling the segment piston modes. Using the technique outlined in Chapter 6, the segment piston eigenmodes and eigenvalues are calculated. The resulting segment piston eigenmodes, Z_{eigen}, and the corresponding segment piston eigenvalues are shown in Chapter 6. In this chapter, the unmodulated pyramid WFS is only used to control segment piston modes. In future work, the number of modes controlled by the unmodulated pyramid WFS could be increased.

7.2.2 Finding a modal basis for the modulated pyramid

The modulated pyramid WFS is used to control the bulk of the atmospheric turbulence, due to the increased dynamic range from the modulation. This enables the AO system to reliably close the loop. To produce an efficient reconstructor, it is useful to have an orthogonal modal basis. The modal basis is orthogonalised twice, once with respect to the actuator geometry and a second time with respect to the atmospheric covariance. This process of double diagonalisation is described in [Gendron 1995, Lai et al. 2000]. A key step is the computation of the atmospheric covariance, $\langle h_i h_j \rangle$, which is defined as:

$$\langle h_i h_j \rangle = \mathrm{Re}\Big[\sum_{u=0}^{U-1} \sum_{v=0}^{V-1} (\mathcal{F}[\mathrm{IF}_i(x,y)]^* \cdot \mathcal{F}[\mathrm{IF}_j(x,y)] \cdot \mathrm{PSD}_\phi(u,v) \cdot df^2) \Big], \tag{7.5}$$

where PSD_ϕ is the power spectral density of the atmospheric turbulence, IF is a single influence function of the DM (as shown in Figure 7.5), df is the frequency step size used in PSD_ϕ, U and V are the number of elements in the u and v axes respectively. The statistical covariance matrix Δ_{stat} is defined as:

$$\Delta_{\mathrm{stat}} = \begin{bmatrix} \langle h_1 h_1 \rangle & \langle h_1 h_2 \rangle & \dots & \langle h_1 h_j \rangle \\ \vdots & \ddots & & \vdots \\ \langle h_i h_1 \rangle & \dots & & \langle h_i h_j \rangle \end{bmatrix}. \tag{7.6}$$

It is useful to be able to force certain modes to be present (initially these will be piston, tip and tilt), regardless of the double orthogonalisation steps. For example, the tip and tilt can be offloaded to a separate control system. For each actuator in the DM, the influence function is flattened into a row vector. The influence function row vectors are stacked into a matrix IF, where the row is indexed by the actuator number. The first 20 modes, excluding piston, for a KL modal basis, which is forced orthogonal to piston, tip and tilt are shown in Figure 7.6.

A modal basis, which is forced to be orthogonal to the segment piston eigenmodes, is also needed. If the segment piston eigenmodes are present in the modal basis used by the modulated pyramid WFS, the two controllers (modulated and unmodulated) will contest each other. The first 20 segment piston-free modes are shown in Figure 7.7.

7.2.3 Optical gain compensation for the pyramid

Now that a modal basis for each control loop has been defined, a reconstructor that accurately reconstructs a wavefront from a pyramid WFS measurement is required. The pyramid WFS frequency response is not linear [Deo et al. 2018, Korkiakoski et al. 2008], especially in the presence of AO residual. The effective gain for each mode is not unity. This phenomenon is known as the optical gain problem. To solve the optical gain problem, the effective gain for each mode needs to be found. Interaction matrices

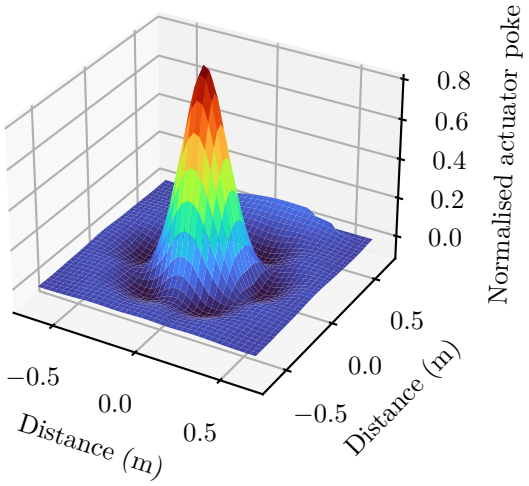

Figure 7.5 An influence function of the EELT deformable mirror (M4), derived from finite element analysis and interpolated to the primary mirror space (M1).

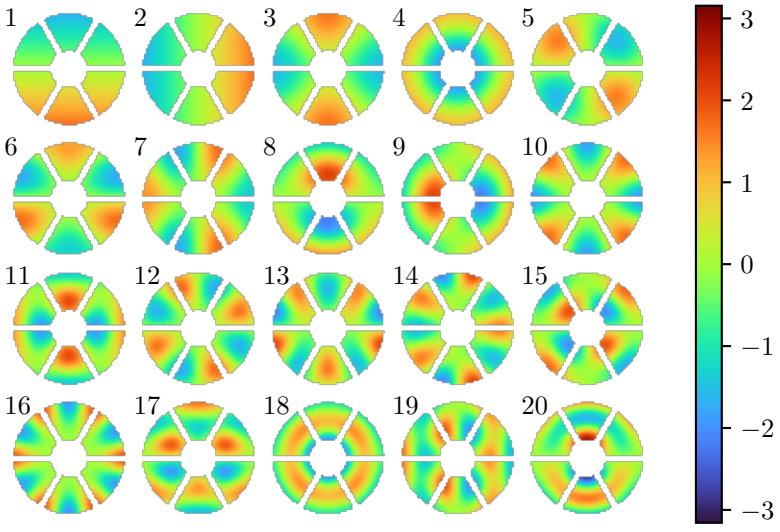

Figure 7.6 The first 20 KL modes (excluding piston), forced to be orthogonal to piston, tip and tilt, which are produced using the double orthogonalisation method, without forcing orthogonality to the six petal eigenmodes (normalised to an RMS of 1 nm).

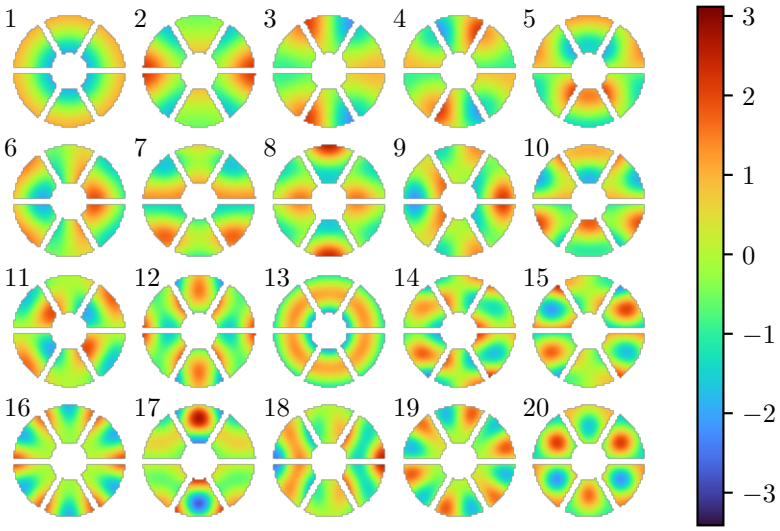

Figure 7.7 The first 20 KL modes (excluding piston), forced to be orthogonal to the six segment piston eigenmodes, which are produced using the double orthogonalisation method.

capturing the response of the pyramid WFS to each mode in the basis are measured for both a diffraction-limited case, and with AO residual present. The AO residual fitting error, ϕ_{fit}, is found by subtracting the projection of each mode in the basis from an atmospheric phase screen

$$\phi_{\text{fit}}(x,y) = \phi_{\text{atm}}(x,y) - \sum_{i=1}^{N} \phi_{\text{atm}}(x,y) \cdot \phi_{Z_i}(x,y), \tag{7.7}$$

where N is the number of modes in the modal basis and $\phi_{Z_i}(x,y)$ is the phase of the i^{th} mode in the modal basis. The DM command, ϕ_{DM}, is calculated as follows:

$$\phi_{DM} = Bs, \tag{7.8}$$

where B is the modal command matrix which has optical gain compensation applied and s is the measurement vector from the pyramid WFS. B is defined as:

$$B = Z \cdot (\frac{1}{OG} \cdot F^{\dagger}), \tag{7.9}$$

where Z is the modes-to-command matrix, F is the modal interaction matrix and $\dagger$ denotes the pseudoinverse. OG is defined as [Chambouleyron et al. 2020]

$$OG = \frac{diag(F_{\text{res}}^T \cdot F_{\text{diff}})}{diag(F_{\text{diff}}^T \cdot F_{\text{diff}})}, \tag{7.10}$$

where F_{res} is the interaction matrix in the presence of AO residual and F_{diff} is the diffraction-limited interaction matrix. The optical gains are calculated for both the

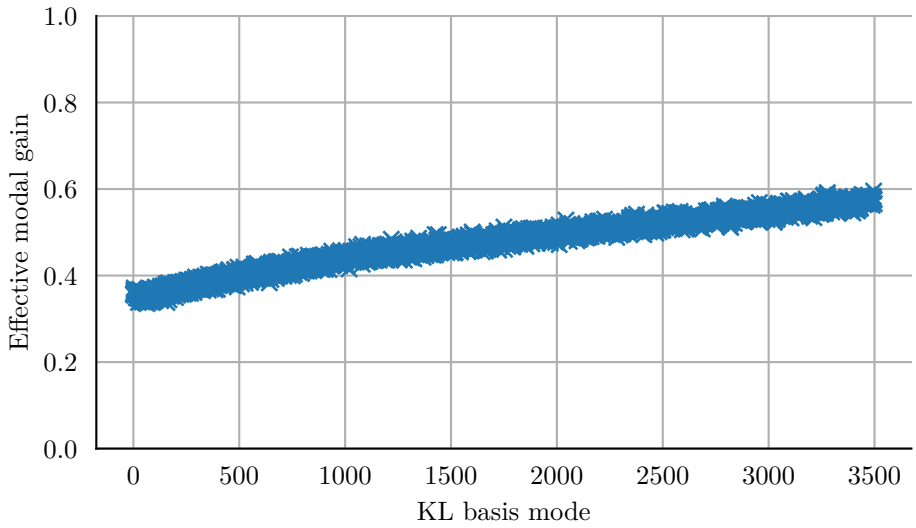

Figure 7.8 The optical gains of the segment piston-free KL modes (Figure 7.7) for a modulated pyramid WFS operating in R-band, using the default parameters from Table 7.1.

modulated pyramid WFS with the entire modal basis, and the unmodulated pyramid WFS with only the segment piston eigenmodes. The optical gains for the modulated pyramid WFS are shown in Figure 7.8, and the optical gains for the segment piston eigenmodes are shown in Figure 7.9.

7.2.4 Reference measurement in the presence of AO residual

When testing the unmodulated pyramid WFS reconstructor (with optical gain compensation), it is found that certain segment piston eigenmodes present an offset. The eigenmode offset is demonstrated in Figure 7.12, where a 50 nm poke for each eigenmode is presented to the unmodulated pyramid WFS. In the ideal case, the reconstructed wavefront should match the eigenmode poke, as is the case for eigenmodes one through three, where a 50 nm poke of each eigenmode is reconstructed with negligible modal crosstalk. For a 50 nm poke of eigenmode five, however, only 30 nm is reconstructed, as well as -35 nm to -30 nm of the other four eigenmodes.

The standard method, Equation (7.1), of forming a measurement from a pyramid WFS consists of subtracting a null reference measurement from the turbulence measurement. In the case of the diffraction-limited unmodulated pyramid WFS, the null reference measurement as shown in Figure 7.10, has a significantly different average value than that of the reference measurement measured in the presence of AO residual, as shown in Figure 7.11. Due to the reduced amplitude of the null reference measurement, the traditional reference measurement subtraction overcompensates for the zero reference. Figure 7.12 also suggests that the measurement signal for eigenmode five is similar to the null reference.

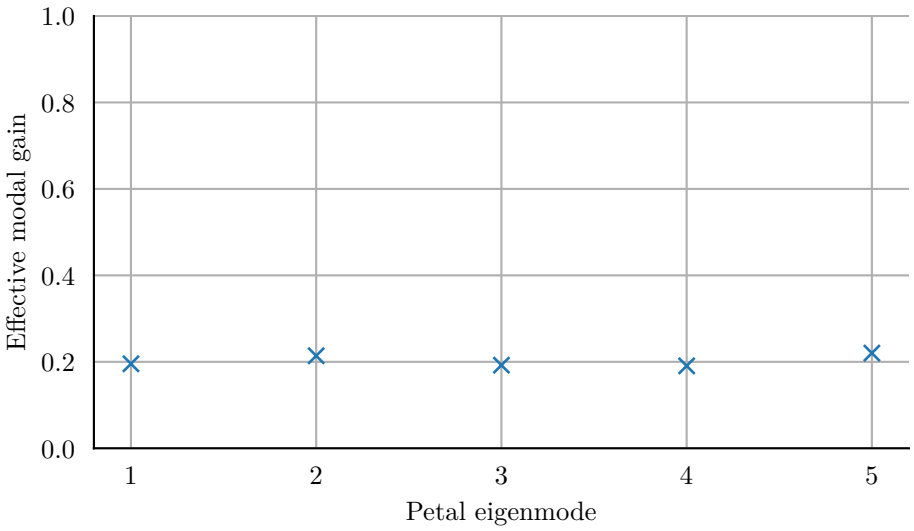

Figure 7.9 The optical gains of the segment piston eigenmodes for an unmodulated pyramid WFS operating in R-band, using the default parameters from Table 7.1.

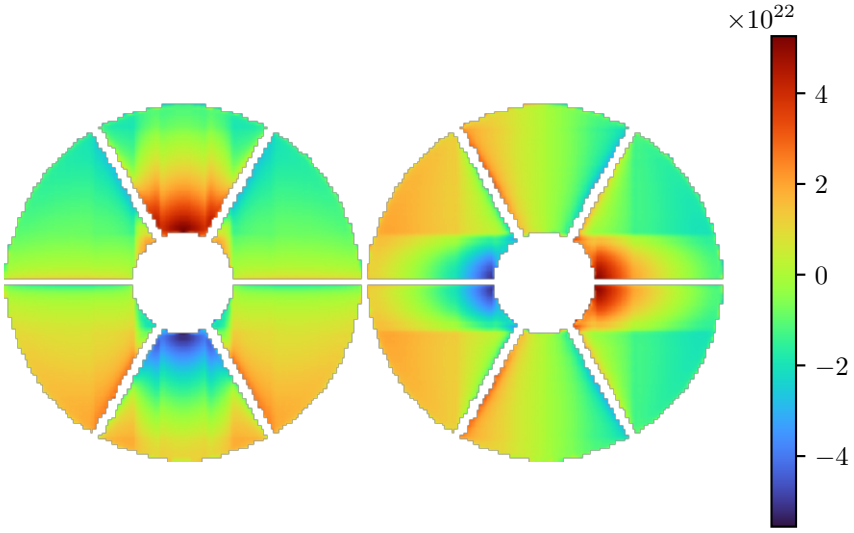

Figure 7.10 The simulated slopes map (unitless) from an umodulated pyramid WFS where the input wavefront is flat (zero across the entire pupil).

If instead, the reference measurement is not subtracted, the offset decreases and the segment piston reconstruction improves significantly, as shown in Figure 7.13. The decrease in the offset is effectively an optical gain of the reference measurement, and can be found via a similar process as that used for calculating modal optical gains. The reference measurement in the presence of AO residuals is effectively the diffraction-limited measurement scaled by some gain factor,

$$s_{\text{ref}} = \frac{s_{\text{diff}}}{k}, \tag{7.11}$$

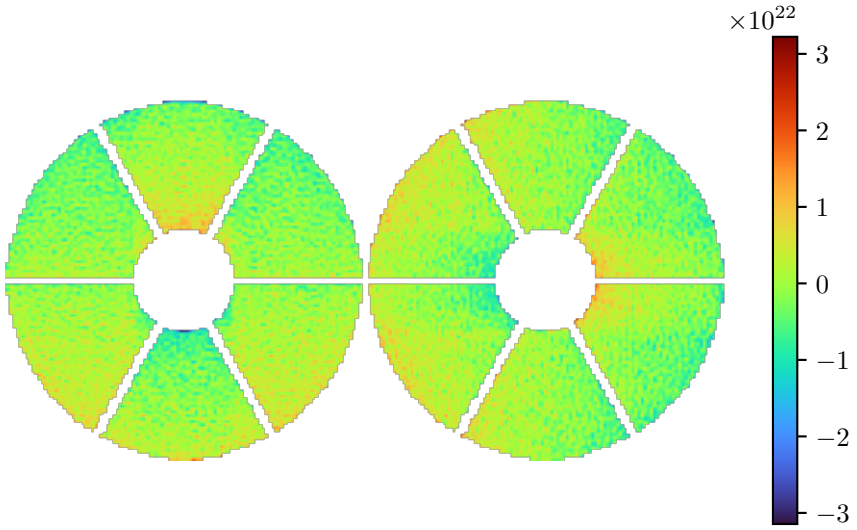

Figure 7.11 The simulated slopes map (unitless) from an umodulated pyramid WFS where the input wavefront is the residual fitting error obtained by removing the first 3500 modes from an atmospheric phase screen, averaged over 100 phase screens.

where k is the optical gain of the reference signal, s_{diff} is the diffraction limited reference signal and s_{ref} is the optical gain compensated reference signal. k is defined as [Deo et al. 2018]:

$$k = \frac{s_{\text{res}}^T \cdot s_{\text{diff}}}{s_{\text{diff}}^T \cdot s_{\text{diff}}}, \tag{7.12}$$

where s_{res} is the pyramid WFS measurement signal in the presence of AO residuals. For the test case defined by Table 7.3, k is found to be approximately 0.23. This closely matches the optical gains for the segment piston eigenmodes in Figure 7.9. By applying what is in essence an optical gain correction to the null reference measurement, the segment piston reconstruction is improved further. The segment piston reconstruction with optical gain compensation on both the reconstructor and null wavefront reference measurement are shown in Figure 7.14. By applying the optical gain correction to the reference measurement, the offsets for certain segment piston eigenmodes are now significantly reduced and the cross-talk between modes is reduced.

7.2.5 A flip-flop modulation pyramid wavefront sensor

The flip-flop approach introduces several new control points to the system, which will all affect the overall performance of the system. These include the duty cycle of the unmodulated loop, the amount of dead-time used when switching between modulation regimes (allowing the modulator time to change path), the loop gains for each control loop and the frequency of both control loops. This significantly increases the amount of time to find optimal settings for the entire control system.

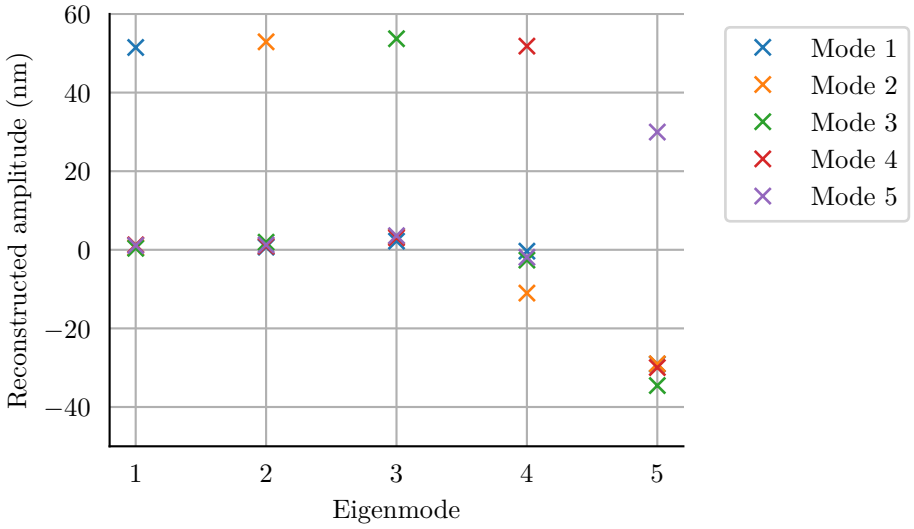

Figure 7.12 The reconstructed amplitude for a 50 nm poke of each segment piston eigenmode in the presence of AO residual. The reconstructor has had optical gain compensation applied to modes, and the standard reference measurement subtraction is applied.

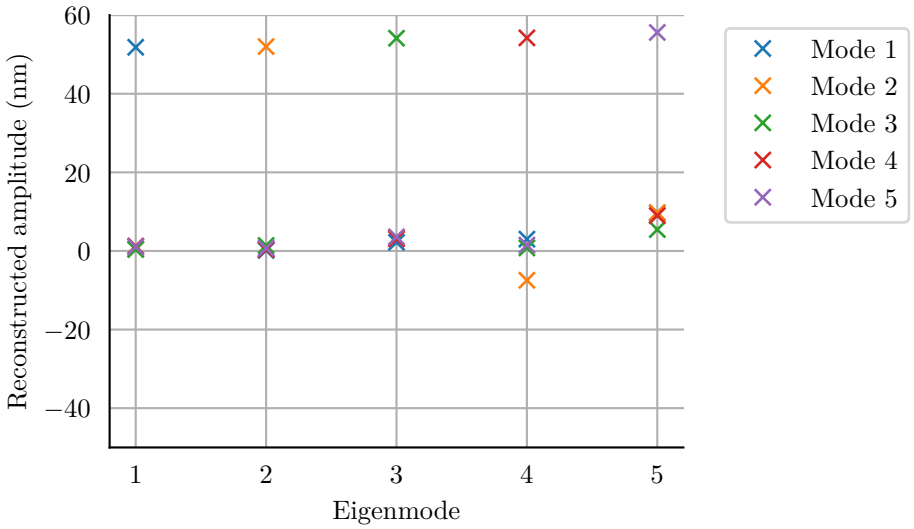

Figure 7.13 The reconstructed amplitude for a 50 nm poke of each segment piston eigenmode in the presence of AO residual. The reconstructor has had optical gain compensation applied to modes, and no reference measurement is subtracted.

7.2.6 Simulation Results

All of the simulations in this section are performed using Octopus, employing the parameters listed in Table 7.3. A nominal wavelength of 650 nm or 2200 nm is used for both the PSF and the WFS, in R and K-band, respectively. The main modulated pyramid WFS AO loop is running at 1 kHz, and the segment piston correction loop with the unmodulated pyramid WFS is effectively running at 100 Hz as the modulation

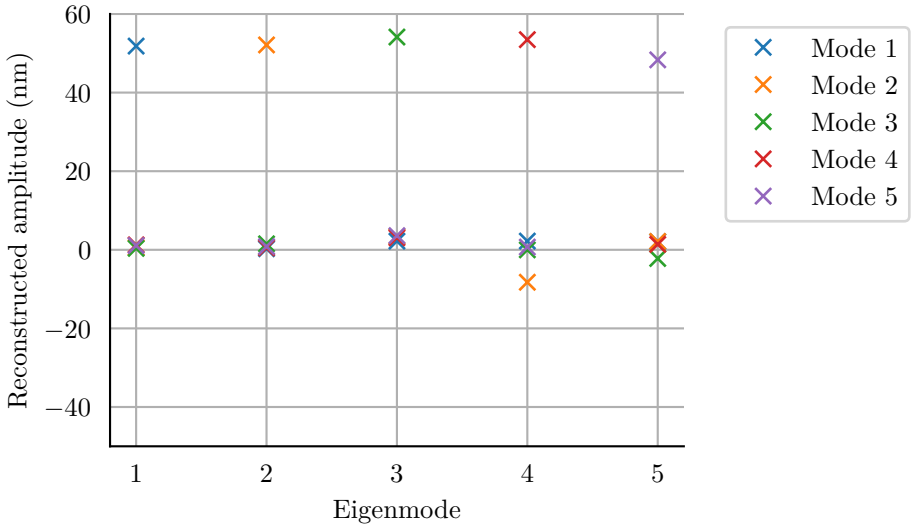

Figure 7.14 The reconstructed amplitude for a 50 nm poke of each segment piston eigenmode in the presence of AO residual. The reconstructor has had optical gain compensation applied to modes as well as the reference measurement.

is stopped every 10 iterations. In a real system, the tip/tilt mirror used to introduce the modulation is not able to stop or start the modulation instantly. To account for this in simulation, a dead-frame is inserted before and after each single unmodulated pyramid WFS measurement.

7.2.6.1 K-band scenario

In K-band, it is possible to close the loop either with or without the proposed flip-flop method. With the proposed flip-flop modulation method, an improvement in closed-loop long exposure Strehl of 8.3% (Table 7.4) is observed over the Strehl of the standard modulated case. Figure 7.15 compares the short exposure Strehl, measured in K-band, using normal modulation, with the flip-flop method. Once the loop has converged, the flip-flop modulation method has a consistently higher short exposure Strehl than the standard modulated pyramid. The resulting long exposure PSFs are shown in Figure 7.16, where an improvement in the PSF core is clearly visible with the flip-flop method.

The flip-flop modulation method is able to sense and correct large (400 nm peak-to-valley) segment piston errors in the atmospheric wavefront. Figure 7.17 shows the short exposure Strehl, measured in K-band, using the flip-flop method with a 400 nm peak-to-valley segment piston waffle (an alternating push and pull of segment piston) mode injected into the atmospheric phase from iteration 250. The short exposure Strehl returns to the baseline level within 25 iterations.

Table 7.3 Full closed-loop flip-flop simulation parameters used in this chapter.

Parameter	Value
Telescope Diameter (D)	37 m
Fried Parameter (r_0)	15 cm
Outer Scale (L_0)	25 m
Atmosphere	ESO 35 layer model
Frame Rate (F_s)	1 kHz
Delay	2 Frames
PSF (λ_p) Wavelength	2200 nm (K-band), 650 nm (R-band)
WFS (λ_W) Wavelength	2200 nm (K-band), 650 nm (R-band)
WFS Order	116 × 116 Subapertures
Modulation Width	$4\lambda_W/D$, $0\lambda_W/D$
Time Steps	1000
Number of Spider Arms	6
Spider Arm Width	50 cm
Flux	10000 photons/subaperture/frame
Number of Actuators	5190
Number of Modes	3500

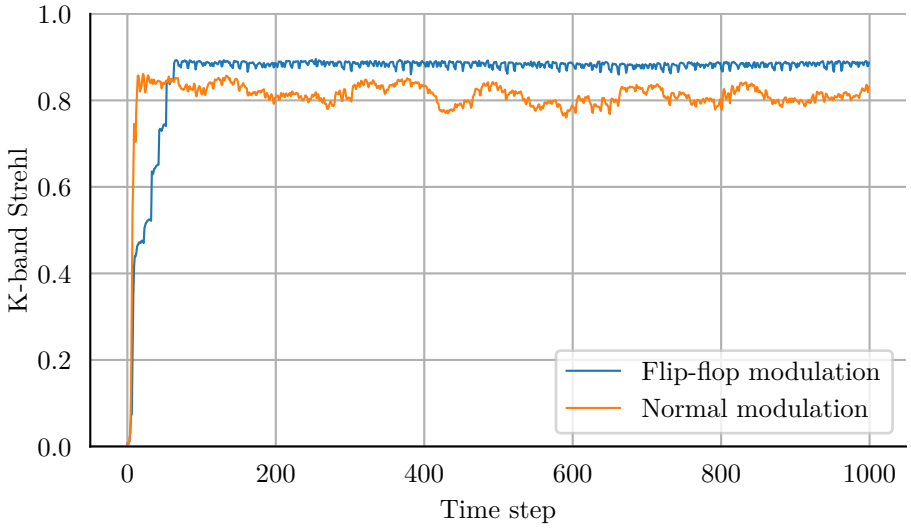

Figure 7.15 The short exposure Strehl, measured in K-band, comparing the flip-flop modulation method (blue) with the traditional modulation method (orange).

7.2.6.2 R-band scenario

In R-band, if the segment piston modes are not controlled, it is not possible to close the loop in simulation, due to excessive segment piston. Using the flip-flop modulation approach, it is possible to sense and correct segment piston modes, resulting in stable closed-loop performance, as shown in Figure 7.18, with a closed-loop long exposure Strehl of 18.7%.

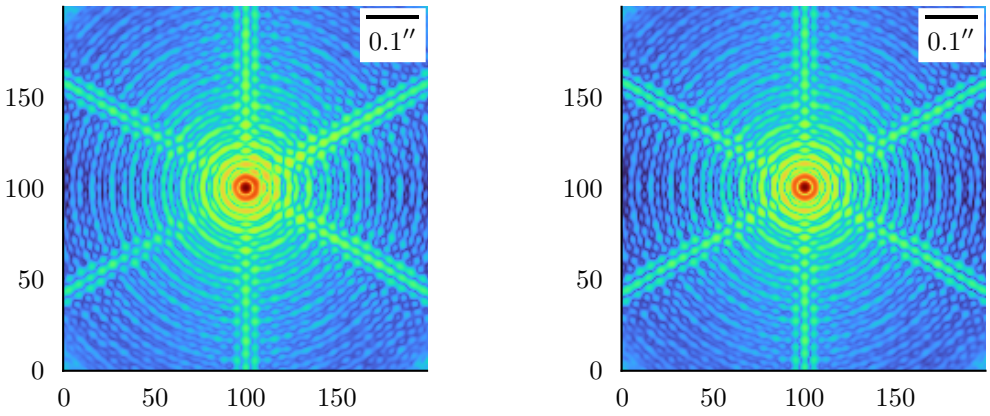

Figure 7.16 The long exposure point spread function simulated in K-band, with the WFS also operating in K-band, without (a) and with (b) the flip-flop modulation.

Table 7.4 Long exposure Strehl for R and K bands.

Band	Strehl with flip-flop modulation	Strehl with normal modulation
K	87.6%	79.3%
R	18.7%	6.6%

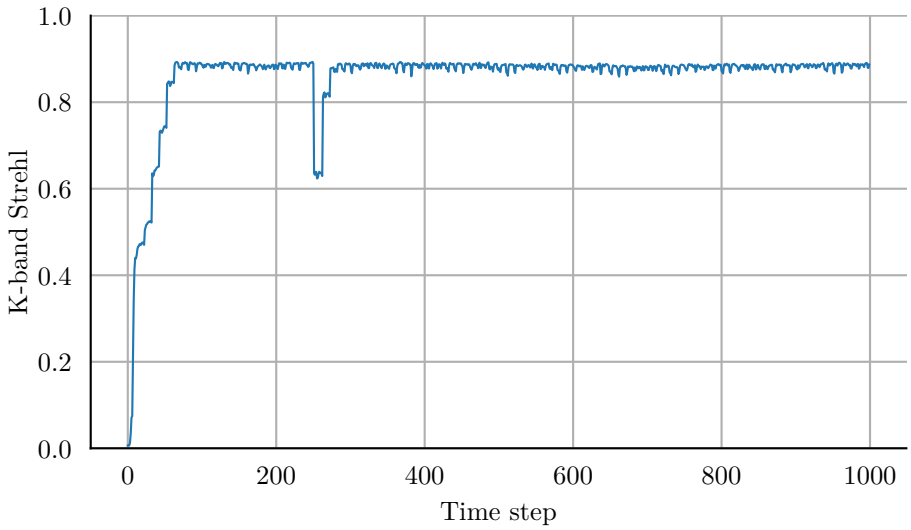

Figure 7.17 The short exposure Strehl, simulated in K-band, using the flip-flop modulation method and the simulation parameters from Table 7.1. From time step 250, a segment piston waffle mode of 400 nm peak-to-valley is applied to the incoming wavefront.

The Maréchal criterion approximates the Strehl ratio

$$\text{Strehl} \approx e^{-(\frac{2\pi\epsilon}{\lambda})^2}, \tag{7.13}$$

where ϵ is the RMS wavefront error in metres and λ_p is the wavelength in metres. By taking an atmospheric phase screen and removing the projection of each of the 3500 modes in the KL modal basis including tip and tilt (before it has been forced orthogonal to segment piston eigenmodes), the RMS fitting error, ϵ, is approximately 110 nm, resulting in a Strehl of 32.3%. This Strehl only includes fitting error and represents the best case closed-loop performance, before accounting for temporal effects, giving an upper bound for the closed-loop Strehl. The flip-flop modulation method is achieving closed-loop Stehl close to the fitting error, considering the fitting error does not account for any temporal errors.

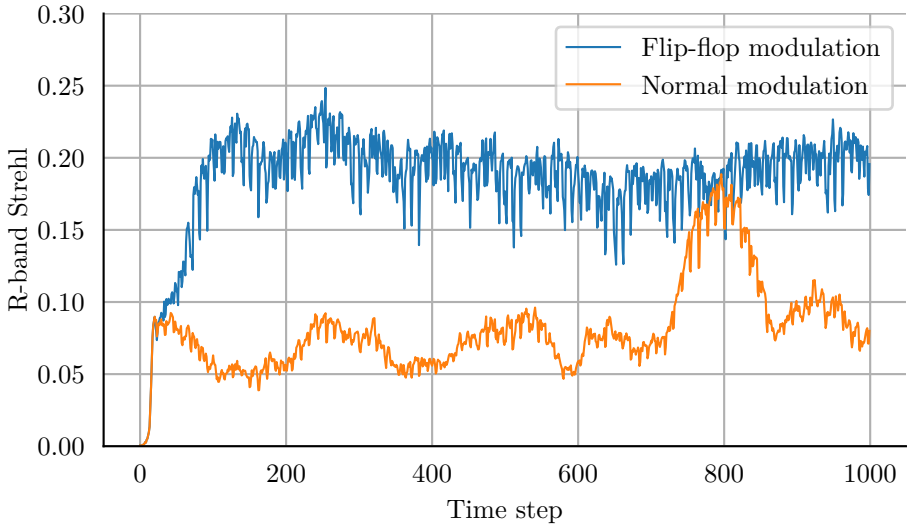

Figure 7.18 The short exposure Strehl, measured in R-band, comparing the flip-flop modulation method (blue) with the traditional modulation method (orange).

In this method, the absolute position of each segment piston is not known, however the segment piston errors are controlled relative to some offset (2π ambiguity). In these monochromatic simulations, the segment piston errors were corrected, relative to some absolute offset. Not knowing what the value of the absolute offset is had no detrimental effect on the PSF.

The long exposure PSFs are shown in Figure 7.19, where using the flip-flop method an Airy disk is visible and the six diffraction spikes from the spider arms are just visible, unlike the PSF from the standard modulated scheme, where an Airy disk is not visible and the diffraction spikes are less prominent.

7.3 CONCLUSION

This chapter presents a new flip-flop modulation method for controlling segment piston errors, which is shown working in simulation, in both R and K-band with an r_0 of 15 cm. The improvement of the flip-flop method versus a standard modulated pyramid WFS,

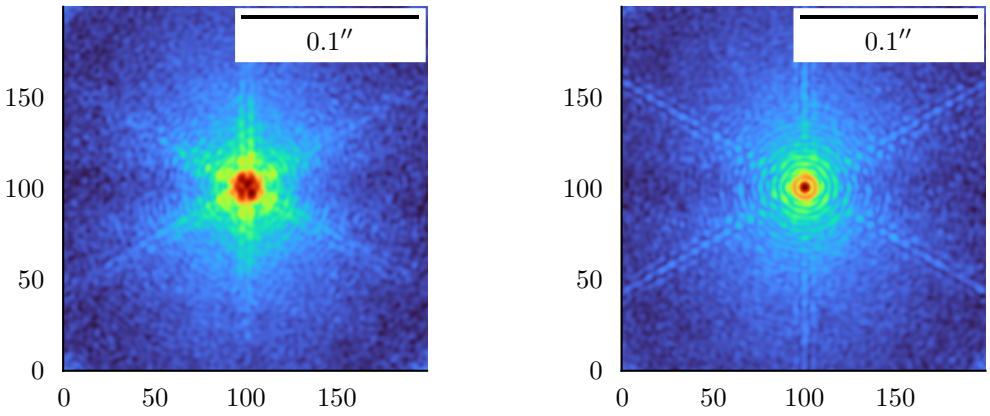

(a) (b)

Figure 7.19 The long exposure point spread function simulated in R-band, with the WFS also operating in R-band, without (a) and with (b) the flip-flop modulation.

in long exposure Strehl for K and R band, after 1000 iterations, is 8.3% and 12.1% respectively. The flip-flop modulation method introduces several new parameters that could be further optimised, such as the duty cycle and frequency of the unmodulated pyramid WFS loop.

The simulations only cover the monochromatic case, where a 2π phase ambiguity has no detrimental effect on the PSF. In future work, it will be interesting to explore the flip-flop method with polychromatic light sources. Adding to the optical gain corrections of the reference signal of the pyramid, implementing a filter for the pyramid WFS measurement signal, which is matched to the segment piston eigenmode measurement signal, could further increase the SNR.

Chapter 8

CONCLUSION AND FUTURE WORK

This thesis investigates issues arising in AO systems in the context of ELTs. This chapter serves to summarise the original contributions to the field of AO, contained in Chapter 4, Chapter 5, Chapter 6 and Chapter 7. As a result of the research in this thesis, there are several areas for further reserach, which are outlined in Section 8.2.

8.1 CONCLUSIONS

All ground-based telescopes are faced with the challenge of imaging through Earth's time-varying atmosphere. The atmosphere introduces phase distortions to the incoming wavefronts from astronomical targets. The phase distortions can be corrected with a real-time AO system or by post-processing the images. This thesis makes contributions to AO, specifically within the area of wavefront sensing and estimation with a pyramid WFS.

Due to the manufacturing tolerances required to manufacture a pyramid, the cost is typically high. These manufacturing tolerances are reduced for a 2-sided or 3-sided prism. Chapter 4 investigates the effects of the prism geometry (number of sides) on the closed-loop AO performance, with end-to-end simulations. The findings of this research are that under high flux scenarios (high SNR), there is little separating the roofs (two 2-sided), 3-sided, pyramid and 6-sided prism WFS, which matches the analytical results shown by Fauvarque et al. [Fauvarque et al. 2016]. However, in a low flux scenario with readout noise, the 3-sided WFS performs 11.4% better than the pyramid WFS in the same conditions. The performance improvement can be attributed to the reduced number of pupil images of the 3-sided WFS, providing a higher SNR.

Investigating different prism geometries for Fourier WFS can be a time consuming and expensive endeavour. To save time and money, a digital Fourier WFS has been developed in the laboratory. A SLM is used to introduce the optical path difference equivalent to a glass prism, allowing any geometry of prism to be evaluated. For the first time, digital 3-sided and cone WFSs have been demonstrated, along with a pyramid and 6-sided WFS. The linearity of the digital unmodulated 3-sided, pyramid, 6-sided

and cone WFS has been demonstrated experimentally for the first 12 modes.

The support structure which holds the secondary mirror in place is known as a spider. As telescopes have increased in size, these spiders have become larger. For the ELTs, the spider arms can be wider than a subaperture of the WFS, and the typical r_0 at the observatory site. The thick spiders effectively subdivide the pupil into segments. The segmented pupil presents a significant challenge to wavefront estimation and control as each segment is effectively independent and the mean of the wavefront over each segment is different (segment piston errors). Making matters worse, the modulated pyramid WFS, which is the WFS of choice for ELTs, poorly senses segment piston modes. By optimising the illumination threshold for active subaperture selection, the amount of regularisation used in calculating the command matrix, and reducing the number of modes used in the wavefront estimation, the wavefront estimation in the presence of thick spiders can be improved.

A new sensitivity metric, the eigenvalues of the interaction matrix, for the sensitivity of a pyramid WFS to segment piston modes has been developed. This metric shows that the unmodulated pyramid WFS provides a significant increase in sensitivity when compared to a modulated pyramid WFS.

Having shown that an unmodulated pyramid WFS is sensitive to segment piston modes, a flip-flop modulation method is introduced. The flip-flop modulation method for a pyramid WFS alternates between the modulated and unmodulated states, combining the increased dynamic range of a modulated pyramid WFS and the increased sensitivity to segment piston modes of the unmodulated pyramid WFS. The flip-flop method has been evaluated in end-to-end simulations in both K and R-band, providing a 8.3% and 12.1% improvement in the long exposure Strehl respectively, when compared to a standard modulated pyramid WFS under expected atmospheric conditions.

8.2 FUTURE RESEARCH

Continuing the N-sided prism simulations, investigating the cone WFS with Octopus would be very interesting and will complete the N-sided prism research. Further work is required on the processing of the cone WFS detector image to fully utilise the information captured.

In the current configuration of the 3-sided WFS in Octopus, the x slope utilises measurements from all three of the pupil images, whilst the y slope only uses measurements from two pupil images. It will be interesting to investigate whether rotating the prism relative to the detector such that the x and y slopes use the same number of pupil images improves the wavefront estimation from the 3-sided WFS.

The unmodulated digital Fourier WFS was evaluated in an open-loop configuration. In future work, developing a fully closed-loop system would allow a more in-depth

analysis of the performance of different prism geometries in a more realistic environment. Adding a second SLM to introduce wavefront aberrations, a fast tip/tilt mirror for modulation, and a high order DM would be needed. Currently, the Fourier WFS is using simple prism geometries. In future work, it will be interesting to explore the generation of optimal Fourier masks to further improve the performance of Fourier based (pyramid) WFSs.

The flip-flop modulation method for the pyramid WFS has been shown to successfully control segment piston errors in simulation, in a monochromatic, high flux scenario. Future work could evaluate the flip-flop method in a low-light environment and under worst-case atmospheric conditions. It will also be interesting to evaluate the flip-flop method with chromatic light, similar to that which will be present at the telescope.

As Hutterer et al. [Hutterer et al. 2018] have shown that the measured signal for segment piston modes is concentrated around the spider arms, the SNR could be further increased by implementing a filter that optimally selects only subapertures that contain segment piston information.

The flip-flop modulation method makes some assumptions around how fast a tip/tilt modulator could change modulation states. An experimental demonstration of stopping and starting the modulation of the pyramid to investigate the full effects on the AO system would be beneficial.

Appendix A

KL MODAL BASIS FOR THE THORLABS DMP40

A.0.0.1 Modal basis

The Thorlabs software development kit provides an interface to control the DM with a normalised Zernike basis, where Zernike polynomials Z_0 to Z_{11} are controllable with a normalised amplitude range of -1 to 1. Through the experiments carried out in this thesis, it was found that some Zernike modes were not symmetrical through the entire amplitude range. This lead to the development of a new modal basis for the DM which consists of the DM eigenmodes.

To calculate the DM eigenmodes, the influence function for each actuator is measured using a Thorlabs WFS20-7AR Shack-Hartmann WFS and the first 24 influence functions are shown in Figure A.1. Due to the actuator geometry of the DM and the lenslet size of the Thorlabs WFS20-7AR, the influence functions are poorly sampled. In the laboratory configuration used, the WFS20-7AR cannot measure the absolute amplitude of the actuator influence functions; for this reason, the influence functions are normalised to their peak.

Each influence function is reshaped from a two-dimensional matrix into a vector. Each influence function vector is then placed into a new matrix where each influence function vector is a new row, forming the matrix Q. The influence function covariance matrix, Δ_{geom}, is calculated as

$$\Delta_{\text{geom}} = Q^T \cdot Q. \tag{A.1}$$

By diagonalising the influence function covariance matrix, Δ_{geom}, the DM eigenmodes can be found with a singular value decomposition

$$\Delta_{\text{geom}} = USV, \tag{A.2}$$

where U and V are unitary matrices and S is a diagonal matrix of singular values. U, V and S are found by SVD factorisation. As we are dealing with a real, square matrix, $U = V^T$, which are the eigenvectors of Δ_{geom} and S contains the corresponding

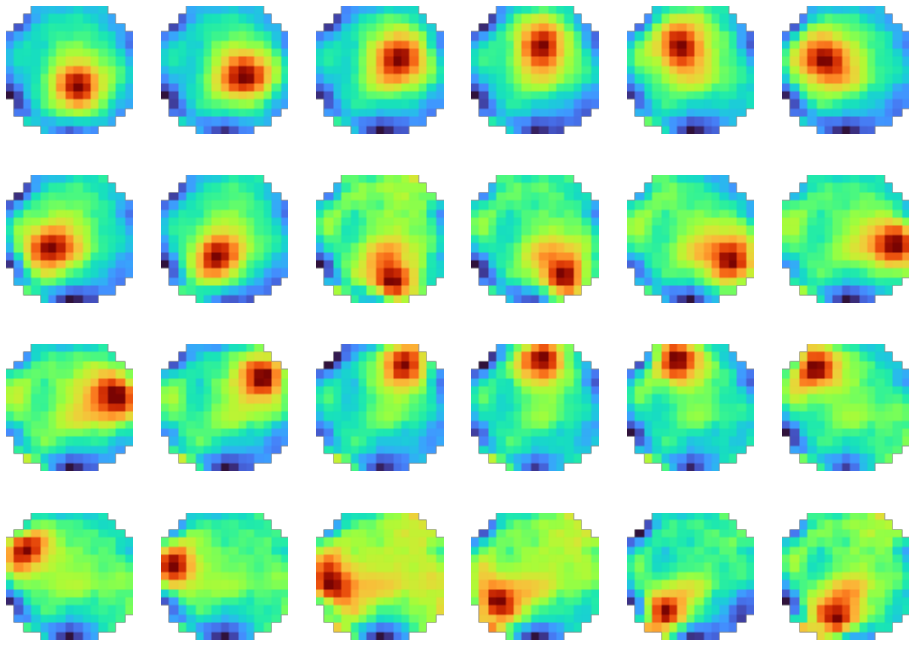

Figure A.1 The first 24 influence functions of the Thorlabs DMP40 DM measured with a Thorlabs WFS20-7AR Shack-Hartmann WFS. The WFS is not able to measure the absolute amplitude of the actuator influence functions and are normalised to their peak.

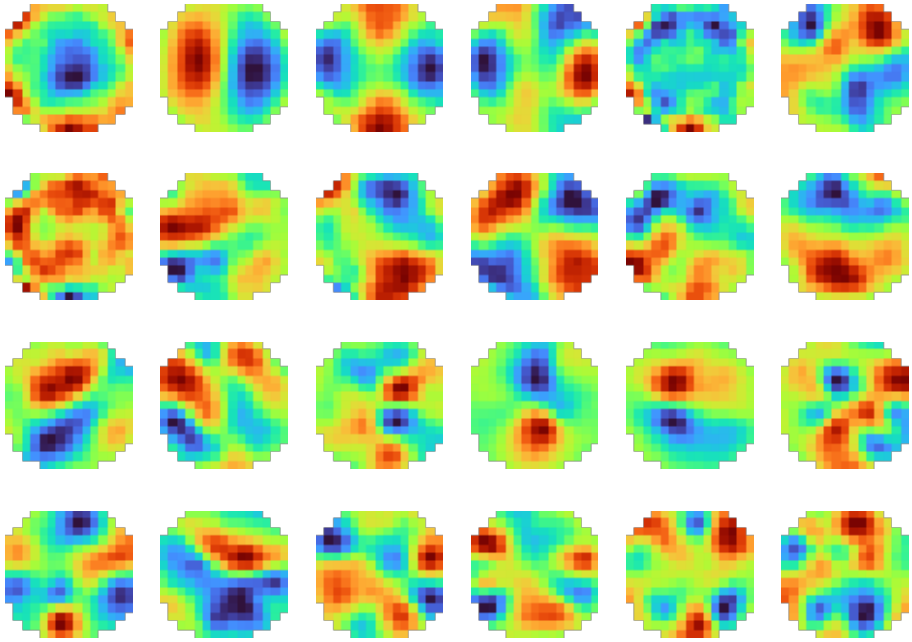

Figure A.2 The first 24 eigenmodes of the Thorlabs DMP40 DM. Each mode is normalised to its peak intensity.

eigenvalues. From this, the KL basis is constructed as:

$$Z_{\mathrm{KL}}(i) = \sum_{m=0}^{M-1} V_{i,m} Q_{i,m}, \tag{A.3}$$

where Z_{KL} is the modes-to-command matrix for the DM eigenmodes, m is the eigenmode index and i is the number of DM actuators. The first 24 DM eigenmodes are shown in Figure A.2. These computed eigenmodes were not found to be any better than the Zernike modes built into the DM, so the built-in Zernike modes were used.

REFERENCES

Akondi, V., Castillo, S. and Vohnsen, B. (2014), "Multi-faceted digital pyramid wavefront sensor", *Optics Communications*, Vol. 323, pp. 77–86.

Arsenault, R., Biasi, R., Gallieni, D., Riccardi, A., Lazzarini, P., Hubin, N., Fedrigo, E., Donaldson, R., Oberti, S., Stroebele, S., Conzelmann, R. and Duchateau, M. (2006), "A deformable secondary mirror for the VLT", In B.L. Ellerbroek and D.B. Calia (editors), *Advances in Adaptive Optics II*, Vol. 6272, International Society for Optics and Photonics, SPIE, pp. 284 – 295.

Baldwin, J.E., Tubbs, R.N., Cox, G.C., Mackay, C.D., Wilson, R.W. and Andersen, M.I. (2001), "Diffraction-limited 800 nm imaging with the 2.56 m Nordic Optical Telescope", *Astronomy & Astrophysics*, Vol. 368, No. 1, pp. L1–L4.

Béchet, C., Le Louarn, M., Tallon, M. and Thiébaut, É. (2008), "Performances of the fractal iterative method with an internal model control law on the ESO end-to-end ELT adaptive optics simulator", Vol. 7015 of *Proc. SPIE*, pp. 70151H–70151H–9.

Berry, R. and Burnell, J. (2005), *The handbook of astronomical image processing*, Vol. 2, Willmann-Bell, Inc.

Bifano, T.G., Perreault, J.A. and Bierden, P.A. (2000), "Micromachined deformable mirror for optical wavefront compensation", In J.D. Gonglewski, M.A. Vorontsov and M.T. Gruneisen (editors), *High-Resolution Wavefront Control: Methods, Devices, and Applications II*, Vol. 4124, International Society for Optics and Photonics, SPIE, pp. 7 – 14.

Born, M. and Wolf, E. (1999), *Principles of Optics*, Cambridge University Press, 7th ed.

Bouchez, A.H., Angeli, G.Z., Ashby, D.S., Bernier, R., Conan, R., McLeod, B.A., Quirós-Pacheco, F. and van Dam, M.A. (2018a), "An overview and status of GMT active and adaptive optics", In L.M. Close, L. Schreiber and D. Schmidt (editors), *Adaptive Optics Systems VI*, Vol. 10703, International Society for Optics and Photonics, SPIE, pp. 284 – 299.

Bouchez, A.H., Angeli, G.Z., Ashby, D.S., Bernier, R., Conan, R., McLeod, B.A., Quirós-Pacheco, F. and van Dam, M.A. (2018b), "An overview and status of GMT active and adaptive optics", In L.M. Close, L. Schreiber and D. Schmidt (editors), *Adaptive Optics Systems VI*, Vol. 10703, International Society for Optics and Photonics, SPIE, pp. 284 – 299.

Boyer, C. (2018), "Adaptive optics program at TMT", In L.M. Close, L. Schreiber and D. Schmidt (editors), *Adaptive Optics Systems VI*, Vol. 10703, International Society for Optics and Photonics, SPIE, pp. 314 – 326.

Boyer, C. and Ellerbroek, B. (2016), "Adaptive optics program update at TMT", In E. Marchetti, L.M. Close and J.P. Véran (editors), *Adaptive Optics Systems V*, Vol. 9909, International Society for Optics and Photonics, SPIE, pp. 78 – 91.

Breckinridge, J. and Voelz, D. (2011), *Computational Fourier Optics: A MATLAB Tutorial*, SPIE Press monograph, SPIE Press.

Cayrel, M. (2012), "E-ELT optomechanics: overview", In *Ground-based and Airborne Telescopes IV*, International Society for Optics and Photonics, SPIE.

Chambouleyron, V., Fauvarque, O., Janin-Potiron, P., Correia, C., Sauvage, J.F., Schwartz, N., Neichel, B. and Fusco, T. (2020), "Pyramid wavefront sensor optical gains compensation using a convolutional model", *Astronomy and Astrophysics*, Vol. 644, A6.

Chew, T.Y., Clare, R.M. and Lane, R.G. (2006), ""a comparison of the Shack-Hartmann and pyramid wavefront sensors"", *Optics Communications*, Vol. 268, pp. 189 – 195.

Clare, R.M., Le Louarn, M. and Bechet, C. (2011), "Laser guide star wavefront sensing for ground-layer adaptive optics on extremely large telescopes", *Appl Opt*, Vol. 50, No. 4, pp. 473–83.

Clare, R.M., Engler, B.E. and Weddell, S.J. (2020), "Wavefront reconstruction with the cone sensor", In *2020 35th International Conference on Image and Vision Computing New Zealand (IVCNZ)*, pp. 1–6.

Clare, R. and Le Louarn, M. (2011), "Numerical simulations of an extreme AO system for an ELT", .

Clare, R.M. (2004), *Wavefront sensing and phase retrieval for astronomical imaging*, Thesis (PhD), University of Canterbury, 2004.

Clare, R.M. and Lane, R.G. (2005), "Wave-front sensing from subdivision of the focal plane with a lenslet array", *J. Opt. Soc. Am. A*, Vol. 22, No. 1, pp. 117–125.

Clare, R.M., Engler, B., Weddell, S., Shatokhina, I., Obereder, A. and Le Louarn, M. (2017), "Numerical evaluation of pyramid type sensors for extreme adaptive optics for the European Extremely Large Telescope", In *Adaptive Optics for Extremely Large Telescopes 5*, .

Clare, R.M. and Lane, R.G. (2003), "Wavefront sensing from spatial filtering at the focal plane", In R.K. Tyson and M. Lloyd-Hart (editors), *Astronomical Adaptive Optics Systems and Applications*, Vol. 5169, International Society for Optics and Photonics, SPIE, pp. 43 – 54.

Cooley, J.W. and Tukey, J.W. (1965), "An Algorithm for the Machine Calculation of Complex Fourier Series", *Math. Comput.*, Vol. 19, pp. 297–301.

Davies, R. and Kasper, M. (2012), "Adaptive Optics for Astronomy", *Annual Review of Astronomy and Astrophysics*, Vol. 50, No. 1, pp. 305–351.

Deo, V., Gendron, E., Rousset, G., Vidal, F. and Buey, T. (2018), "A modal approach to optical gain compensation for the pyramid wavefront sensor", In L.M. Close, L. Schreiber and D. Schmidt (editors), *Adaptive Optics Systems VI*, Vol. 10703, International Society for Optics and Photonics, SPIE, pp. 653 – 670.

Engler, B., Weddell, S., Le Louarn, M. and Clare, R. (2018), "Effects of the telescope spider on extreme adaptive optics systems with pyramid wavefront sensors ", In *Adaptive Optics Systems VI*, International Society for Optics and Photonics, SPIE.

ESO (2021), "FAQ | ELT | ESO", `https://elt.eso.org/about/faq/#question_2`.

Esposito, S. and Riccardi, A. (2001), "Pyramid wavefront sensor behavior in partial correction adaptive optics", *Astron Astrophys*, Vol. 369, pp. L9–L12.

Fauvarque, O., Neichel, B., Fusco, T., Sauvage, J.F. and Girault, O. (2016), "General formalism for Fourier-based wave front sensing", *Optica*, Vol. 3, No. 12, p. 1440.

Fauvarque, O., Neichel, B., Fusco, T., Sauvage, J.F. and Girault, O. (2017), "General formalism for Fourier-based wave front sensing: application to the pyramid wave front sensors", *Journal of Astronomical Telescopes, Instruments, and Systems*, Vol. 3, No. 1, p. 019001.

Fourier, J. (1822), *Théorie analytique de la chaleur*, F. Didot.

Fried, D.L. (1966), "Optical Resolution Through a Randomly Inhomogeneous Medium for Very Long and Very Short Exposures", *J. Opt. Soc. Am.*, Vol. 56, No. 10, pp. 1372–1379.

Fried, D.L. (1982), "Anisoplanatism in adaptive optics", *J. Opt. Soc. Am.*, Vol. 72, No. 1, pp. 52–61.

Gendron, E. (1995), *Optimisation de la commande modale en optique adaptative : application a l'astronomie*, PhD thesis.

GMT (2021), "Quick Facts | Giant Magellan Telescope", `https://www.gmto.org/overview/quick-facts/`.

Goodman, J. (2005), *Introduction to Fourier Optics*, W. H. Freeman, 3rd ed.

Hickson, P. (2014), "Atmospheric and adaptive optics", *The Astronomy and Astrophysics Review*, Vol. 22, No. 1.

Holzlöhner, R., Kimeswenger, S., Kausch, W. and Noll, S. (2020), "Bolometric Night Sky Temperature and Subcooling of Telescope Structures", *arXiv e-prints*, arXiv:2010.01978.

Horsley, D.A., Park, H., Laut, S.P. and Werner, J.S. (2007), "Characterization of a bimorph deformable mirror using stroboscopic phase-shifting interferometry", *Sensors and Actuators A: Physical*, Vol. 134, No. 1, pp. 221–230, international Mechanical Engineering congress and Exposition 2005.

Hubin, N., Ellerbroek, B.L., Arsenault, R., Clare, R.M., Dekany, R., Gilles, L., Kasper, M., Herriot, G., Le Louarn, M., Marchetti, E., Oberti, S., Stoesz, J., Veran, J.P. and Verinaud, C. (2006), "Adaptive optics for Extremely Large Telescopes", *Proceedings of the International Astronomical Union*, Vol. 1, No. S232, pp. 60–85.

Hutterer, V., Shatokhina, I., Obereder, A. and Ramlau, R. (2018), "Advanced wavefront reconstruction methods for segmented Extremely Large Telescope pupils using pyramid sensors", *Journal of Astronomical Telescopes, Instruments, and Systems*.

Ilovitsh, T., Ilovitsh, A., Sheridan, J. and Zalevsky, Z. (2014), "Optical realization of the radon transform", *Opt. Express*, Vol. 22, No. 26, pp. 32301–32307.

Kasper, M., Beuzit, J.L., Verinaud, C., Gratton, R.G., Kerber, F., Yaitskova, N., Boccaletti, A., Thatte, N., Schmid, H.M., Keller, C., Baudoz, P., Abe, L., Aller-Carpentier, E., Antichi, J., Bonavita, M., Dohlen, K., Fedrigo, E., Hanenburg, H., Hubin, N., Jager, R., Korkiakoski, V., Martinez, P., Mesa, D., Preis, O., Rabou, P., Roelfsema, R., Salter, G., Tecza, M. and Venema, L. (2010), "EPICS: direct imaging of exoplanets with the E-ELT", In I.S. McLean, S.K. Ramsay and H. Takami (editors), *Ground-based and Airborne Instrumentation for Astronomy III*, Vol. 7735, International Society for Optics and Photonics, SPIE, pp. 948 – 956.

Kolmogorov, A. (1941), "The Local Structure of Turbulence in Incompressible Viscous Fluid for Very Large Reynolds' Numbers", *Akademiia Nauk SSSR Doklady*, Vol. 30, pp. 301–305.

Korkiakoski, V., Vérinaud, C. and Louarn, M.L. (2008), "Improving the performance of a pyramid wavefront sensor with modal sensitivity compensation", *Appl. Opt.*, Vol. 47, No. 1, pp. 79–87.

Lai, O., Jr., P.J.S. and Gendron, E. (2000), "MANO: the modal analysis and noise optimization program for the W.M. Keck Observatory adaptive optics system", In P.L. Wizinowich (editor), *Adaptive Optical Systems Technology*, Vol. 4007, International Society for Optics and Photonics, SPIE, pp. 620 – 631.

Lane, R.G. and Tallon, M. (1992), "Wave-front reconstruction using a Shack-Hartmann sensor", *Appl Opt*, Vol. 31, No. 32, pp. 6902–8.

Law, N. M., Mackay, C. D. and Baldwin, J. E. (2006), "Lucky imaging: high angular resolution imaging in the visible from the ground", *A&A*, Vol. 446, No. 2, pp. 739–745.

Le Louarn, M., Verinaud, C., Korkiakoski, V. and Fedrigo, E. (2004), "Parallel simulation tools for AO on ELTs", In *Advancements in Adaptive Optics*, International Society for Optics and Photonics, SPIE.

Le Roux, B. and Carbillet, M. (2006), "Advantage of a predictive control law for extreme adaptive optics imaging", In C. Aime and F. Vakili (editors), *IAU Colloq. 200: Direct Imaging of Exoplanets: Science & Techniques*, pp. 597–602.

Mahajan, V.N. (1983), "Strehl ratio for primary aberrations in terms of their aberration variance", *J. Opt. Soc. Am.*, Vol. 73, No. 6, pp. 860–861.

Martin, H.M., Zappellini, G.B., Cuerden, B., Miller, S.M., Riccardi, A. and Smith, B.K. (2006), "Deformable secondary mirrors for the LBT adaptive optics system", In B.L. Ellerbroek and D.B. Calia (editors), *Advances in Adaptive Optics II*, Vol. 6272, International Society for Optics and Photonics, SPIE, pp. 274 – 283.

Mathar, R.J. (2010), "Karhunen-Loéve basis of Kolmogorov phase screens covering a rectangular stripe", *Waves in Random and Complex Media*, Vol. 20, No. 1, pp. 23–35.

Noll, R.J. (1976), "Zernike polynomials and atmospheric turbulence*", *Journal of the Optical Society of America*, Vol. 66, No. 3, p. 207.

Petit, C., Meimon, S., Fusco, T., Kulcsár, C. and Raynaud, H.. (2010), "Hybrid lqg/integrator control for the vlt extrem ao system sphere", In *2010 IEEE International Conference on Control Applications*, pp. 878–883.

Phillion, D.W. and Baker, K. (2006), "Two-sided pyramid wavefront sensor in the direct phase mode", *Advances in Adaptive Optics Ii, Prs 1-3*, Vol. 6272, pp. U768–U779.

Primot, J., Rousset, G. and Fontanella, J.C. (1990), "Deconvolution from wave-front sensing: a new technique for compensating turbulence-degraded images", *J. Opt. Soc. Am. A*, Vol. 7, No. 9, pp. 1598–1608.

Ragazzoni, R. (1996), "Pupil plane wavefront sensing with an oscillating prism", *Journal of Modern Optics*.

Roddier, F. (1988), "Curvature sensing and compensation: a new concept in adaptive optics", *Appl. Opt.*, Vol. 27, No. 7, pp. 1223–1225.

Roddier, F. (1999), *Adaptive optics in astronomy*, Cambridge University Press.

Rosensteiner, M. (2012), "Wavefront reconstruction for extremely large telescopes via CuRe with domain decomposition", *J. Opt. Soc. Am. A*, Vol. 29, pp. 2328–2336.

Schwartz, N., Sauvage, J.F., Correia, C., Petit, C., Quiros-Pacheco, F., Fusco, T., Dohlen, K., Hadi, K.E., Thatte, N., Clarke, F., Paufique, J. and Vernet, J. (2017), "Sensing and control of segmented mirrors with a pyramid wavefront sensor in the presence of spiders", In *Adaptive Optics for Extreamly Large Telescopes 5*, .

Shatokhina, I., Obereder, A., Rosensteiner, M. and Ramlau, R. (2013), "Preprocessed cumulative reconstructor with domain decomposition: a fast wavefront reconstruction method for pyramid wavefront sensor", *Appl. Opt.*, Vol. 52, pp. 2640–2652.

Strang, G. (2006), *Linear algebra and its applications*, Thomson, Brooks/Cole, Belmont, CA, 4th ed.

Taylor, G.I. (1938), "The spectrum of turbulence", *Proceedings of the Royal Society of London. Series A-Mathematical and Physical Sciences*, Vol. 164, No. 919, pp. 476–490.

van Dam, M.A. and Lane, R.G. (2002), "Direct wavefront sensing using geometric optics", In J.D. Gonglewski, M.A. Vorontsov, M.T. Gruneisen, S.R. Restaino and R.K. Tyson (editors), *High-Resolution Wavefront Control: Methods, Devices, and Applications IV*, Vol. 4825, International Society for Optics and Photonics, SPIE, pp. 237 – 248.

van Dam, M.A., Conan, R., Bouchez, A.H. and Espeland, B. (2012), "Design of a truth sensor for the GMT laser tomography adaptive optics system", Vol. 8447 of *Proc. SPIE*.

van Dam, M.A. (2002), *Wave-front sensing for adaptive optics in astronomy*, Thesis (PhD), University of Canterbury.

Verinaud, C. (2004), "On the nature of the measurements provided by a pyramid wave-front sensor", *Optics Communications*, Vol. 233, No. 1-3, pp. 27–38.

Vernet, E., Cayrel, M., Hubin, N., Mueller, M., Biasi, R., Gallieni, D. and Tintori, M. (2012), "Specifications and design of the E-ELT M4 adaptive unit", In B.L. Ellerbroek, E. Marchetti and J.P. Véran (editors), *Adaptive Optics Systems III*, Vol. 8447, International Society for Optics and Photonics, SPIE, pp. 1991 – 1998.

Vohnsen, B., Castillo, S. and Rativa, D. (2011), "Wavefront sensing with an axicon", *Opt. Lett.*, Vol. 36, pp. 846–848.

Wang, J., Bai, F., Ning, Y., Huang, L. and Wang, S. (2010), "Comparison between non-modulation four-sided and two-sided pyramid wavefront sensor", *Opt. Express*, Vol. 18, pp. 27534–27549.

Wilson, R.G. (1975), "Wavefront-error evaluation by mathematical analysis of experimental foucault-test data", *Appl. Opt.*, Vol. 14, No. 9, pp. 2286–2297.

Wlodarczyk, K.L., Bryce, E., Schwartz, N., Strachan, M., Hutson, D., Maier, R.R.J., Atkinson, D., Beard, S., Baillie, T., Parr-Burman, P., Kirk, K. and Hand, D.P. (2014), "Scalable stacked array piezoelectric deformable mirror for astronomy and laser processing applications", *Review of Scientific Instruments*, Vol. 85, No. 2, p. 024502.